# Implementation of a Quantum Twisting Microscope

by

**Logan Miller**

A thesis submitted to the University

of Ottawa in partial fulfillment of

the requirements for the Master's degree in Physics

Department of Physics

University of Ottawa

Ottawa, Ontario, Canada

September 2025

© Logan Miller, Ottawa, Canada, 2025

# Abstract

Two dimensional (2D) materials are widely studied for both pure scientific interest and potential real world applications. Recently, the effect of a relative twist between 2D materials has generated a lot of interest. This has motivated the need for experimental techniques that can create samples with in-situ twist to avoid individual fabrication of samples at fixed angles. Additionally, many of the effects of twist require a fully momentum resolved band structure to fully appreciate them. This thesis describes and provides steps to replicate a recently developed novel scanning probe technique, the quantum twisting microscope (QTM), which provides an approach to overcoming both of these problems by facilitating the creation and characterization of 2D material interfaces with arbitrary twist angle.

# Acknowledgments

First and foremost, I would like to thank Professor Adina Luican-Mayer for her support and expert guidance throughout my master's degree. In particular, I am incredibly grateful and impressed by her effort and dedication to the professional development of myself and the group's other students. I am certain it will aid in my future career and likely already has! I wish her the best in her exciting move to UCI.

Thank you to Mathieu, Spyros, and Howard for teaching me virtually all I know about the cleanroom.

Thank you to my fellow members of the lab with whom I spent the past two years with.

Thank you to my dad and grandpa for always encouraging scientific inquiry when I was young as they have done throughout their careers. Thank you to Holly for her unending support and encouragement throughout my schooling. Thank you to all the rest of my friends and family for their support during all of my schooling.

# Contents

**Abstract** ii

**Acknowledgments** iii

**Contents** iv

**List of Figures** vii

**Chapter 1: Introduction** 1
- 1.1 2D Materials . . . 2
- 1.2 Graphene . . . 5
- 1.3 Moiré and Twist . . . 8
- 1.4 Scanning Probes . . . 11
  - 1.4.1 Atomic Force Microscope . . . 13
- 1.5 Opportunities for New Experimental Techniques in 2D Materials . . . 15
  - 1.5.1 In-Situ Twistronics Experiments . . . 15
  - 1.5.2 Momentum Resolved Electronic Structure . . . 16

**Chapter 2: Planar Tunneling Junctions** 18
- 2.1 Quantum Tunneling . . . 18
- 2.2 Planar Tunneling Junctions . . . 19
- 2.3 Twistable Planar Tunneling Junction . . . 20
  - 2.3.1 Discussion . . . 34
- 2.4 Other QTM Experiments . . . 36
  - 2.4.1 Backgated Sample and Probe . . . 36
  - 2.4.2 Twistable Inelastic Planar Tunneling Junction . . . 37
  - 2.4.3 Tunneling Through Point Defects . . . 37

**Chapter 3: Implementation** 38
- 3.1 Custom AFM Tip . . . 39
- 3.2 Geometric Constraints . . . 42
- 3.3 Custom Stage . . . 43

3.4 Sample Pillar . . . 49
3.4.1 Substrate Selection . . . 50
3.4.2 Plasma Etch Photoresist Mask . . . 51
3.4.3 Plasma Etch . . . 54
3.4.4 KOH Wet Etch . . . 57
3.4.5 Electrical Contacts . . . 62
3.5 Measurement Electronics . . . 65
3.5.1 DC Measurements . . . 66
3.5.2 Lock-in Measurements . . . 66
3.6 Transfer Techniques . . . 68
3.6.1 Intermediate Polymer Transfer . . . 70
3.6.2 Flake Transfer . . . 75

**Chapter 4: Electrical Transport of Vertical Graphite Interfaces 82**
4.1 Setup . . . 83
4.2 Procedure . . . 88
4.3 Results . . . 90
4.4 Discussion . . . 97

**Chapter 5: Conclusions and Next Steps 99**

**Bibliography 101**

**Appendices 121**
A Methods . . . 122
A.1 Mechanical Exfoliation . . . 122
A.2 Polymer Stamp Preparation . . . 123
A.3 Heterostructure Preparation . . . 128
A.4 Specific Stamp Preparation for Graphite . . . 129
A.5 Flake Preparation on Substrate . . . 132
A.6 Inverted Transfer . . . 133
B Polymer Stamp PDMS Shape Motivation . . . 135
C Graphene Band Structure . . . 136
D Scanning Tunneling Microscope . . . 141
E QTM: Momentum Resolved Twisted Bilayer Graphene Examples . . . 142
F Photolithography Mask Design . . . 145
G Lockin Amplifier . . . 151
G.1 Filtering . . . 151
G.2 Testing . . . 152
H AFM Tip Solvent Bath . . . 156
I Ellispometry . . . 158

J PMMA Transfer Examples . . . . . 159

# List of Figures


1.1 Graphene honeycomb lattice structure . . . . . 5
1.2 Two honeycomb lattices rotated by a commensurate twist angle . . . 8
1.3 Two honeycomb lattices rotated by an incommensurate twist angle . 11
1.4 Schematic of standard SPM operation . . . . . 12
1.5 Tapping mode AFM scan of graphite flake . . . . . 14

2.1 Rotated honeycomb lattices with momentum offset . . . . . 21
2.2 Metal bands in parallel plate capacitor . . . . . 24
2.3 Graphene bands in parallel plate capacitor . . . . . 24
2.4 Solution to electrostatics of graphene based parallel plate capacitor . 25
2.5 Spectral function of a graphene . . . . . 27
2.6 Difference between the Fermi-Dirac distributions of the two graphene layers . . . . . 27
2.7 Line cuts of difference between the Fermi-Dirac distributions of the two graphene layers . . . . . 28
2.8 Visualization of the band offset and twist on the product of graphene spectral functions . . . . . 29
2.9 Effect of the Fermi Dirac windowing on the product of graphene layer spectral functions . . . . . 30

2.10 Calculated tunneling current as a function of $V_B$ and $\theta$ with features overlaid . . . 31
2.11 Features and conditions within calculated tunneling current as a function of $V_B$ and $\theta$ . . . 32
2.12 Graphene bands depicted at the features and conditions within calculated tunneling current as a function of $V_B$ and $\theta$ . . . 33
2.13 Monolayer graphene probe used to probe twisted bilayer graphene sample. . . . 35
2.14 Demonstration of inherent momentum offset between K points electrons of dissimilar materials. . . . 36

3.1 Schematic displaying the key components of a QTM system . . . 39
3.2 Commercial tipless cantilevers . . . 40
3.3 Commercial tipless cantilevers with Au coating . . . 41
3.4 Commercial tipless cantilevers with Au coating and custom tip . . . 41
3.5 Custom deposited tip . . . 42
3.6 Schematics depicting the necessary considerations when engaging a short custom AFM tip to a sample. . . . 43
3.7 Schematic of components comprising custom stage . . . 44
3.8 Schematic demonstrating the two possible planes to rotate within . . . 45
3.9 Schematic demonstrating the effect of rotating an uncentred sample . . . 46
3.10 Bruker AFM system . . . 47
3.11 Schematic of designed stage mount with slotted screw holes and mounting holes for the goniometer. . . . 48
3.12 Schematic of designed bare PCB . . . 49

3.13 Raised sample pillar substrate fabrication process . . . . . 50
3.14 Patterned photoresist etch mask. . . . . 53
3.15 Line profile of patterned photoresist etch mask. . . . . 54
3.16 $Ar/CF_4$ plasma etch $SiO_2$ etch rate . . . . . 55
3.17 Images of displayed lack of spatial uniformity in plasma etching. . . . 56
3.18 Patterned $SiO_2$ mask. . . . . 57
3.19 KOH etching setup . . . . . 59
3.20 Etched sample pillar. . . . . 60
3.21 KOH sidewall etching . . . . . 60
3.22 Profilometre scan of etched pillar . . . . . 61
3.23 Schematic demonstrating role of LOR in patterned deposition . . . . 62
3.24 Etched sample pillar with developed resist contact pattern . . . . . 64
3.25 Complete raised sample pillars with different metal contact patterns . 65
3.26 Demonstration of the use of an AC bias superimposed on a DC value to estimate $dI/dV$. . . . . 66
3.27 Lock-in amplifier functionality . . . . . 68
3.28 vdW transfer to a substrate with the polymer both above and below the vdW structure. . . . . 69
3.29 Schematic demonstrating the transfer of a pre-stacked vdW structure, that has not been flipped right side up, to a substrate polymer side up. 70
3.30 Schematic demonstrating the transfer of a pre-stacked vdW structure, that has been flipped, to a substrate polymer side up. . . . . 70
3.31 Schematic demonstrating the steps to transfer and flip a vdW structure from PPC to a PMMA tape frame. . . . . 73

3.32 Images of the steps to flip a vdW heterostructure from a PPC film to a PMMA/PVA film. . . . . 74
3.33 Polymer tape frame suspended over glass slide with a hole. . . . . 75
3.34 Structure used to prop up AFM tips for transfer. . . . . 76
3.35 Schematic demonstrating the steps to place a vdW structure from a polymer tape frame to an AFM tip . . . . . 78
3.36 Schematic demonstrating the steps to place a vdW structure from a polymer tape frame to a raised sample pillar. . . . . 79
3.37 Images of the steps to place a graphite flake from a PPC tape frame to a custom AFM tip. . . . . 80
3.38 Images of the steps to place a graphite flake from a PPC tape frame to a raised sample pillar . . . . . 81

4.1 Conductive AFM probe holder with custom AFM tip . . . . . 83
4.2 Graphite flake on sample pillar contacted by metal wire. . . . . 84
4.3 Custom stage with sample mounted and contacted . . . . . 84
4.4 Experimental setup showing connections to SMU . . . . . 86
4.5 Circuit diagram of system under test . . . . . 86
4.6 Schematic of the expected effective interface resistances for different landing conditions. . . . . 87
4.7 vdW tip during laser alignment . . . . . 89
4.8 vdW tip during tip engagement . . . . . 90
4.9 IV curve of withdrawn vdW tip . . . . . 91
4.10 IV curves between the graphite vdW tip and Au surface . . . . . 92
4.11 IV curves between the graphite vdW tip and graphite flake . . . . . 93

4.12 Contact mode AFM scans of Au surface on raised pillar taken using custom vdW tip. . . . . 94
4.13 Contact mode AFM scans of graphite flake on raised pillar taken using custom vdW tip. . . . . 94
4.14 IV curves between the graphite vdW tip and graphite flake post topographic scans . . . . . 95
4.15 IV curves between the graphite vdW tip and gold post topographic scans 96
4.16 vdW tip before and after topographic scan over rough surface . . . . 97

A.1 Mechanical exfoliation process . . . . . 124
A.2 PDMS shapes . . . . . 125
A.3 Polymer stamp making process . . . . . 127
A.4 Dry transfer technique used to pickup an hBN flake. . . . . 129
A.5 Graphite stamp preparation . . . . . 131
A.6 AFM tip flake cutting . . . . . 132
A.7 Inverted transfer method . . . . . 134
A.8 Inverted transfer drift demonstration . . . . . 135
A.9 PDMS shape motivation . . . . . 136
A.10 Graphene probe and TBLG sample bands used in the calculation of tunneling current . . . . . 143
A.11 Calculated tunneling current between graphene probe and TBLG samples 144
A.12 Photolithography masks . . . . . 145
A.13 Padding added to pillar shapes in the first photolithography mask . . 146
A.14 Pillar shapes on the first photolithography mask . . . . . 147
A.15 Contact shapes overlaid onto a pillar shape. . . . . 148

A.16 Alignment marks in the first and second mask. . . . . 149
A.17 Use of alignment marks when aligning second mask to etched pillar substrate. . . . . 149
A.18 Window in the second mask around the pillars to enable easy viewing. 150
A.19 Use of window demonstrated when aligning second mask to etched pillar substrate. . . . . 150
A.20 First and second masks aligned. . . . . 151
A.21 Circuit used to test homemade lock-in amplifier . . . . . 153
A.22 Demonstration of lockin amplifier used on test circuit . . . . . 154
A.23 Sourced and measured signals during lockin amplification. . . . . 155
A.24 Processing performed on measured signal during lockin amplification. 156
A.25 Tweezer holder to facilitate AFM tip solvent baths . . . . . 157
A.26 Flipped vdW heterostructure transfer from PMMA film to raised sample pillar . . . . . 160
A.27 Flipped vdW heterostructure transfer from PMMA film to tipless AFM cantilever . . . . . 161

# Chapter 1

# Introduction

Whether in search of new technological applications or in the desire to deepen our understanding of science, scientists and engineers alike are interested in studying the electronic properties of materials. Today, 2D materials offer exciting opportunities in both directions and significant effort is being put into their study, particularly the effects of twisted 2D materials [1].

Traditional fabrication methods of twisted 2D materials are effective and reliable; however, they can be moderately tedious and time consuming, especially when multiple samples at different twist angles are needed, as each sample is assembled at a fixed angle. While innovative devices and techniques to realize in-situ twisted samples have been achieved, few groups have implemented them [2–6]. Promisingly, recent progress towards more universal approaches has been made. This includes the instrument described in this thesis [7] as well as a completely separate platform [8]. In addition to being able to produce 2D material samples with any twist, the field needs more methods to probe the electronic band structures of these materials. Current

experimental setups do exist, but they are limited in number and have their own sets of challenges.

In this thesis, I discuss my efforts towards the development and replication of a novel scanning probe, the Quantum Twisting Microscope (QTM) [7], capable of characterising 2D material planar interfaces at an arbitrary twist angle through the collection of an out-of-plane current. This platform allows for momentum-resolved spectroscopy and in situ twistronic experiments [7, 9]; and although not the focus here, the QTM platform is highly versatile and can enable many other measurement schemes [10–15].

In Chapter 1, I begin with a high-level introduction to 2D materials as well as discuss the experimental techniques this system can replicate. A self-contained pedagogical explanation of the theory that describes the momentum-resolved spectroscopy function of the instrument is provided in Chapter 2. Chapter 3 covers how to implement the scanning probe, followed by some early measurements which demonstrate initial proof of concept in Chapter 4. Finally, conclusions and future steps are outlined in Chapter 5.

## 1.1 2D Materials

There is a distinct class of materials known as two-dimensional (2D) or van der Waals (vdW) materials which are organized as layers of one or a few atom thick sheets stacked on top of each other. Within these layers, the atoms are tightly bound in plane by covalent bonds and are loosely bound out of plane to adjacent layers by vdW forces [16].

Although, researchers have studied vdW materials for quite some time, it was initially believed that individual layers (monolayers) would be thermodynamically unstable and that they could only exist as a part of their larger layered bulk structures [17]. Despite this, there were still attempts to isolate individual layers through intercalation and growth techniques [17] and theoretical models were still developed before their successful isolation. It was Canadian scientist P.R. Wallace from Chalk River who initially solved for the electronic structure of graphene (monolayer of graphite) when he was investigating graphite post World War II, presumably in the context of graphite's use as a moderator in nuclear fission reactors [18, 19].

In 2004, A. Geim and K. Novoselov were successful in isolating a monolayer of graphene from bulk graphite by mechanical exfoliation [20, 21]. Their method, a protocol for which is described in Appendix A.1, demonstrated that the weak vdW forces between layers could be overcome by the adhesive force of scotch tape such that a bulk crystal could be thinned down to its atomically thin layers. Monolayers of many other 2D materials have since been isolated, including insulators such as hexagonal boron nitride (hBN) [22, 23], metallic and semiconducting transition metal dichalcogenides (TMD) [24], magnetic materials [25, 26], superconductors [27, 28] and various other materials with novel characterizations [29]. In addition, growth methods have become sufficiently sophisticated such that relatively high quality monolayers can be grown [30–33].

The study of these materials has revealed that monolayers and few layers host distinct properties not present in their bulk counterparts. For example, graphene monolayers host quasiparticles that behave as if they are massless [34] and certain TMDs go from

having indirect to direct bandgaps when reduced from bulk to monolayers [35]. In addition, the vdW gap between layers makes it such that 2D materials can be stacked to create heterostructures with new effective material properties [23,36]. The recipes and methods to fabricate these vdW heterostructures can be found in Appendix A.

The materials in heterostructures are important, but the relative twist between layers introduces another important degree of freedom. Although some twist angle inhomogeneity may be inherently present in graphite flakes [37–39] or other materials, methods to introduce a deterministic twist angle during heterostructure fabrication have been widely adopted [40]. Notably in 2010, R. Bistritzer and A. H. MacDonald theoretically showed that at specific angles between graphene layers, the dispersion relation of the electrons would become flat. This would effectively quench the kinetic energy of the electrons [41] making electron-electron correlations relevant [42, 43]. Early scanning tunneling microscope (STM) studies supported the presence of these flatbands [44, 45], but in 2018, transport measurements conclusively showed their presence and relevance with correlated insulator states and superconducting states existing within the same twisted samples [46, 47]. The phase diagram of these samples resembled those found in high temperature superconductors, sparking further excitement into the field of 2D materials [42]. Despite the prolific publishing record of these magic angle twisted bilayer graphene samples, our understanding of the nature of these strongly interacting states remains incomplete [48], and we need more momentum resolving techniques to study them. Research has been extended beyond twisted bilayers and other more complicated systems with flat bands are now being investigated [49–53].

## 1.2 Graphene

Graphene is arguably the most widely studied 2D material, but it would be a mistake to owe this entirely to it being the first to be isolated and conceptualised. Graphene has tremendous properties, some of which are highlighted here, and from a practical standpoint, the availability of both low defect count synthetic highly oriented pyrolytic graphite (HOPG) and natural graphite make it very accessible [1].

Its interesting properties are the direct result of its honeycomb lattice crystal structure constructed from two identical triangular sublattices. An image of the honeycomb lattice in real and reciprocal space can be found in Figure 1.1.

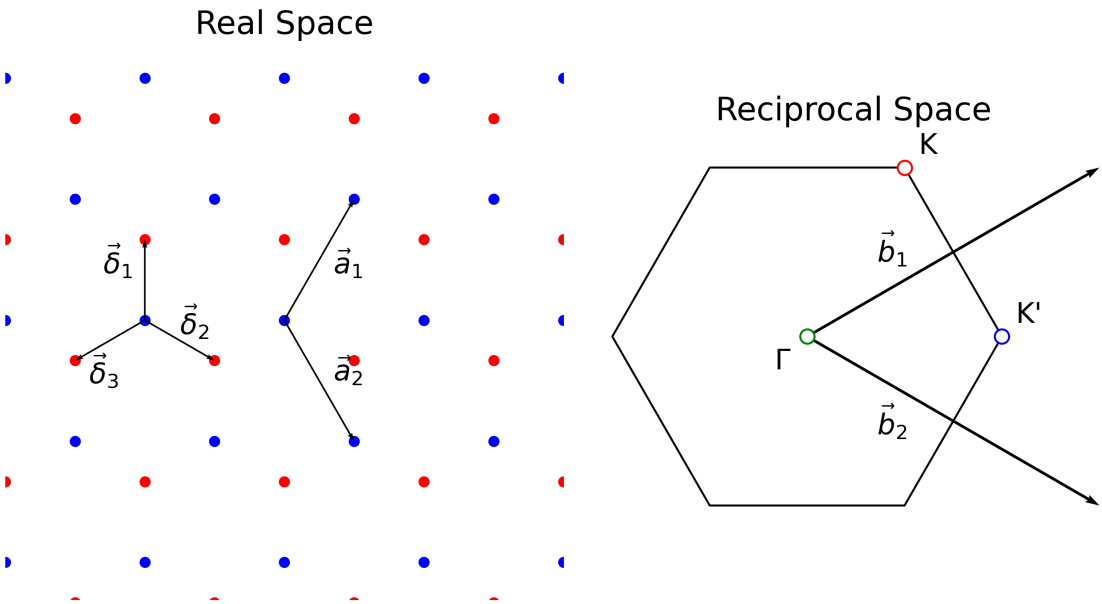


Figure 1.1: Graphene honeycomb lattice in real and reciprocal space. Left: Real space with two sublattices shown in red and blue. Lattice vectors are labeled by $\vec{a}_i$ and nearest neighbour vectors are labeled by $\vec{\delta}_j$. Right: Reciprocal space showing first Brillouin Zone with K, K' and Γ high symmetry points. Reciprocal lattice vectors labeled by $\vec{b}_i$.

In Appendix C, this geometry is used to solve a nearest neighbour (NN) tight binding model, where one finds that the conduction and valence bands of graphene's electronic structure meet at two degenerate discrete points in momentum space known as the K and K' points (referred to from now on as just K points). The bands meet at the Fermi energy where they have zero density of states (DOS). Around the K points, the electron dispersion relation is linear with respect to their crystal momenta,

$$E = \pm \hbar v_f |k| \tag{1.1}$$

where $E$ is the quasiparticle energy, $\hbar$ is the reduced Planck constant, $k$ is the crystal momentum with respect to the K points and $v_f$ is the Fermi velocity and is approximately 300x smaller than the speed of light, $v_f \approx c/300$. The reader may notice that this linear relationship is distinct from the more common dispersion relations of electrons within crystals that can approximated by that of a free particle with a renormalized effective mass, $m^*$.

$$E(k) = \frac{(\hbar k)^2}{2m^*} \tag{1.2}$$

This distinction becomes apparent if we instead write the full relativistic energy of a particle, with momentum $p$, speed of light $c$ and rest mass $m$,

$$E^2 = (pc)^2 + (mc^2)^2 \tag{1.3}$$

$$E_{\text{photon}} = pc \tag{1.4}$$

A photon or a massless particle's energy is linear with respect to its momentum. Given

the resemblance, electrons in graphene with crystal momentum near the K points behave as if they are massless and are modeled by the relativistic Dirac equation. As a result, they are appropriately named Dirac fermions. This is more than an interesting observation as it has direct consequences on the behaviour of the electrons. For instance, Klein tunneling is a mechanism in which massless particles incident on potential barriers have near perfect transmission coefficients. This effect has been observed in graphene and makes it challenging to electrostatically confine electrons in graphene [54–56]. In addition, graphene's sublattice symmetry imparts another degree of freedom, distinct from spin, referred to as pseudospin. The pseudospin is locked to the crystal momentum such that they are either parallel or antiparallel, analogous to the concept of chirality between true spin and momentum found in quantum electrodynamics [19, 54]. The chiral nature of graphene's electrons makes it such that backscattering off impurities is suppressed [57]. Combined with graphene's high group velocity, $v_f$, all these effects lead to graphene samples having very high electron mobilities [58].

The Dirac cones in graphene are also robust and protected by discrete symmetries. To break the Dirac cones and open a bandgap, either sublattice symmetry or time reversal symmetry must be broken [59, 60]. Time reversal symmetry can broken with an external magnetic field leading to the formation of Landau levels and the quantum hall effect (QHE) [61, 62]. Haldane also showed that it is possible to achieve a QHE without an external magnetic field [63]. This has been experimentally realized in graphene systems where some correlated electron states within flatbands can break the symmetry [64]. The underlying substrates can break the sublattice symmetry as is seen with a small gap opening [65, 66], or it can directly be seen with hBN as a

honeycomb lattice with broken sublattice symmetry and a large gap of approximately 6 eV [67, 68].

## 1.3 Moiré and Twist

One of the mechanisms responsible for the properties of vdW heterostructures is the introduction of a new relevant periodic length scale. A weak periodic potential leads to band folding, effective mass renormalization, the creation of bandgaps, and in general, changes the dispersion relations [69]. When the bands become flat enough and electron energies become independent of crystal momentum, strong electron-electron correlations become relevant leading to properties not captured by the independent electron approximation [42, 43].

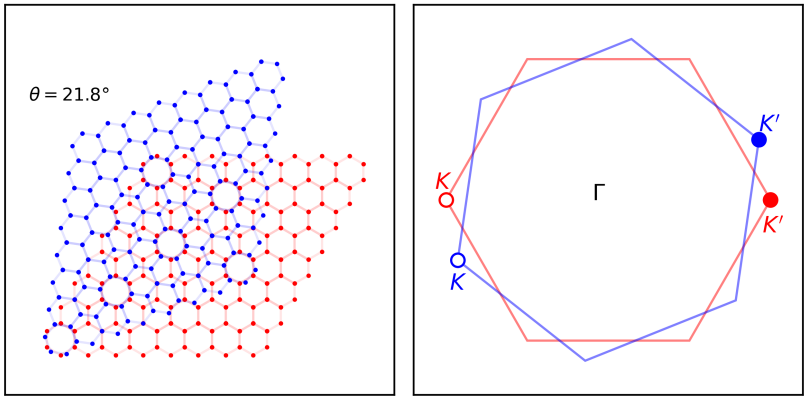


Figure 1.2: Two honeycomb lattices rotated with respect to each other by a commensurate angle of 21.8°. Left: Real space, Right: K space

To provide some intuition for why this new length scale appears, we can refer to our early wave mechanics. When two modes with slightly different frequencies are

superimposed, one intuitively expects low frequency beats [70]. This is shown in Figure 1.2, where two honeycomb lattices rotated with respect to each other produce a visible long range periodicity. In 2D, a spatial frequency, or lattice periodicity, is represented by $x$ and $y$ components, $\vec{k} = (k_x, k_y)$. A difference between two separate crystal's wavevectors can be the result of a difference in orientation (twist) or modulus (lattice constant). Consider two reciprocal lattice vectors with arbitrary twist angle, $\theta$, and relative lengths, $\delta$:

$$\vec{k_1}/|\vec{k_1}| = \begin{bmatrix} 1 \\ 0 \end{bmatrix} \tag{1.5}$$

$$\vec{k_2}/|\vec{k_1}| = \begin{bmatrix} \cos\theta & -\sin\theta \\ \sin\theta & \cos\theta \end{bmatrix} \begin{bmatrix} (1+\delta) \\ 0 \end{bmatrix} \tag{1.6}$$

Taking the difference between these and finding the magnitude,

$$\frac{(\vec{k_1} - \vec{k_2})}{|\vec{k_1}|} = \begin{bmatrix} 1 - (1+\delta)\cos\theta \\ -(1+\delta)\sin\theta \end{bmatrix} \tag{1.7}$$

$$|\frac{(\vec{k_1} - \vec{k_2})}{|\vec{k_1}|}|^2 = (1 - (1+\delta)\cos\theta)^2 + ((1+\delta)\sin\theta)^2 \tag{1.8}$$

$$= 2(1+\delta)(1-\cos\theta) + \delta^2 \tag{1.9}$$

we find a beat frequency magnitude. Converting that beat frequency back to real space we find the often quoted moiré wavelength:

$$\lambda = \frac{(1+\delta)a_0}{\sqrt{2(1+\delta)(1-\cos\theta) + \delta^2}} \tag{1.10}$$

We can fix the lattice constants as they would be with two layers of the same material,

$$\lambda = \frac{a_0}{\sqrt{2(1-\cos\theta)}} = \frac{a_0}{2\sin(\theta/2)} \tag{1.11}$$

The direct tunability of the moiré length scale with a relative twist between layers allows us to change the bands and enables the possibility of creating artificial lattices and quantum simulators [71].

It is important to note that the moiré superpattern is not strictly periodic with the underlying crystals and is usually quasiperiodic, not maintaining translational symmetry [70]. For the moiré period to be commensurate and form a periodic lattice, the moiré wave vectors must be integer linear combinations of the underlying crystal lattice vectors.

$$\vec{R_\lambda} = \vec{R_A} = \vec{R_A} \tag{1.12}$$

$$\vec{R_\lambda} = n\vec{a}_1^{(1)} + m\vec{a}_2^{(1)} = n'\vec{a}_1^{(2)} + m'\vec{a}_2^{(2)} \tag{1.13}$$

Given the coefficients must be integers, one would expect a discrete set of solutions. It can be enforced that $n = n'$ and $m = m'$ such that pairs are solutions to

$$\cos(\theta) = \frac{1}{2}\frac{m^2+n^2+4mn}{m^2+n^2+mn} \tag{1.14}$$

An incommensurate twist angle is shown in Figure 1.3 and a commensurate twist angle is shown in Figure 1.2. In both, a large moiré pattern is apparent, but only in the commensurate example is the pattern a perfect crystal. The effect of commensurability can be seen in the electrical properties of a twisted material (Section 1.5.1), but

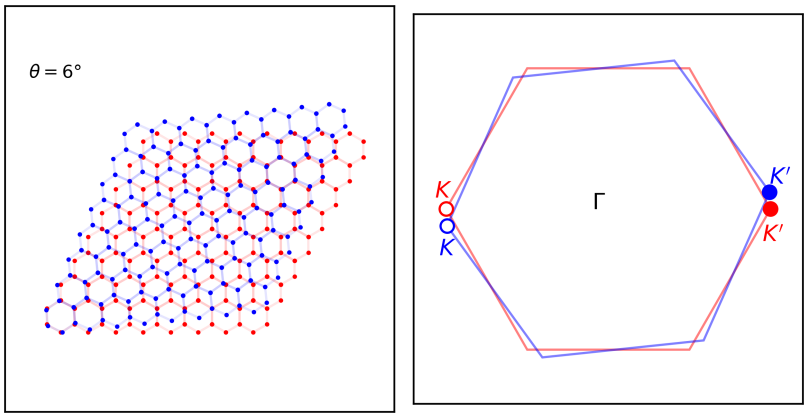


Figure 1.3: Two honeycomb lattices rotated with respect to each other by a non-commensurate angle of 6°. Left: Real space, Right: K space

it also has an effect on the feasibility of theoretical models. Atomistic calculations, such as density functional theory or tight binding models, require explicit inclusion of atoms and their positions. For small twist angles, where the moiré supercell is very large, accounting for all atoms makes these methods significantly more computationally expensive. As a result, continuum models that only focus on the moiré length scale, making commensurability less relevant, are often employed first [42, 70, 72].

## 1.4 Scanning Probes

Scanning probe microscopy (SPM) techniques are essential to the investigation of 2D materials as they lend themselves to studying the surfaces of materials through highly localized probe to surface interactions. In general, an SPM system requires a sharp probe with a distance to sample sensitive interaction, a feedback control loop (often proportional integral derivative (PID) is sufficient) and a set of stages to raster scan the probe across the sample [73]. Commonly used SPM techniques are the atomic

force microscope (AFM), essential to the QTM and described below, and the scanning tunneling microscope (STM), described in Appendix D.

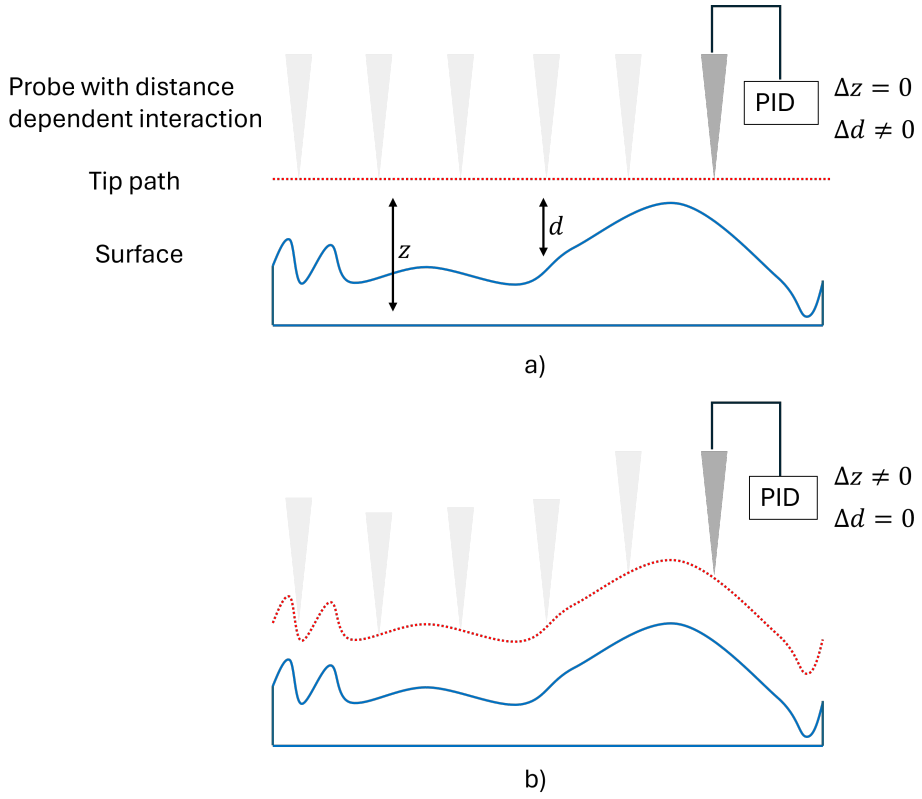


Figure 1.4: Two standard modes of operation in SPM using a probe with a distance dependent interaction and a PID controller. a) Position of the probe is fixed by PID and the interaction amplitude is recorded. b) Amplitude of the interaction is fixed by PID by maintaining the probe to sample distance thus mapping out the topography.

Figure 1.4 highlights the two main ways the control loop can be used: maintaining a constant interaction amplitude to some set point by adjusting the distance between probe and sample giving a topographic scan, or holding the height of the probe fixed while the amplitude of the interaction is recorded. With a functioning control loop, additional measurements can be performed independently of the interaction used in

the feedback.

### 1.4.1 Atomic Force Microscope

As mentioned, the AFM is commonly used in the field of 2D materials and has many variations. AFM relies on the Lennard Jones potential between a tip on a cantilever with calibrated stiffness and the sample surface. Standard commercial tips tend to have a radius around 10-20nm and heights of 10-20ums. When close to the sample, but not in contact, the tip to sample force is attractive causing the cantilever to deflect downwards. However, when in contact and very close, the tip to sample force changes sign and the cantilever is deflected up. The amplitude and sign of the force are monitored by reflecting a laser off the cantilever onto a photodetector (PD) array. During initial setup, the laser is aligned to the centre of the array, effectively zeroing the signal. The difference in the signal between the top and bottom halves of the array indicate vertical deflection of the cantilever, and differences between left and right halves indicate lateral deflection of the cantilever.

For measuring the topography of our samples, a tapping mode AFM scan is often used, an example of which is shown in Figure 1.5. In tapping mode, an AFM tip with a high Q factor cantilever is driven near its resonance by a piezoelectric actuator and the amplitude of its oscillation is recorded on the PD array. As the tip briefly comes into contact with the surface, or very nearly, the oscillation amplitude is modulated. The control loop aims to maintain the amplitude by adjusting the tip to sample distance mapping out the topography. In contact mode, the cantilever is not driven by an oscillator and it is a DC deflection of the cantilever that is controlled. As the tip scans

the surface, a z piezoelectric stage adjusts the height of the cantilever to maintain a constant deflection. Contact mode can also be used to acquire topographic scans of samples. However, the tip makes direct contact with the surface and poses a risk of damaging samples. Since the cantilevers used in contact mode have known stiffness values, the deflection of the cantilever corresponds to a measurable force. This enables the user to apply a known, controlled force to the sample during scanning.

The QTM is built off of an adapted AFM that is used in contact mode. With the constant deflection setpoint, conductance measurements can be performed independently of the photodiode signal used in the control loop.

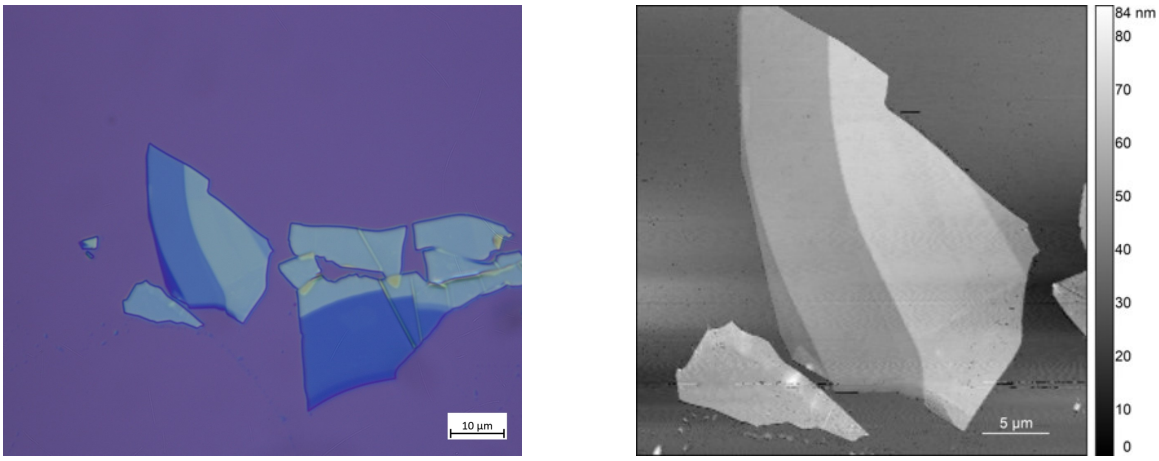


(a) (b)

Figure 1.5: Tapping mode AFM scan of graphite flake. Left: Optical image of exfoliated graphite flake on 285nm $SiO_2$/Si substrate. Right: Tapping mode AFM scan of the graphite flake.

## 1.5 Opportunities for New Experimental Techniques in 2D Materials

In the introduction, I identified two classes of experimental techniques in twisted 2D materials that present opportunities for further development. Here, I describe some setups within these classes that the QTM can improve on or add to.

### 1.5.1 In-Situ Twistronics Experiments

Important to the study of the effect of the twist angle on a 2D material is the interlayer coupling between layers as a function of the twist [74, 75]. To directly study this, one needs to either create a lot of samples or have a scheme to twist in-situ [2–6]. Many of these studies rely on the rotation of a microscopic gear structure to twist the layers with respect to each other. These have not been widely adopted and require specialized expertise, making more universal approaches to create 2D materials with arbitrary twist desirable [7, 8].

An example of a measurement that would be impractical with standard fabrication protocols is the study of graphite to graphite interfaces as a function of twist. Of those performed [2, 3], and recreated in [7], an incommensurate to commensurate phase transition can be observed by monitoring the interlayer conductance as a function of twist. At angles above 10°, the interlayer coupling of the graphene layers is heavily suppressed, leading to incoherent tunneling, and the layers behave as if they are independent [44, 45]. However, at commensurate twist angles where the moiré superlattice forms a perfect crystal, allowing for strong interlayer coupling and coherent tunneling to take place, a large peak in conductance is observed [2, 3, 7, 74, 76].

### 1.5.2 Momentum Resolved Electronic Structure

Measurement of the band structure of a crystal provides a full image of how electrons within the material behave. There are techniques to measure a 2D material's band structure; however, they are limited in number and have their own sets of challenges. Two techniques, separate from the one used in the thesis, that find common use are briefly described below.

#### Quasi Particle Interference

This technique is thoroughly described in [77, 78]. STM gives access to the local density of states (LDOS) of a material, $\rho(E, r)$, which provides the number of available states at a given energy, $E$, and position, $r$. The ability to perform highly localized spectroscopy with STM is very important and has had tremendous success. However, the STM tip is not selective of momentum as it sums over all available states at a given energy and position irrespective of the momentum, $k$. To achieve momentum resolution and extract the dispersion relation of a material, a loss of spatial resolution is required through a Fourier transform (FT). Near defects, wavefunctions can scatter to equal energy states with different momentum on the Fermi surface. This scattering can result in energy dependent oscillations that LDOS measurements are sensitive to. Taking a FT, the energy and wavelength dependence can be used to extract the dispersion relation of the bands. These measurements are very challenging and require highly stable systems as scan sizes need to be large to achieve good resolution in frequency space. Few QPI experiments have been performed on twisted graphene samples, presumably given the difficulty of these measurements.

### Angle-Resolved Photoemission Spectroscopy

This subsection briefly summarizes key aspects from [79]. Another widely used technique to achieve momentum resolution of electronic states in 2D materials is angle-resolved photoelectron spectroscopy (ARPES). In ARPES, electrons occupying energy states within a material can be kicked out by an incident photon via the photoelectric effect. The incident photons carry minimal momentum and it can be approximated that ejected electrons maintain their initial momentum from within the material. In typical setups, the energy of the ejected electron is measured on a detector with electromagnetic lenses while the momentum is recorded by the ejection angle of the electron. Most ARPES systems rely on ultraviolet light sources, often from synchrotrons, and cryogenic ultra high vacuum environments. Improvements to ARPES experiments are being made with complicated optical trains such that nanometer spot sizes can spatially resolve the bands (nano-ARPES) [80], but they unfortunately still do not have sufficient energy resolution to fully study certain samples such as twisted bilayer graphene [9].

# Chapter 2

# Planar Tunneling Junctions

This chapter provides a self contained description of the theory underlying the momentum resolved spectroscopy capabilities of the Quantum Twisting Microscope (QTM). It follows the supplemental of the original paper [7] with a more pedagogical approach, including simplifying assumptions, more steps and motivations. More generally, the background on tunneling experiments follows from [81]. The intention of this section is to provide sufficient intuition and understanding to another student so that the model can be easily implemented and even expanded on.

## 2.1 Quantum Tunneling

Classically, when a particle encounters a potential barrier with energy greater than its own, the particle will not be able to pass it. However, as is well known, tunneling is observed for microscopic particles and requires a quantum mechanical treatment. Given the wave nature of matter, an incident particle may have a finite probability

of existing on the other side of a potential barrier. Within the region of the barrier, the particle can not exist and its wavefunction decays evanescently. If the evanescent wave reaches the other side of the barrier where it can exist once more, then the particle can tunnel.

Tunneling is commonly introduced from a free space region through a barrier to another free space region. This approach is instructive, but it is relatively uninteresting compared to what is possible experimentally. Instead, it is significantly more enlightening to tunnel from one material to another. By setting the energy of an incident particle from one material, the presence of a resonant energy state in the other material can be inferred through the measurement of a tunneling event, where the rate of tunneling is described by Fermi's Golden Rule. Tunneling can be either be characterized as being elastic or inelastic. In elastic tunneling, the energy of the particle is conserved whereas in inelastic tunneling, the particle has either gained or lost energy by a scattering event. Elastic tunneling events can be used to measure the presence of available states in a material directly, whereas in inelastic events we can measure the energies of excitations that can be scattered off of.

## 2.2 Planar Tunneling Junctions

Early tunneling experiments between materials were carried out between planar metal electrodes separated by an insulator, usually aluminum oxide. The barrier was initially treated as vacuum, and the resulting tunneling current depended on the density of states at the Fermi energy of both metals [81]. Famously, Giaever used a planar

tunneling junction to measure the energy gap in superconductors [82]. Inelastic tunneling experiments were also used to measure phonon modes of the barrier material or dopants embedded within [83]. Notably, in a planar tunneling junction, both energy and in plane momentum are conserved [84, 85], requiring a match in energy and momentum between the initial and final states. By comparison, in STM, the atomically sharp tip does not have a defined crystal momentum and is insensitive to it. Momentum conserved tunneling was eventually explored within semiconductor tunneling junctions where tunneling would occur when the Fermi surfaces of the two electrodes would overlap [84, 85]. An inplane magnetic field was often used to change the separation of the Fermi surfaces in momentum space as an electron picks up an impulse from the Lorentz force during its tunneling. The resultant change in momentum is proportional to the magnetic field and thickness of the barrier. This approach has been built on in various ways with electrical pump probe experiments and full energy momentum resolution [86, 87]. Researchers now perform planar tunneling junction experiments between 2D materials; however few focus on momentum resolution and tend to be performed at fixed angles [88–95].

## 2.3 Twistable Planar Tunneling Junction

To perform momentum resolved spectroscopy of 2D materials, we need a way to tune the energy as well as the relative momentum of tunneling electrons. A twistable planar tunneling junction can do both. In this section, we investigate how this can be realized between two graphene layers separated by a $WSe_2$ tunneling barrier, where one graphene layer acts as a probe and the other acts as a sample.

As mentioned previously, a relative rotation between layers in real space rotates the reciprocal lattice vectors of the layers with respect to each other creating a superpattern periodicity. This rotation in k-space also rotates the bands such that a difference in crystal momentum between layers develops. The K point Dirac cones of the sample and probe layers become separated in k-space such that the quasiparticles between layers have different crystal momenta as can be seen in Figure 2.1.

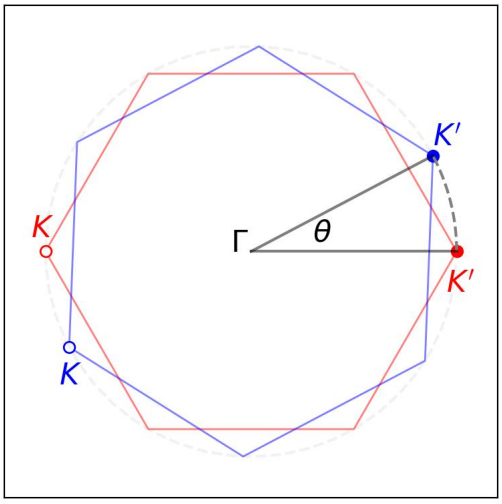


Figure 2.1: Two honeycomb lattices twisted with respect to each other, imparting momentum offset shown by the dashed gray line. One layer is in red and the other layer is in blue.

The separation as a function of twist is simply the arc length

$$\Delta k = |K|\theta \tag{2.1}$$

where $|K|$ is the magnitude of the distance between the $\Gamma$ and $K$ points and $\theta$ is the relative twist between layers. We can use this twist between layers to tune the relative momentum of electrons supplied from the K points of the probe graphene layer to

the K points of the sample, allowing us to take a line cut through the sample's band structure at the K point.

The energy of tunneling electrons can be tuned with an external bias as is done in STM and other tunneling experiments. The relationship between bias and energy can be understood by modeling the tunnel junction as a parallel plate capacitor. For simplicity, let us begin by with the case where we have two perfect conductors separated by a dielectric.

**Electrostatics of High Density of States Metal Parallel Plate Capacitor**

Applying a bias, $V_B$, across a standard parallel plate capacitor causes a charge, $Q$, to build up on the plates depending on the geometric capacitance, $C$, of the capacitor.

$$V_B = Q/C \tag{2.2}$$

The bands also become offset by $\phi$, corresponding to the applied bias as shown in Figure 2.2.

$$eV_B = \phi \tag{2.3}$$

**Electrostatics of Graphene Based Parallel Plate Capacitor**

We now turn our attention to our graphene based capacitor. It is similar, but the low density of states near charge neutrality alters the electrostatics. Whereas adding charges to a high DOS material does not change the chemical potential noticeably, adding electrons to charge neutral graphene will increase the chemical potential. This effect is known as electronic compressibility and leads to quantum capacitance [96,97].

With this we get the following equation,

$$eV = \mu_B - \mu_T - \frac{eQ}{C_{geo}} \tag{2.4}$$

where $\mu_{T,B}$ are the chemical potentials of the top and bottom electrodes. By keeping track of energies, we also get the condition shown in Figure 2.3:

$$eV_B = \phi + (\mu_T - \mu_B) \tag{2.5}$$

Here, it is assumed that there is no independent electrostatic doping of the individual layers such that $\mu_T = -\mu_B$ as in [7]. To solve for these equations self consistently, we write the accumulated charge as the charge of an electron times the density of states, $n(\mu)$, and use the familiar expression for the capacitance of a parallel plate capacitor.

$$n(\mu) = \text{sign}(\mu)\frac{\mu^2}{\pi\hbar^2 v_f^2} \tag{2.6}$$

$$C_{geo}/A = \frac{\varepsilon_r \varepsilon_0}{d} \tag{2.7}$$

Altogether now,

$$eV = 2\mu - \frac{e^2 \text{sign}(\mu)\mu^2 d}{\pi\hbar^2 v_f^2 \varepsilon_r \varepsilon_0} \tag{2.8}$$

using two layers of $WSe_2$ as the dielectric tunneling barrier with $\varepsilon_r = 4.63$ and layer thickness of 0.58 nm, we solve for $\mu$ and $\phi$ as functions of the applied bias, $V_B$, in Figure 2.4.

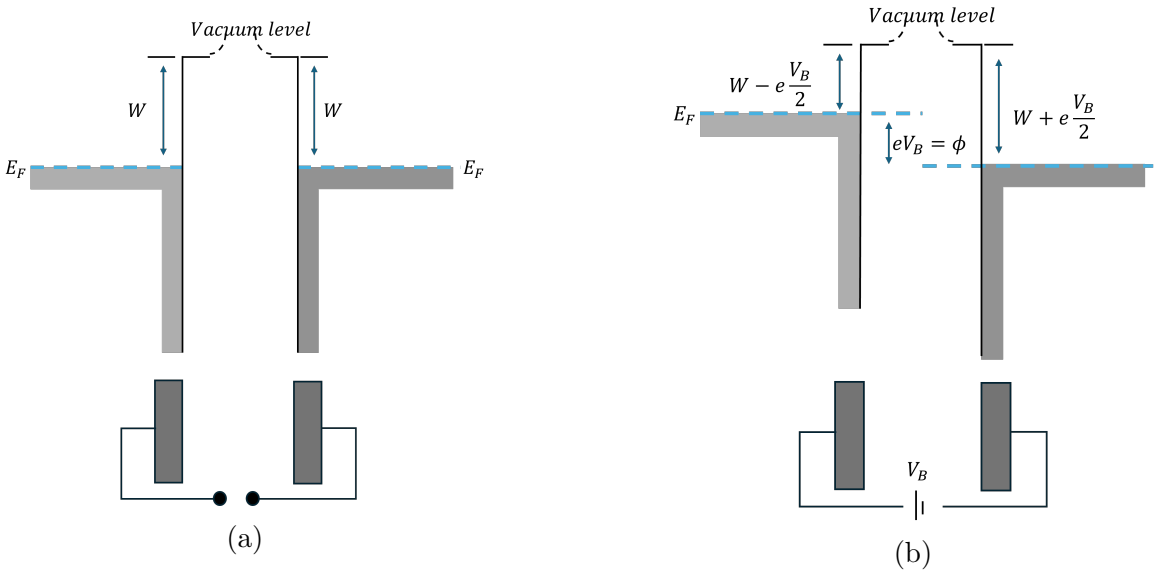


Figure 2.2: Bands of metal electrodes in parallel plate capacitor. a) Fermi energies aligned b) Fermi energies offset by an applied bias

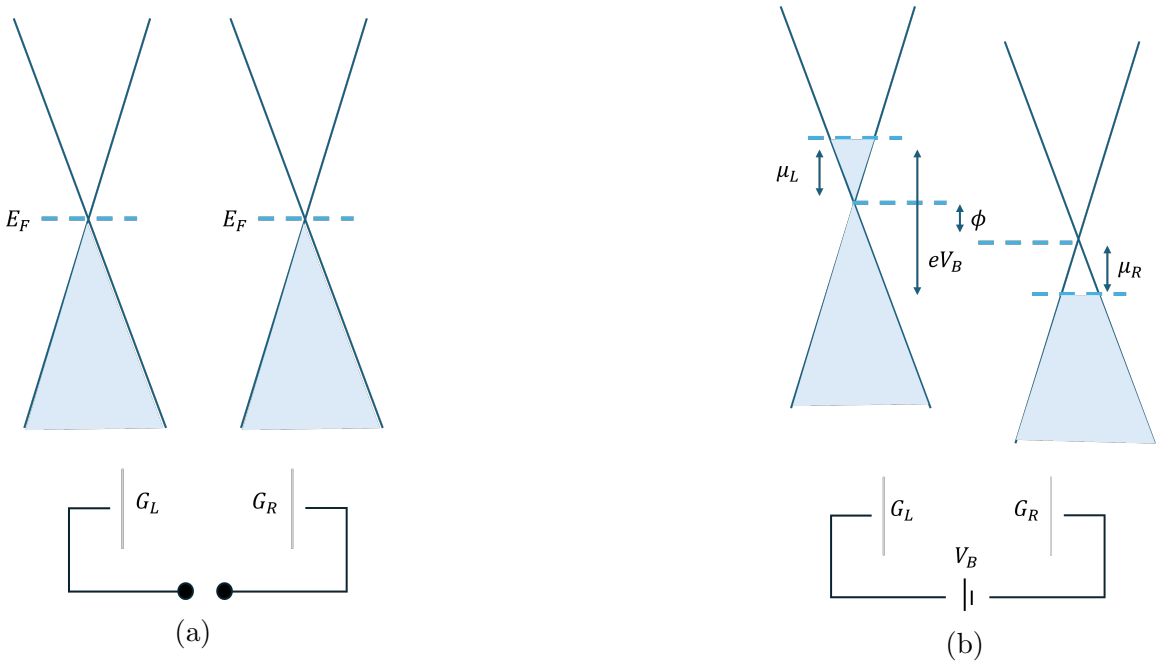


Figure 2.3: Bands of graphene electrodes in parallel plate capacitor. a) Bands and Fermi energies aligned b) Bands and Fermi energies no longer aligned as the result of an applied bias

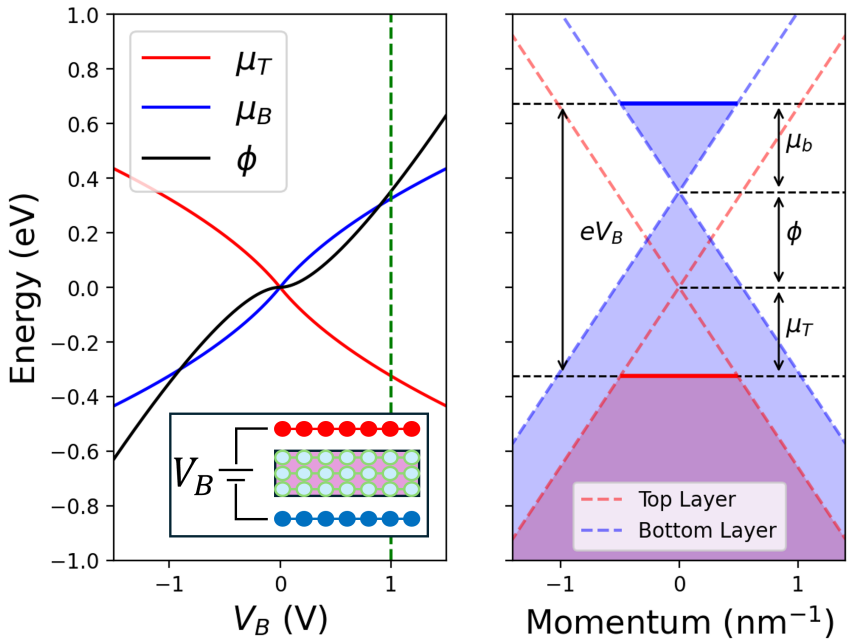


Figure 2.4: Solution to electrostatics of graphene based parallel plate capacitor where B and T subscripts label the graphene electrodes. Left: $\phi(V_B), \mu_T(V_B), \mu_B(V_B)$ with vertical line at 1V. Inset depicting the top and bottom graphene electrodes separated by a $WSe_2$ tunnel barrier forming the parallel plate capacitor. Right: Depiction of the graphene bands at the 1V solution.

### Tunneling Current

We now have an understanding of how an external bias applied across the graphene to graphene tunneling barrier alters the relevant energies and how a twist between the graphene layers induces a momentum offset. Let us calculate the tunneling current as a function of both, where we assume only elastic momentum conserved tunneling events are allowed. The tunneling current is then proportional to the integral over all momentum and energy matching states within the energy window available for

tunneling [76],

$$I_T \propto \int dE\{\underbrace{(f_B(E) - f_T(E+\phi))}_{\text{Term 1}} \underbrace{\sum_{k_B,k_T} |T^{\alpha\beta}_{k_B,k_T}|^2 A_B(k_B,E) A_T(k_T,E+\phi)\}}_{\text{Term 2}} \quad (2.9)$$

where $f_{B,T}$ are the Fermi Dirac distributions for the distinct layers, $|T^{\alpha\beta}_{k_B,k_T}|$ is a tunneling constant, and $A_{B,T}$ are the spectral functions of the top and bottom graphene layers. The spectral functions are related to the imaginary component of the Green's function representing the response of the crystal from adding an electron with a given momentum and energy. It captures the band structure of graphene, including Lorentzian broadening as a result of the finite lifetime of the quasiparticle [98, 99].

$$A_{T,B}(k,E) = \frac{2\gamma}{(E - \epsilon_{T,B}(k))^2 + \gamma^2} \quad (2.10)$$

where $\gamma$ is the inverse lifetime and $\epsilon(k)$ are the graphene dispersions in each layer. We use a model for $\gamma$, as employed in experiments to best fit the data, $\gamma = 4 + 0.035|E-\mu|$ eV [7, 95]. The spectral function for an individual graphene layer with line cuts at specific energies is shown in Figure 2.5.

Term 1 of Equation 2.9 is shown in Figure 2.6 and acts as a boxcar filter that selects the energies available for tunneling. The available energies are dictated by $\mu_{T,B}$ and $\phi$ which are functions of the applied bias. Its sign dictates the direction of tunneling and the sharpness of the cutoff is a result of $k_BT$, set to 25meV here.

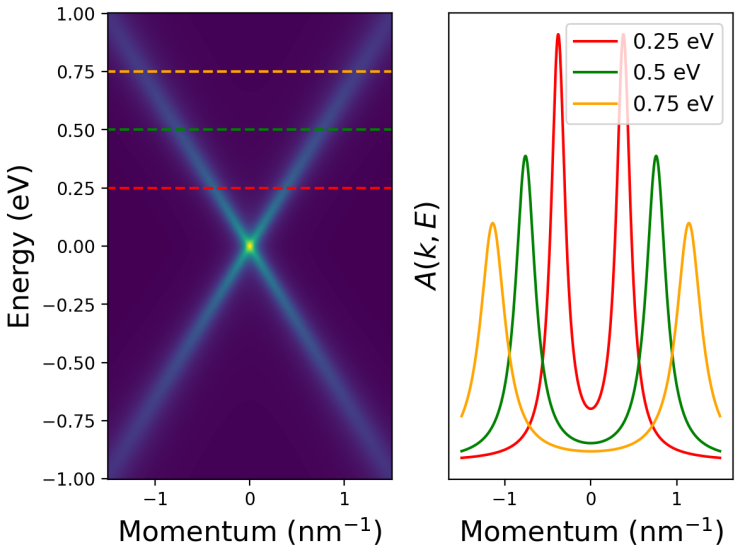


Figure 2.5: Spectral function of a graphene layer. The amplitude is a dimensionless quantity indicating the probability of a state. Left: Spectral function of graphene layer with dimensionless units colour scale Right: Slices of the spectral function at different energies to show the effect of spectral broadening.

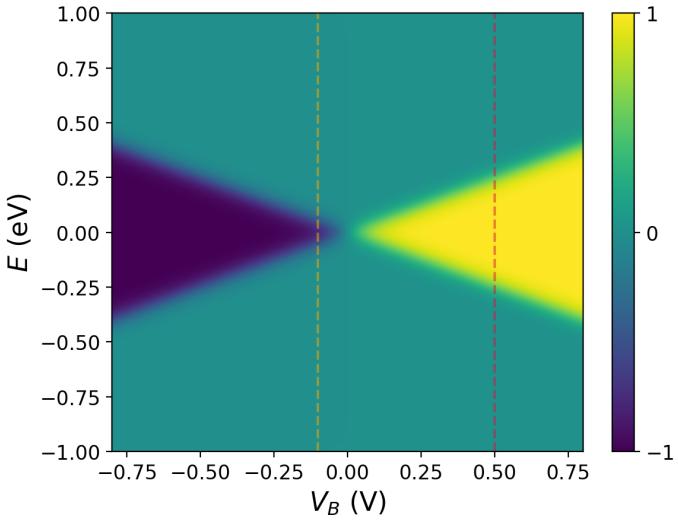


Figure 2.6: Term 1 of Equation 2.9 as a function of $V_B$. The colour scale is dimensionless and indicates the availability of energy states for tunneling and the sign represents the direction of tunneling. Energies shown in the centre colour (turquoise) are outside of the energy range where tunneling is possible. Vertical cuts at two different applied biases are shown in Figure 2.7.

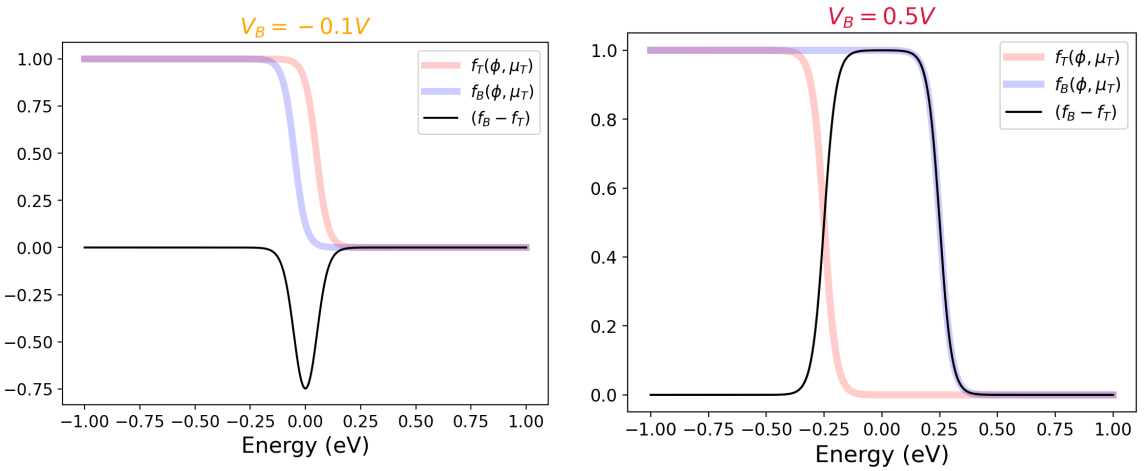


(a) (b)

Figure 2.7: Vertical line cuts from Figure 2.6. The y axis is unitless. The red and light blue lines represent the individual Fermi-Dirac distributions from each respective graphene layer and the black line represents the difference between the two. a) -0.1V b)0.5V

Term 2 of Equation 2.9 sums every combination of momentum states between layers at a fixed energy. Conservation of momentum is enforced by setting

$$|T^{\alpha\beta}_{k_B,k_T}|^2 = |T|^2 \delta_{k_T,k_B} \tag{2.11}$$

where $\delta_{k_T,k_B}$ is the Kroenecker Delta symbol. For simplicity, unique from [7], we assume $|T|^2$ is a constant. As such, effects leading to the tunnel barrier breakdown such as $WSe_2$'s finite band gap and Fowler-Nordheim Field emission will not be captured.

The product of the two spectral functions captures the amplitude of overlap between states in the top and bottom graphene layers with equal energy and momentum. The spectral functions are offset in energy by $\phi(V_B)$ and in momentum by the relative

twist angle $\Delta k(\theta)$. Figure 2.8 shows examples of the product between the spectral functions under various offsets, without the effect of Term 1. The individual spectral functions are indicated by black and white dashed lines. The product peaks where the bands from different layers intersect, indicating a potential for a tunneling transition. This is distinct from the crossing of the valence and conduction band within an individual layer's spectral function. We see that the bias and twist shift the energy and momentum of the intersections between the spectral functions.

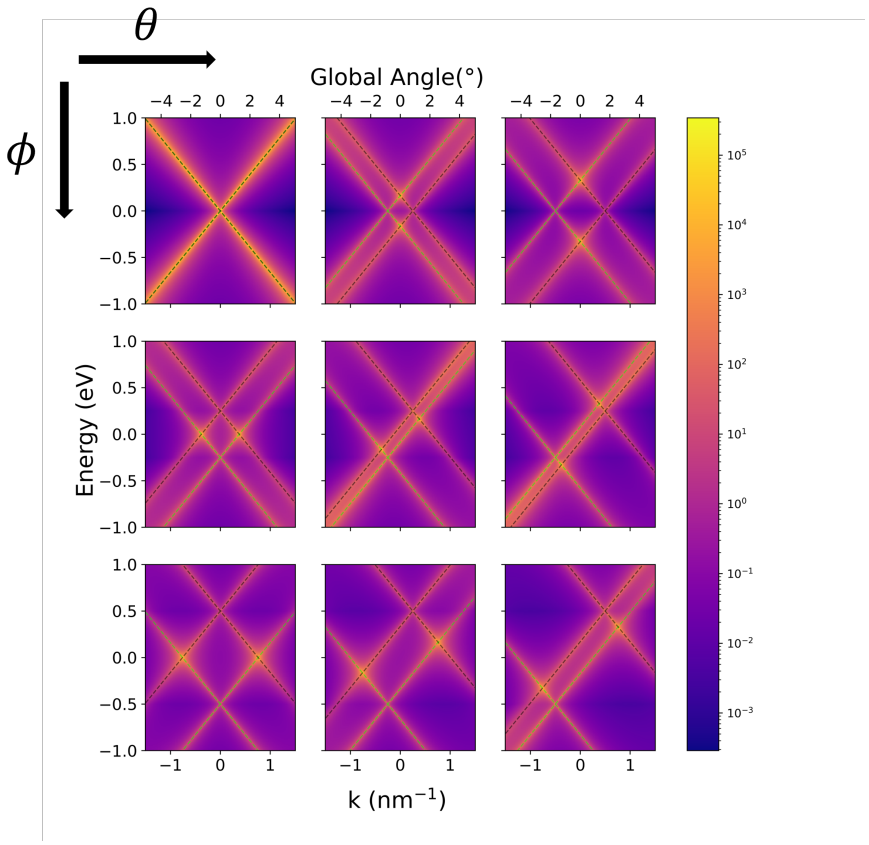


Figure 2.8: Schematic demonstrating the effect of the band offset $\phi(V_B)$ and twist between layers $\theta$ on the product of the spectral functions. The spectral functions from the two layers are overlaid with different colours such that separation in momentum can be distinct from separation in energy. Going vertically between panels, $\phi$ is changed. Going horizontally between panels, $\theta$ is changed.

Now, we look at the effect of the Fermi-Dirac window on an arbitrarily biased and rotated junction in Figure 2.9. The window clearly filters out the energies that are not available for tunneling such that only relevant momentum and energy conserved transitions are counted. Summing over all energy and momenta results in a value proportional to the tunneling current. In the depicted alignment, the two spectral functions cross within the energy window which would result in a tunneling current.

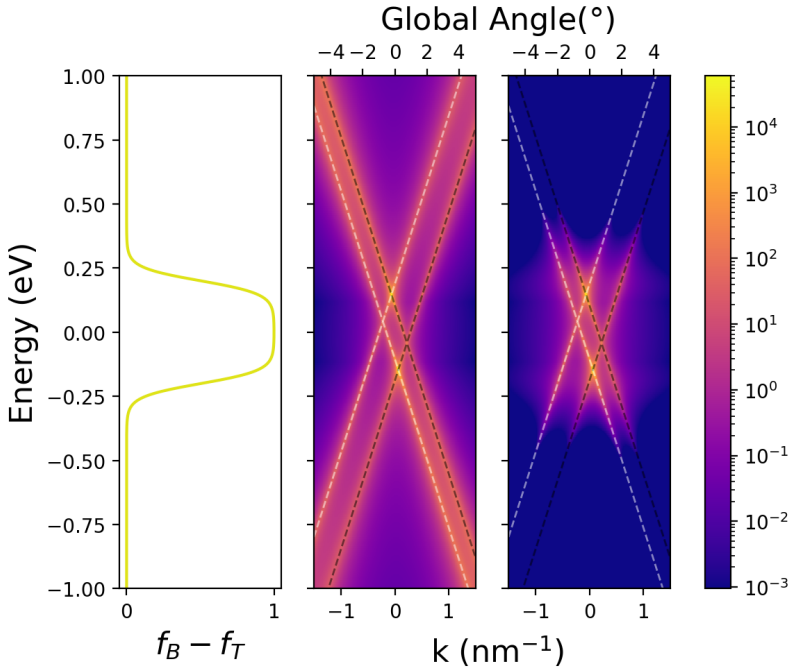


Figure 2.9: Schematic demonstrating the effect of applying the Fermi Dirac windowing on the product of the spectral functions at an arbitrary twist and bias across the graphene based capacitor. Left: Fermi Dirac window, Middle: Product of the two graphene layer spectral functions, Right: Product of the spectral functions multiplied by the Fermi Dirac window.

The calculation of Equation 2.9 over a range of applied biases and relative twists, results in Figures 2.10. The tunneling current changes sign between positive and negative applied bias as expected from Term 1. Notably, there are also two key

features found in the calculated $I$ and $dI/dV$ plots: a high current feature highlighted by a white dashed line and a border separating regions in the plot with and without a tunneling current overlaid with a black dashed lines.

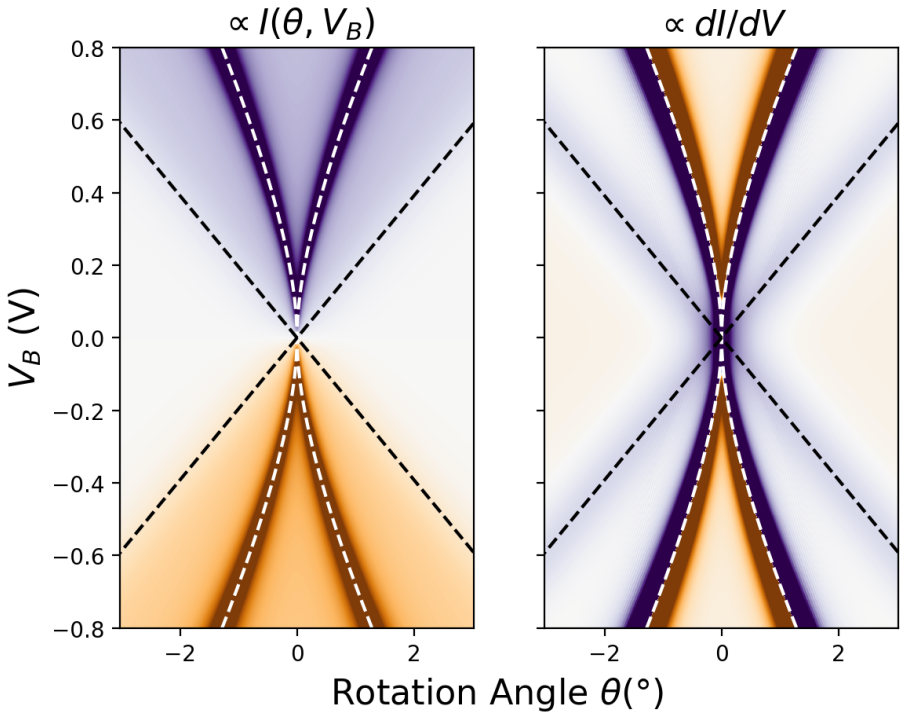


Figure 2.10: Calculated tunneling current as a function of $V_B$ and $\theta$ with nesting and onset tunneling conditions overlaid from Figures 2.11 and 2.12. Purple corresponds to a positive current or derivative, and orange corresponds to negative current or derivative and white corresponds to zero current or derivative. Left: Tunneling current Right: Derivative of tunneling current.

I will walk you through these features by looking at their band alignments. In Figure 2.11, the highlighted features are marked with black markers, indicating the bias voltages and twist angles for which the corresponding band alignments are shown in Figure 2.12. On the marked triangle, associated with the high current feature, the bands are nested in such a way that there are many energy momentum matching

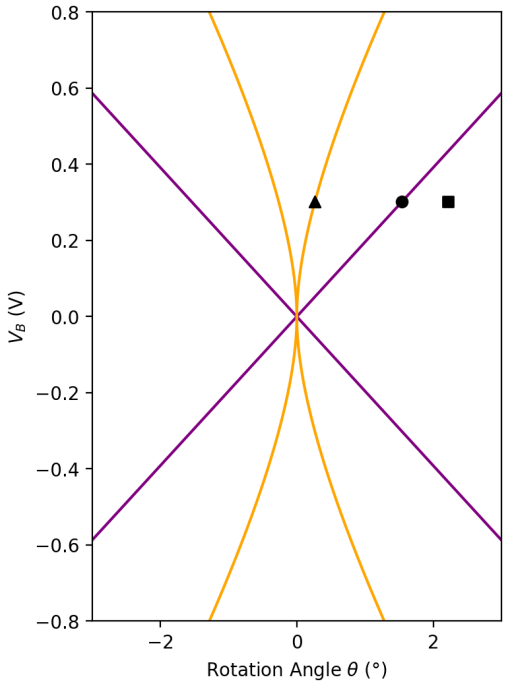


Figure 2.11: Different tunneling features and current conditions as seen in Figure 2.10. The orange curve represents the nesting condition. The purple curve represents the tunneling onset condition. The graphene bands at the twist and bias marked by the triangle, circle and square markers are shown in Figure 2.12.

states. This occurs when

$$\phi = \pm\hbar v_f |K_D|\theta \tag{2.12}$$

This feature gives a direct readout of the band offset $\phi$ as a function of $V_B$. As discussed when solving the electrostatics of the junction, the offset and applied bias are intimately linked to the chemical potential of the layers. From this, the geometric and quantum capacitance can be extracted. Going from the triangle to the circle, the twist angle is increased leading to an increase in the momentum separation between the layers. We see that at this separation, the system reaches a critical point at which

the bands are maximally separated, while states remain accessible for tunneling. This minimum separation onset condition occurs when

$$\phi + 2\mu = \pm\hbar v_f |K_D|\theta \tag{2.13}$$

$$V_B = \pm\hbar v_f |K_D|\theta \tag{2.14}$$

This expression is effectively the band structure of graphene as $|K|\theta$ is a trace through the $K$ point in reciprocal space. This can be used to extract the $v_f$ for instance. From the circle to the square, the separation is reduced further such that there are no states available for tunneling and as a result there is not tunneling current recorded.

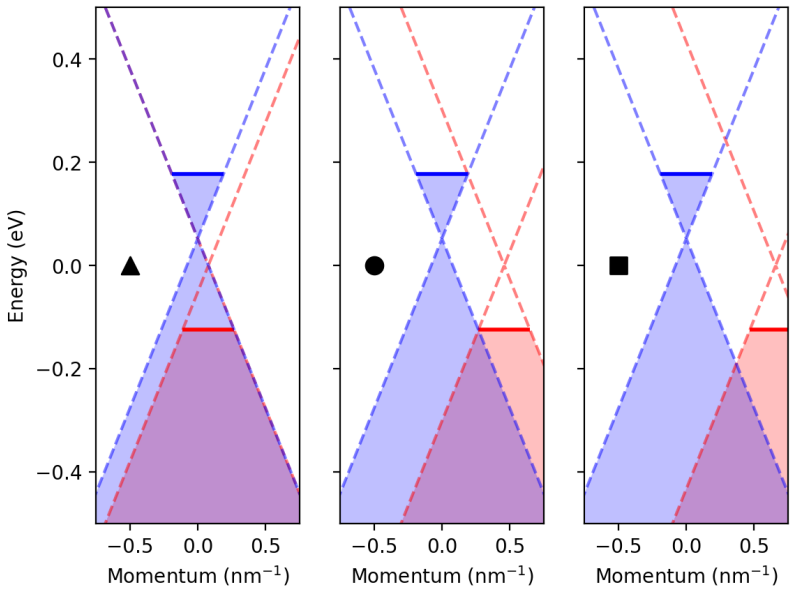


Figure 2.12: Graphene bands of top and bottom layers at three different twist angles and biases marked in Figure 2.11 Left: Triangle marker placed on the nested feature leading to high tunneling current. The bands of the two layers are nested such that there are many states available for tunneling. Middle: Circle marker placed at the tunneling onset condition. The bands are at the separation in k-space where there are states available for tunneling. Right: Square marker placed outside of the tunneling onset condition. At this bias and twist angle there are no available states for tunneling.

### 2.3.1 Discussion

This chapter demonstrates how graphene can be used as a probe to trace out the bands of a graphene based sample in what is now being called Dirac point spectroscopy [9]. The graphene probe supplies electrons at a given energy and momentum relative to the graphene based sample. If there is a match between an empty and filled state, then a tunneling current can take place. This effectively allows us to take a line cut of the bands around the K point of the sample. Since all graphene based samples have their Dirac cones or hybridized Dirac cones at the same distance from the Γ point, we can always trace them out with a graphene Dirac cone probe. Figure 2.13 depicts the relevant angles when probing a twisted bilayer graphene sample. A bilayer sample is initially fabricated with a fixed angle, and the Dirac cones, at $K_{layer1}$ and $K_{layer2}$, from the two layers can hybridize in between. The monolayer graphene probe can then be continuously rotated with respect to the twisted sample to probe its bands. Examples of the tunneling current model implemented where graphene traces out bands resembling those of twisted bilayer graphene can be found in Appendix E.

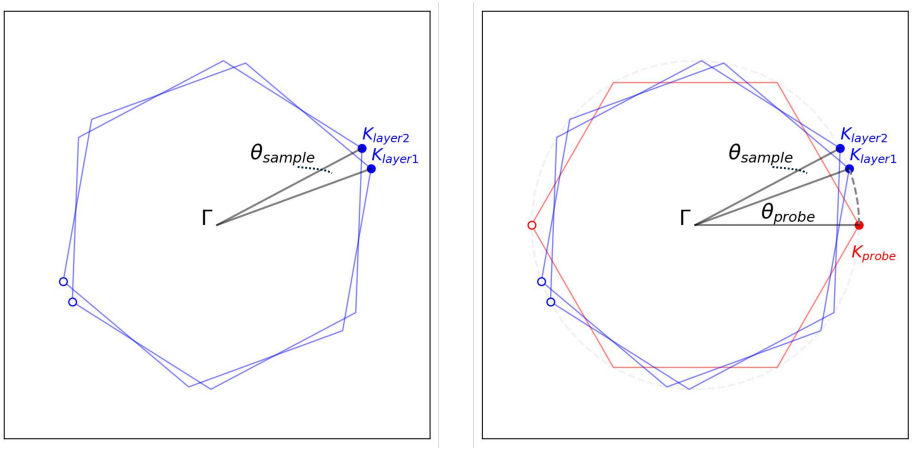


Figure 2.13: Monolayer graphene probe used to probe twisted bilayer graphene sample. Blue: Twisted bilayer graphene sample, Red: Monolayer graphene probe. Left: Twisted bilayer graphene sample with a fixed angle, $\theta_{sample}$. Its K points are separated in crystal momentum by this twist, and when sufficiently close, they hybridize to form flat bands. Right: Monolayer graphene probe with continuously twistable angle, $\theta_{probe}$, with respect to the twisted bilayer graphene sample. This twist angle is used to take a line cut through the K points of the twisted sample.

However, a graphene probe can not be used to measure the K point dispersion relation of all materials. For instance, a graphene probe could not easily be used to measure the K point dispersion of a TMD sample as the graphene probe would not pass through the K point of the TMD [100, 101]. The inherent momentum offset between materials with different lattice constants resulting in different $|K|$ point is demonstrated in Figure 2.14. To account for the inherent momentum offset, a rotating external magnetic field could potentially be used. To perform this momentum resolving measurement at the K point of materials, like materials should be used on the probe and sample [7].

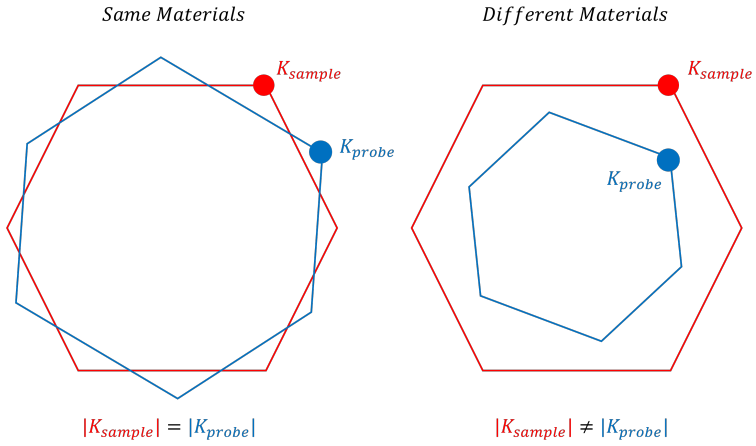


Figure 2.14: Demonstration of the requirement for $|K|$ to match between sample and probe. Left: When both are equal, as with graphene to other graphene based samples, the graphene probe can take a line cut through the sample's K point dispersion relation. Right: When both are different, the graphene probe will not trace a cut through the sample's K point dispersion relation.

## 2.4 Other QTM Experiments

### 2.4.1 Backgated Sample and Probe

By adding another dielectric and conductive electrode to the probe and sample, both can be backgated such that their chemical potentials can be tuned independently. For example, to study electron correlation effects, it would be necessary to be able to tune the carrier density with more control.

### 2.4.2 Twistable Inelastic Planar Tunneling Junction

In this section, only elastic momentum conserved tunneling is discussed; however, inelastic momentum conserved events do take place within these junctions. Analogous to the experiments described in [83], but with momentum resolution, inelastic events can be recorded to map out the dispersion relations of the excitations that the electrons are scattering off of. This has recently been realized to measure graphene phonon modes and their coupling to electrons [10, 11]. There are also proposals to record other quasiparticles such as plasmons [12] or those in proposed quantum spin liquids [13].

### 2.4.3 Tunneling Through Point Defects

While distinct from the other schemes described, with no twisting or conservation of momentum, it is worth mentioning that this system can be used to measure the electrostatic potential of a material on one side of a 2D material interface through tunneling into point defects. At low temperatures, the point defects behave as quantum dots and become sensitive to the local potential of the material on the interface. This has been used to extract the electrostatic potential resulting from a moiré potential of graphene aligned to hBN [15].

# Chapter 3

# Implementation

At this point of the thesis, the reader should understand the motivation for an experimental technique capable of creating twistable 2D material planar interfaces. Now, we discuss the implementation of a QTM to facilitate these interfaces and their electrical characterization. The system is built around a commercial AFM. To establish a junction, one half of the interface is placed on an AFM tip while the other half lies on a sample substrate. The halves of the junction are brought together using the AFM's contact mode capabilities with a custom stage enabling rotation. Electrical measurement equipment then characterizes the interface through the collection of an out of plane current.

The implementation requires a custom AFM tip, a custom sample substrate, new methods, a custom set of stages and electrical equipment. I begin with a description of the custom AFM tip as it imposes constraints on the rest of the system. I then outline the adaptations required to accommodate these constraints, namely a custom set of stages and procedures to fabricate necessary sample substrates. The electrical

measurement equipment is described and finally, I go over new methods that were developed to transfer 2D materials and heterostructures to the necessary structures.

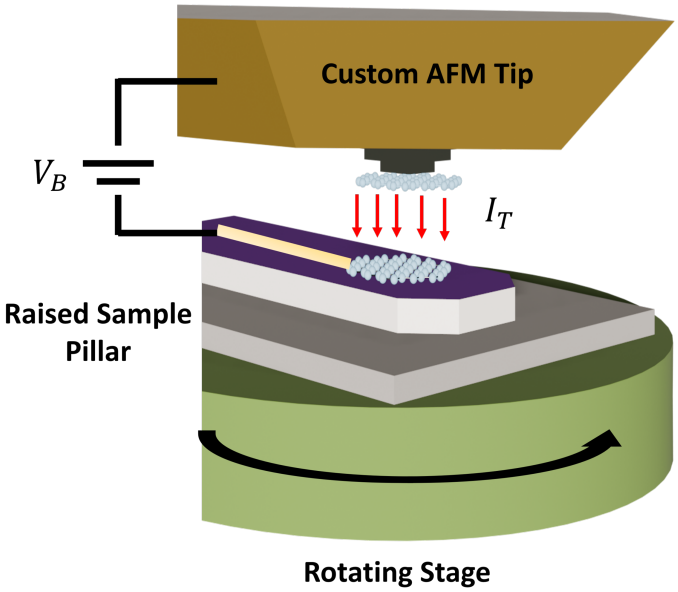


Figure 3.1: Schematic displaying the key components of a QTM system consisting of a custom rotating stage, a raised sample pillar and a custom AFM tip.

## 3.1 Custom AFM Tip

The key to the QTM is an electrically contacted vdW tip. Conventional AFM tips are generally tall and sharp such that they have good spatial resolution and can resolve deep features. For our application, spatial resolution is not of chief concern, and the main requirement is that our tip must allow for a 2D material to be placed on top, forming a flat apex. These conditions are met with a significantly shortened tip of 1-2um with a flat apex of approximately 50nm. The tip must also be placed on the cantilever with sufficient room from the edges such that there is enough area for flakes to conform and stick. These conditions require a custom tip. When a vdW material

is eventually transferred to one of the custom tips, they form a flat plateau at the apex with area sizes ranging from 50nm to 1-2um depending on the thickness of the flakes [7].

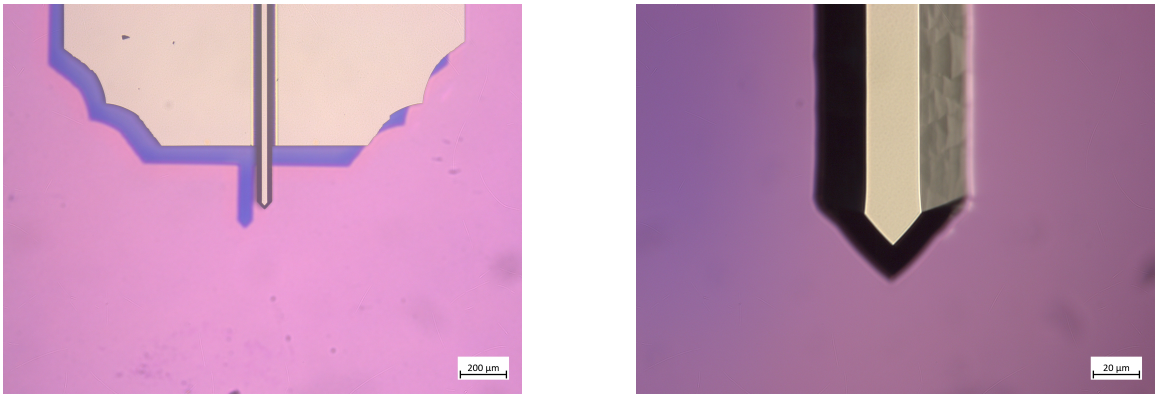


(a) (b)

Figure 3.2: Optical microscope images of a commercial tipless cantilever at magnifications of a) x20 and b) x50.

First, commercially available tipless cantilevers are purchased, as shown in Figure 3.2. The cantilevers are then loaded into an evaporator chamber to be coated with Cr/Au (3nm/100nm), as shown in Figure 3.3, to enable conductivity measurements. The Cr adhesion layer is evaporated with an e-beam source and the gold is thermally evaporated. The custom tips are then grown on top of the conductive cantilevers. The tips are made of platinum that has been deposited by focused ion beam (FIB) deposition at the Canadian Centre for Electron Microscopy (CCEM). In this process, the cantilever is placed in a vacuum chamber flooded with a Pt containing precursor gas. A focused ion ($Ga^+$) beam is then directed at the end of the cantilever where the operator intends to deposit material, causing the precursor molecules to dissociate, depositing the metal [102]. The tip structures are pyramids composed of eight square layers of roughly equal thickness. The layers are grown layer by layer from the base,

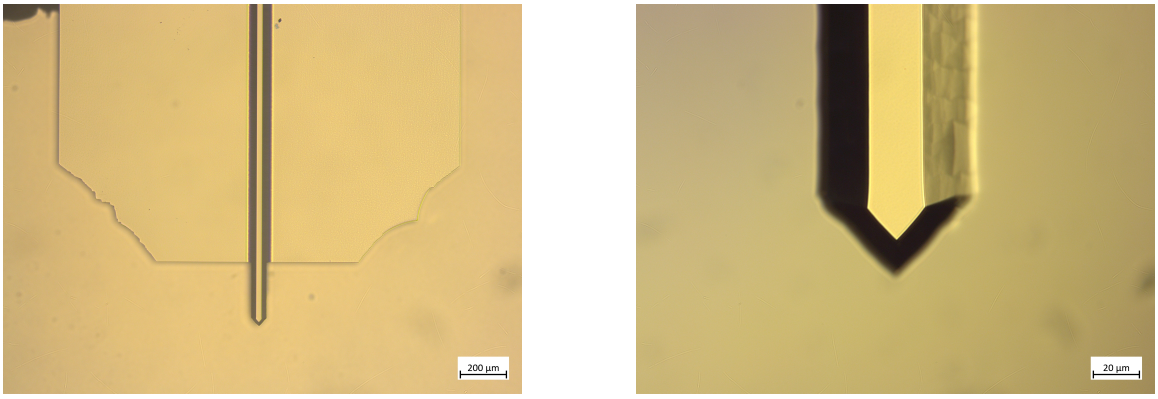


(a) (b)

Figure 3.3: Optical microscope images of commercial tipless cantilever after Cr/Au film deposition at magnifications of a) x20 and b) x50.

with each added layer being smaller in area. The apex is not directly deposited at 50nm, but is instead milled down from a larger layer. The tip is deposited approximately 10um from the edges of the cantilever. Images of the cantilevers with the custom tips are found in Figures 3.4 and 3.5.

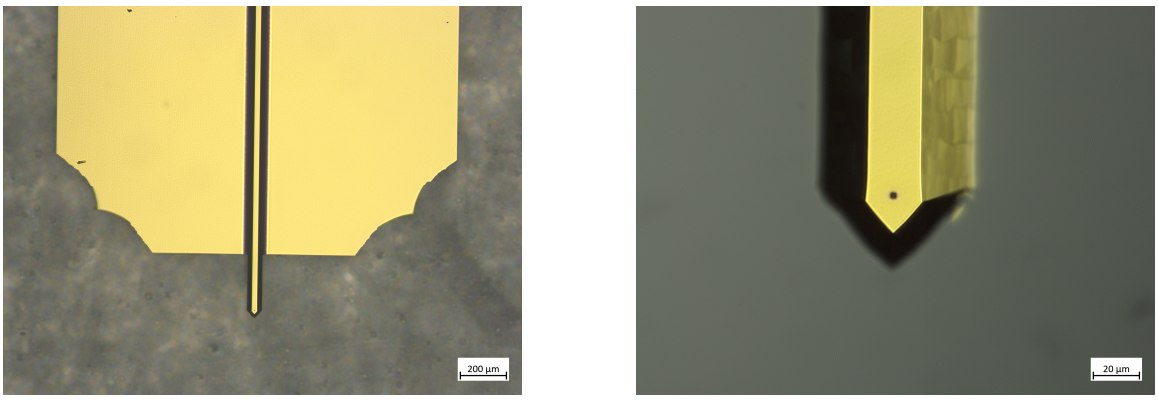


(a) (b)

Figure 3.4: Optical microscope images of commercial tipless cantilever after Cr/Au film deposition and FIB deposition of custom tip at magnifications of a) x20 and b) x50.

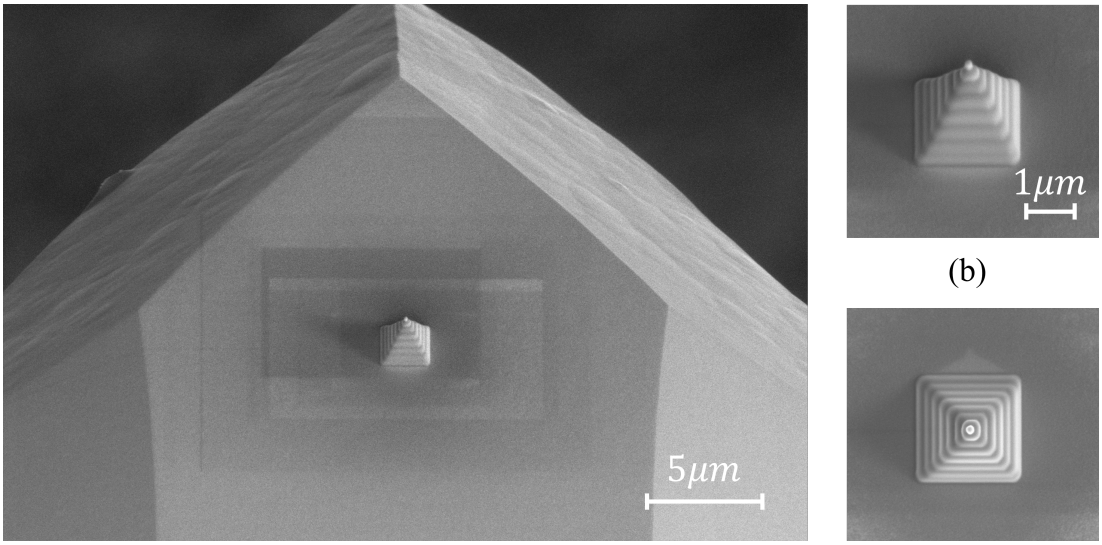


Figure 3.5: FIB images of custom Pt tip deposited at the end of an AFM tip via FIB deposition. a) 52° tilt b) 52° tilt c) 0° tilt

Once the tips have been deposited, vdW materials or heterostructures can be transferred to them by techniques described in Section 3.6.

## 3.2 Geometric Constraints

The short custom tip accommodates vdW material transfers, but imposes geometric constraints on the sample substrate and stage. Solutions to these constraints are illustrated in the schematic sets shown in Figure 3.6. AFM heads are designed such that the probe holder tilts the cantilever down towards the sample at a defined fixed angle. For standard tall tips, this poses no issue during tip engagement. However, our shorter custom tip deposited 10um from the cantilever edge presents an issue when landing. The tip can contact the substrate if we angle the sample to match

the inclination of the probe. This should also help to ensure that we form a planar interface. Finally, to minimize collisions between the substrate and any part of the AFM probe or probe holder, the sample is placed on a custom raised pillar.

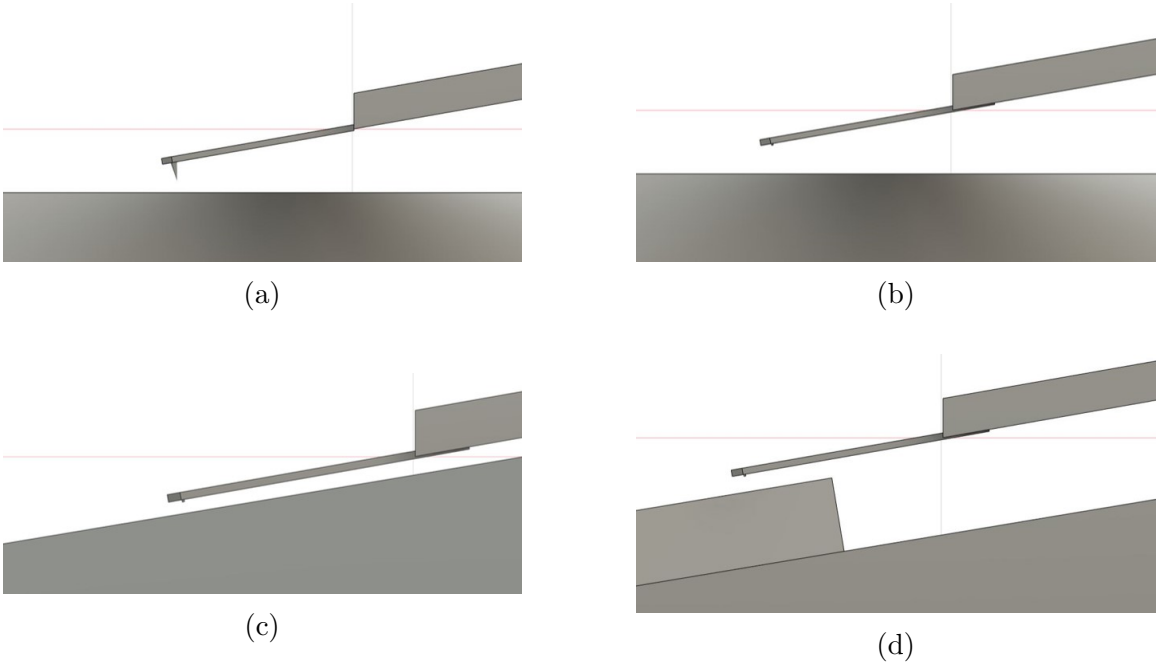


Figure 3.6: Schematics depicting the necessary considerations when engaging a short custom AFM tip to a sample. a) Commercial AFM tip engaging with sample held at a typical AFM tip tilt angle. b) Custom AFM tip engaging with sample held at a typical AFM tip tilt angle. The tip is not tall enough to engage the surface before the edge of the cantilever. c) Custom AFM tip engaging with an inclined sample to match the typical AFM tip tilt angle. The tip is now able to engage. d) Custom AFM tip engaging with an inclined and tall sample to match the typical AFM tip tilt angle. The tall sample provides more space to minimize collisions during engagement.

## 3.3 Custom Stage

A custom stage is required to successfully allow our custom tip to land and to enable in situ rotation. The components of the custom stage, shown in Figure 3.7,

include a mounting solution compatible with the existing system, an angled base, and integrated rotational functionality.

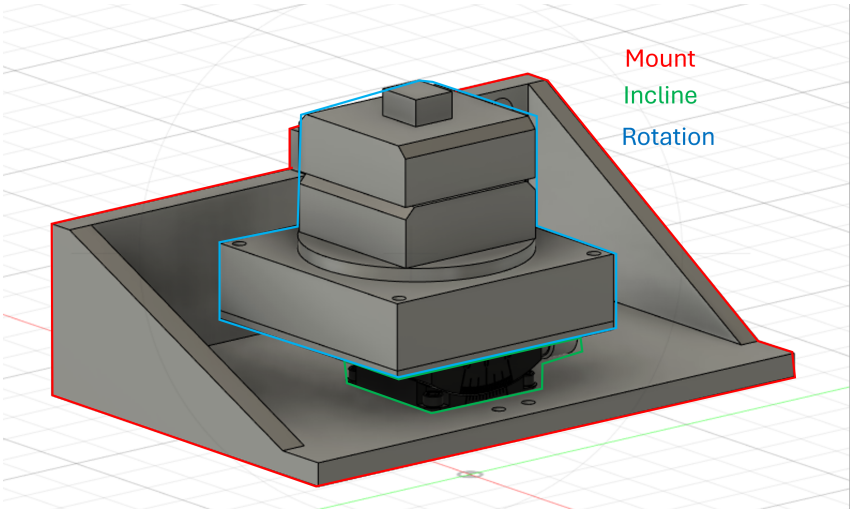


Figure 3.7: Schematic of three components comprising the custom sample stage. In red, a mount to the existing system, in green a component to tilt the sample, in blue a set of stages to enable rotation in plane.

The presented solution is for a Bruker ScanAsyst AFM, but can be generalized to other systems. The mount secures the rest of the stage components to the base of the AFM. An inclined plane must be placed on top to match the angle of inclination of the cantilever as set by the AFM head. The rotation enabling components are placed on top of the angled base such that rotations can be performed in the correct plane and maintain contact with the interface as shown in Figure 3.8. The rotation functionality is achieved with a rotating stage and a set of xy positioners. The xy positioners are placed on top of the rotator to ensure that the sample can be moved to the centre of rotation (COR). A demonstration highlighting the need for this configuration is provided in Figure 3.9.

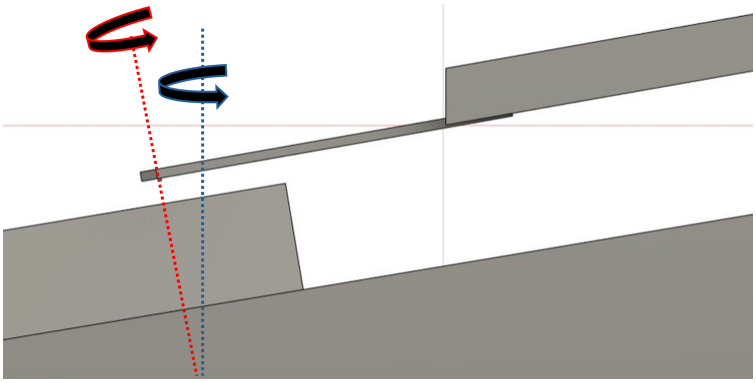

Figure 3.8: Schematic demonstrating the two possible planes to rotate in. In blue, if the rotator is not inclined, the rotation will be in the wrong plane. In red, if the rotator is inclined, the rotation will be in the correct plane.

In standard use of the Bruker AFM, the sample is placed on the coarse motorized stage, shown in Figure 3.10, that provides a large lateral travel range. Using the stage, the sample is approximately aligned to the AFM tip through use of the built in camera system, and the AFM head is lowered until the tip is engaged. Conveniently, the Bruker AFM's sample stage has two unused screw holes, which we used to attach our custom stage mount. This modification does not interfere with the standard operation of the AFM, allowing us to use the original alignment capabilities between the sample and tip. The custom mount acts as a sliding shelf with two slotted holes aligned to the existing screw holes as well as additional mounting holes for the rest of the custom stage, and is shown in Figure 3.11. The prototype was 3D printed to make iterations easily; however, a final version would ideally be machined.

The Bruker holds AFM probes at an angle around 12° from the horizontal. While a fixed angled wedge would be sufficient to match this, the inability to make adjustments if necessary motivated the use of a goniometer. Stepper or piezoelectric goniometers

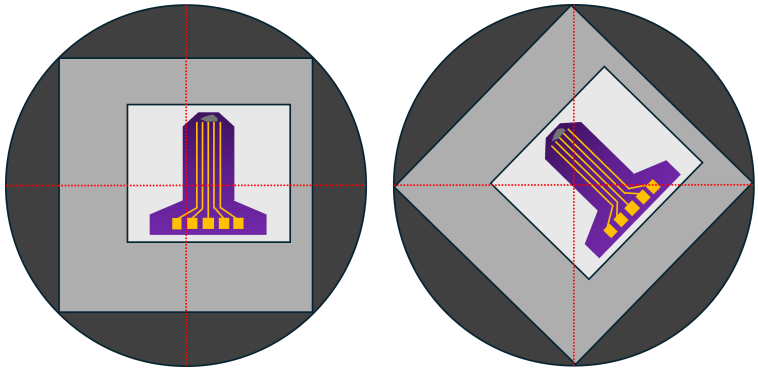

(a)

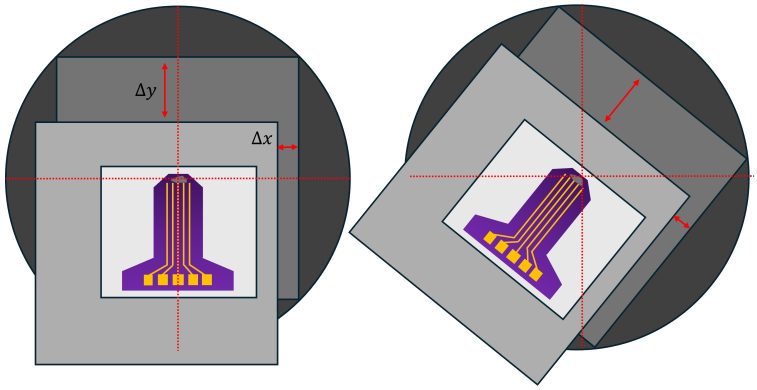


(b)

Figure 3.9: Schematics demonstrating the effect of rotating the stage with and without xy positioners on top. a) No xy positioners to centre the sample to the rotator's COR. Upon rotation, the sample moves laterally. b) xy properly placed on top of rotator such that the sample can be centred to the rotator's COR. Upon rotation, the sample does not move laterally.

add some convenience, but ultimately their use was decided against. The Thorlabs GN05 is sufficiently small, has a range of -15 to 15° and is very economical. While its official load limit is 115g, this was found to be greatly conservative when more than doubling the limit, and did not pose any issues. The rotator is then mounted to the goniometer with a 3D printed adapter plate allowing for the use of the threaded holes on the rotator and goniometer. The selected rotator is an Attocube ECR-5050hs

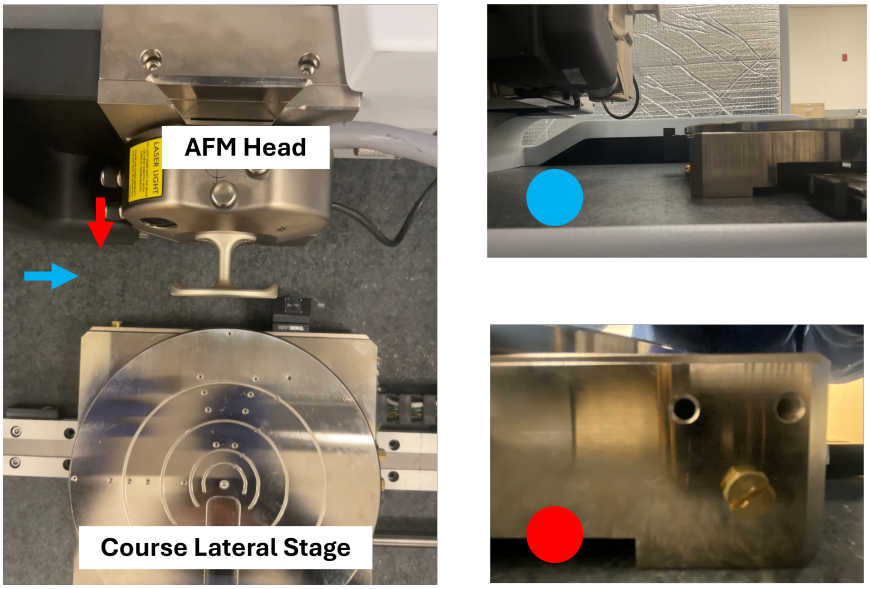


Figure 3.10: Bruker AFM system with different views. Left: Overhead view of course lateral stage and AFM head with two different views highlighted by red and blue arrows. Top Right: View from blue arrow showing spacing between head and course lateral stage. Bottom Right: View from right angle showing available screw holes for mounting custom stage.

piezoelectric motor with closed loop feedback, 0.001° sized steps and 360° range. This was selected for its size and resolution. xy stages required for centering the sample were not acquired at this point in the project, but ideally another set of Attocube piezoelectric stages, such as those from the ECX line, would be used such that only one controller interface is required and they can be mounted without any additional hardware. However, the main constraints on these xy stages are the height, the load relative to the limit on the selected rotator, the travel range and the step size. With sample substrate sizes on the order of 1x1cm$^2$, it would be prudent to have at least 1cm travel in each direction. A minimum step size of 1um is also warranted, with smaller being better. With 1um steps, being within 0.5um of the rotator's COR should be achievable. At 0.5um, a 30° rotation would yield a sample movement of

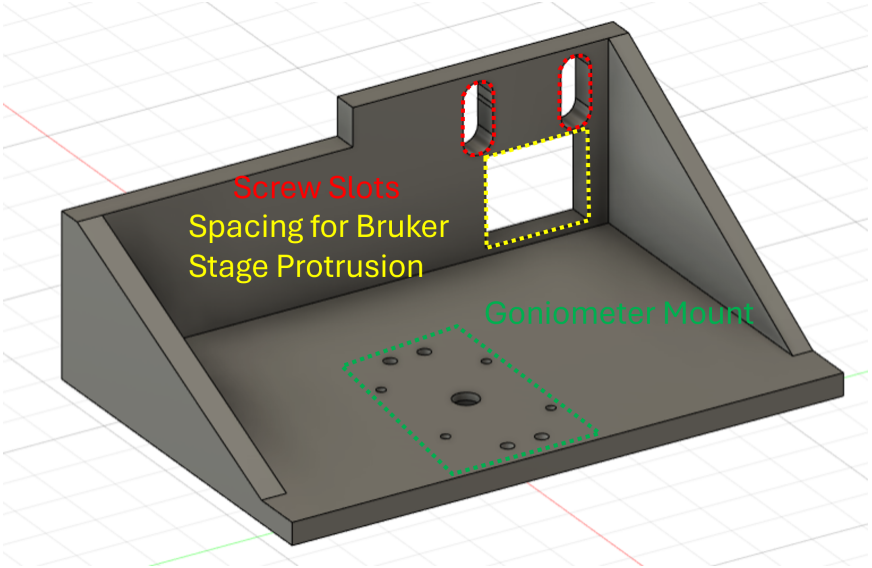


Figure 3.11: Schematic of designed stage mount with slotted screw holes and mounting holes for the goniometer.

250nm. For sample areas on the order of microns this is sufficient.

At the top of the stack, a bare printed circuit board (PCB) should be added to enable easy electrical connections to the sample. This was not implemented at the current phase of the project, but the design was completed and is shown in Figure 3.12. It should feature large gold pads that can be wire-bonded to, and they should terminate with a low-profile connector. Finally, the sample should be propped on a raised 1x1cm$^2$ block to provide additional room between the edge of the stage and the AFM head.

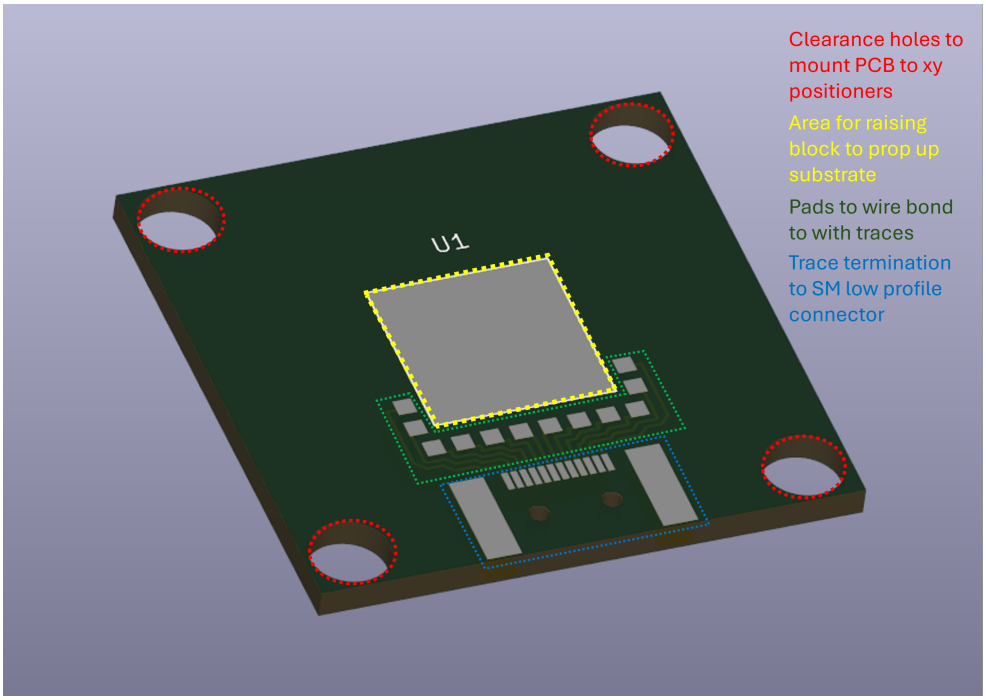


Figure 3.12: Schematic of designed bare PCB with features highlighted

## 3.4 Sample Pillar

As demonstrated in Figure 3.6, a raised sample platform reduces the likelihood of collisions during engagement of the custom tip. The following section outlines the process to fabricate an electrically contacted raised sample pillar 60-80um in height. Figure 3.13 illustrates the steps of the developed process used to define the pillar feature, which relies on photolithography, plasma etching and wet etching. The entire process can be divided into four or five main substeps, the details and development of which are described in the following subsections.

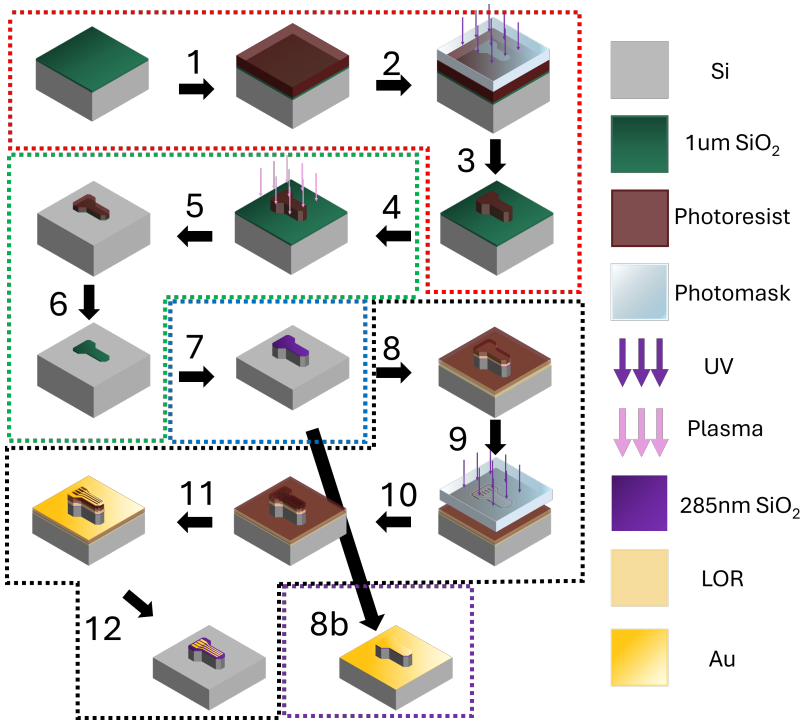


Figure 3.13: Raised sample pillar substrate fabrication process. Steps 1-3 (Red): A patterned photoresist mask is defined on a Si/$SiO_2$ substrate. Steps 4-6 (Green): A plasma etching step removes the unprotected $SiO_2$ such that patterns of unetched $SiO_2$ remain. Step 7 (Blue): A KOH wet etch is performed to etch into the Si using selectivity between the $SiO_2$ and crystal orientation. Steps 8-12 (Black): A patterned photoresist mask is defined to deposit a set of conductive contacts. Step 8b (Purple): An unpatterned conductive layer is deposited.

### 3.4.1 Substrate Selection

For the developed method, the substrate must be an intrinsic Si wafer oriented in the $\langle 100 \rangle$ plane with 1um $SiO_2$. The orientation of the crystal and the thick oxide layer are necessary to take advantage of a wet potassium hydroxide (KOH) etch. The wafer does not have to be intrinsic, but it can not be boron (B) doped as the B greatly reduces the etch rate of the Si, as was found during initial trial runs and is

well known [103].

While Si will always develop a native oxide layer (∼4-5 nm) when exposed to air, it is common for Si wafers to be purchased with a thickened layer. The amorphous oxide is generally grown with thermal oxide in which the wafers are heated in the presence of an oxygen containing source. For thicknesses 300nm and below, a dry thermal oxide is grown which is slow but yields a higher density higher quality film. For thicker films, a wet oxide is grown with water vapour and is faster, but can yield lower quality films. There was no discernible difference between the etch rates of two oxide types during the development of this process.

### 3.4.2 Plasma Etch Photoresist Mask

To begin, a patterned photoresist etch mask is defined on the substrate using photolithography. This will be used in the next step to perform a patterned etch into the wafer's oxide layer. In photolithography, a photosensitive polymer (photoresist) is exposed by an ultraviolet light (UV) light source through a patterned mask. A positive resist, as is used here, becomes soluble in developer when exposed. As a result, after development, a patterned layer of unexposed resist will remain. The process described here uses an i-line (365nm) contact photolithography setup that is manually aligned with micrometre screws. In this step, SPR220-7.0 photoresist is used due to its ability to form uniform films with micron scale thicknesses, making it an effective candidate for use as an etch mask. The pattern defined in this step, described in Appendix F, consists of large area pillar shapes with the smallest feature size being on the order of 100s of um. Broadening of the features as a result of

diffraction through the thick resist layer is not a relevant consideration. The mask is prepared with the following recipe:

- On a clean Si substrate with 1um $SiO_2$, spin SPR220 at 6000RPM
- Perform a soft bake on a 115°C hotplate for 90s
- Measure the photolithography lamp irradiance to determine the required exposure duration to achieve a dose of 385mJ
- Load the first photolithography mask (Appendix F) and expose the photoresist for the calculated dose time
- Let the substrate sit for over 30 minutes post exposure
- Perform a post exposure bake on a 115°C hotplate for 90s
- Develop the exposed areas of photoresist by placing the substrate into a beaker filled with M24 developper for 60s. To stop the development, submerge the substrate in water.

Images of an example patterned photoresist etch mask can be seen in Figure 3.14. After development, the thickness of the photoresist mask can be confirmed with a profilometer trace or with ellipsometry on an unexposed film. In the particular example, a profilometer trace over the alignment marks, shown in Figure 3.14, measures the thickness of the mask to be just under 5um. Note that there will always be some variance in the film thickness which could result from overdevelopment, the size of the wafer, etc.

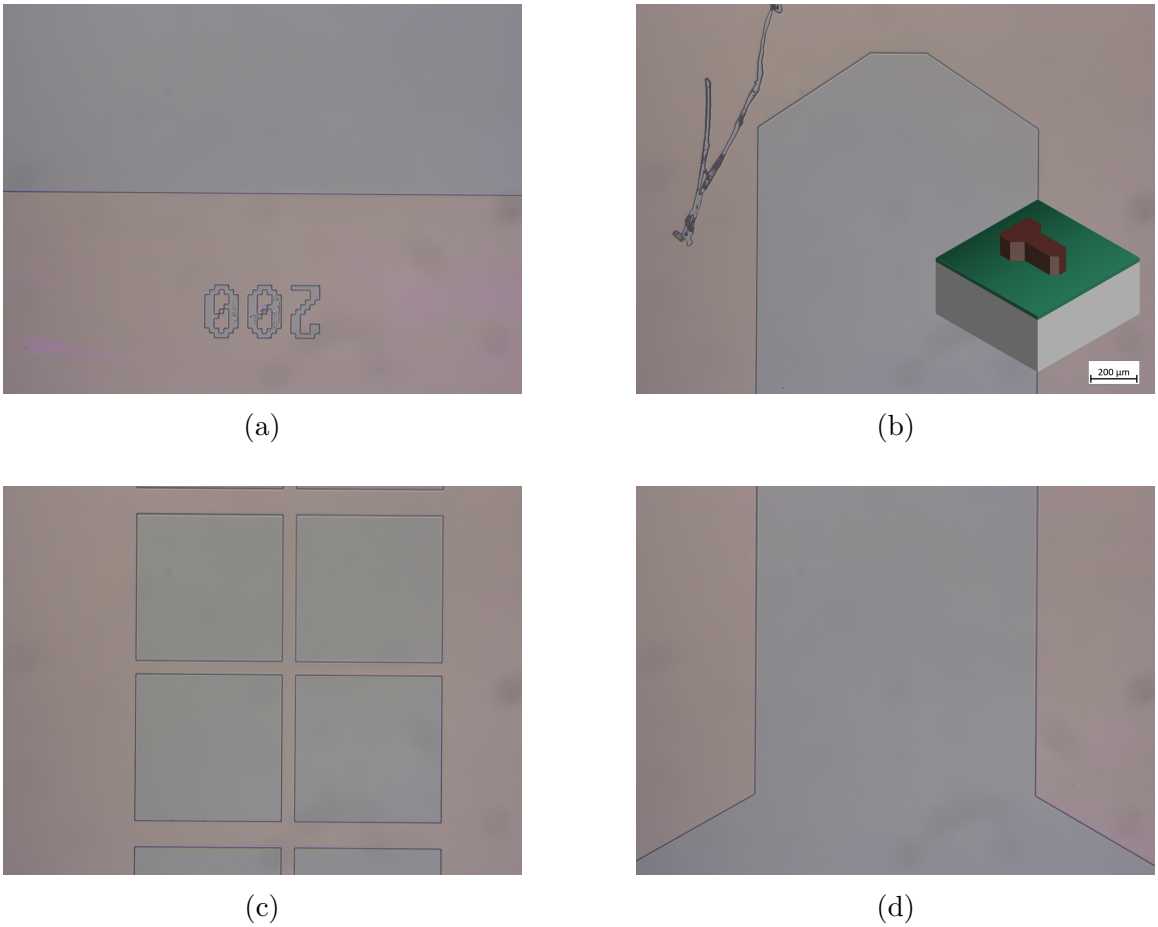


(a) (b)

(c) (d)

Figure 3.14: Patterned photoresist etch mask. Blue-gray features are photoresist. Pink-gray areas are 1um of $SiO_2$. a) Label "200" to identify feature. b) End of pillar feature. Inset: Schematic of the patterened photoresist etch mask in the shape of the pillar. c) Alignment marks. d) Middle of pillar feature.

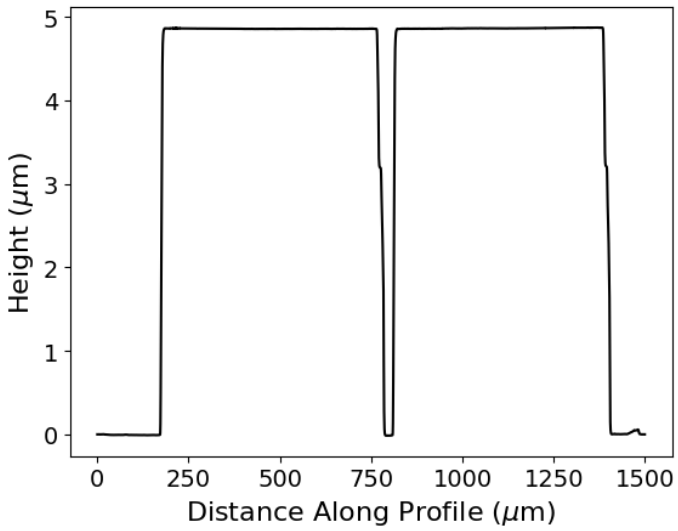


Figure 3.15: Line profile of patterned photoresist layer taken over an alignment mark, shown in Figure 3.14, taken by profilometry.

### 3.4.3 Plasma Etch

A dry plasma etching step is now performed to etch away the areas of exposed $SiO_2$ while the patterned photoresist areas will remain. The etch takes place in a reaction ion etcher (RIE) with an $Ar/CF_4$ chemistry. In this process, the Ar ions sputter etch the surface and the fluoride ions assist by reacting with the surface chemically [104]. The chamber is initially evacuated, then filled with $Ar/CF_4$ gasses at flow rates of 10/25 sccm to a pressure of 8Pa. A radio frequency power source supplies 100W to ignite the plasma, ionizing the gasses and accelerating the ions to the sample, ultimately leading to material removal.

The recipe was initially tested on unpatterned $SiO_2$ substrates and unpatterned SPR220 films for 5 minutes. The etch rates measured by ellipsometry (Appendix

I) were $\sim$ 50nm/min and $\sim$ 150nm/min respectively. Assuming the process is linear, etching 1um of oxide would take $\sim$ 20minutes and at least 3um of resist would be necessary. The measured etch rates should only be used as a guide because plasma etching processes are not linear in general and anecdotally, show variance between days. As such, monitoring the etch rate between shorter runs with profilometry and ellispometry and adapting as necessary is prudent.

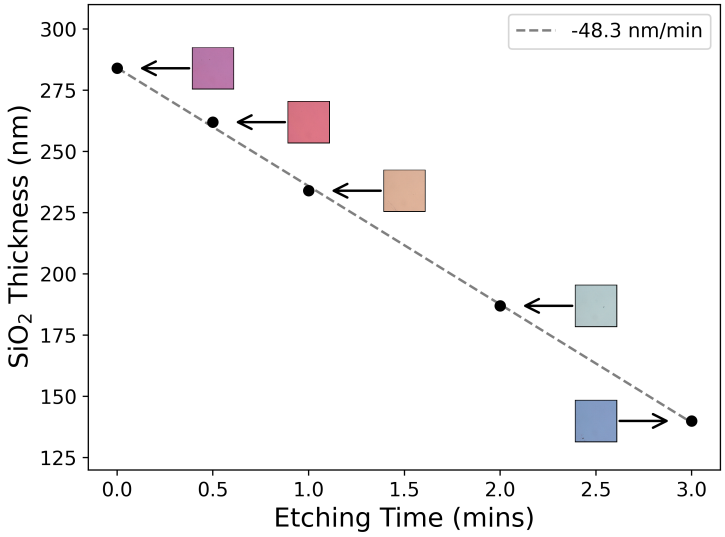


Figure 3.16: $Ar/CF_4$ plasma etch $SiO_2$ etch rate measured with ellipsometry used as a guide. Images of the substrate taken at each point show the colour change in the $SiO_2$ film as the thickness changes. A linear regression is used to calculate the etch rate.

The patterned $SiO_2$ mask achieved by plasma etching the photoresist mask shown in Figure 3.14 can be seen in Figure 3.18. Initially, a 10 minute etch was performed and the film thicknesses were measured with unpatterned witness samples and profilometry. Based on the results and the average etch rates, another 15 minutes was

deemed appropriate. While the 1um of oxide was entirely cleared near the perimeter of the substrate, approximately 90nm remained near the centre. This gradient could have resulted from non-uniformity in the plasma etching process, where etch rates were higher at the edges or from an incomplete development of the photoresist near the centre which could have caused a partial masking. In the following KOH etch step, the remaining oxide will reduce the effective mask and total etch depth. However, the resulting pillars will still be 10s of um tall so this variation does not pose any issues. The remaining resist was then removed with acetone. Profiles of the $SiO_2$ mask thickness in different locations of the substrate are shown in Figure 3.17, clearly demonstrating the gradient.

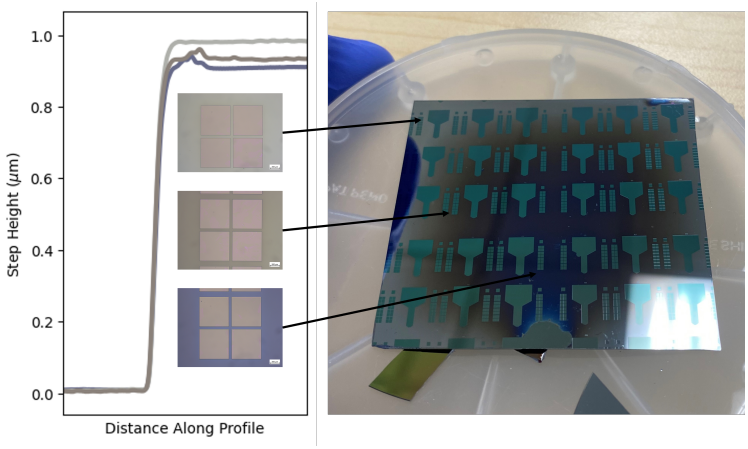


Figure 3.17: Images of patterned substrate after plasma etching displaying lack of spatial uniformity in the etch depth. Left: Profilometer traces over alignment marks taken at different locations on the plasma etched substrate. Etch mask thickness varies from approximately 900nm to 1um. Right: Image of substrate with $SiO_2$ mask.

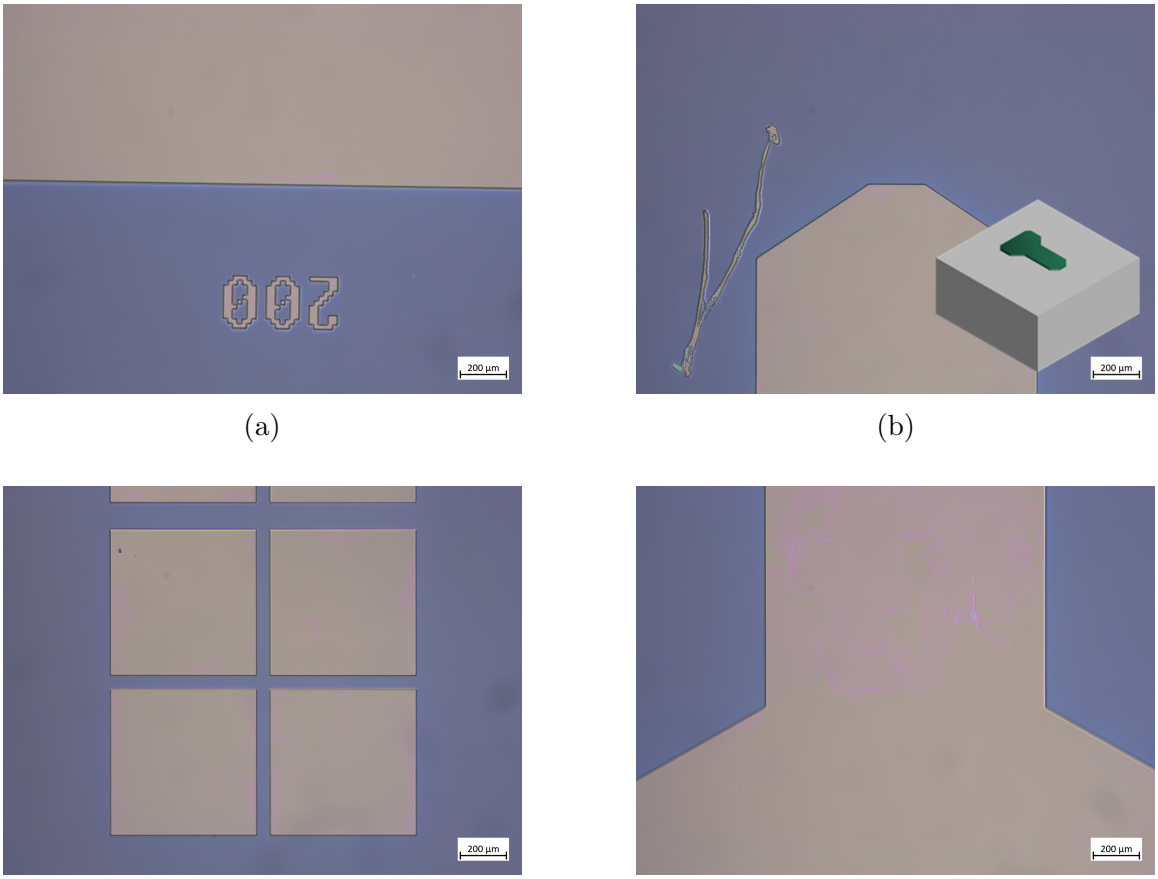


(a) (b)

(c) (d)

Figure 3.18: Patterned $SiO_2$ mask. Purple areas are remaining $SiO_2$ not etched away, here approximately 90nm. Pink-gray features are 1um of $SiO_2$. a) Label "200" to identify feature. b) End of pillar feature. Inset: Schematic of the patterned $SiO_2$ mask in the shape of the pillar. c) Alignment marks. d) Middle of pillar feature.

### 3.4.4 KOH Wet Etch

We now have an intrinsic Si substrate oriented in the $\langle 100 \rangle$ plane covered by a $\approx$ 1um thick pattern of $SiO_2$ that can be used as an etch mask for a wet KOH etch. In this process, highly vertical etching will take place in regions without a protective layer of oxide given the fast etch rate of the Si $\langle 100 \rangle$ plane and the low etch rate

of the sidewall planes [105]. Regions covered with the thick oxide etch mask will be protected given the slow etch rate of $SiO_2$. Regions with some oxide not etched during the plasma etching step will just have thinner effective masks because the Si etching can not begin before the oxide is completely removed. During that time, the 1um mask will be etched partially aswell. To maintain good optical contrast of thin 2D materials, we would like to retain approximately 285 or 90nm of oxide on the pillars [106]. This makes the effective mask thickness 1um - 285(90) nm less any native oxide or remaining oxide not etched during the plasma etching step.

The KOH etching setup underwent three variations before the final configuration was established. Initially, a hotplate was used to heat the KOH solution from the bottom of a beaker, but low contact area made for poor heat transfer. In addition, this setup had very low thermal mass making controlling the temperature exceedingly difficult. KOH etching is a temperature dependent process, so this was found to be inadequate. The next iteration used a temperature controlled water bath. This immediately improved the temperature control and stability, however it was found that after etching the $SiO_2$ was not uniform and displayed patches of different thicknesses. The final resulting setup uses a temperature controlled ultrasonic bath in which the oscillations appear to aid in the uniformity.

The recipe uses 30% KOH at 70°C with the transducer driven at 37kHz. The $SiO_2$ etch rate is approximately 325nm/hr which sets the total etching time to just over 2h. A witness unpatterned $Si/SiO_2$ substrate was used to monitor the remaining $SiO_2$ with ellipsometry. The raised sample pillar with 285nm of $SiO_2$ on top is shown in Figure 3.20. Visually, the etched Si is rough and silver, while the pillars are purple,

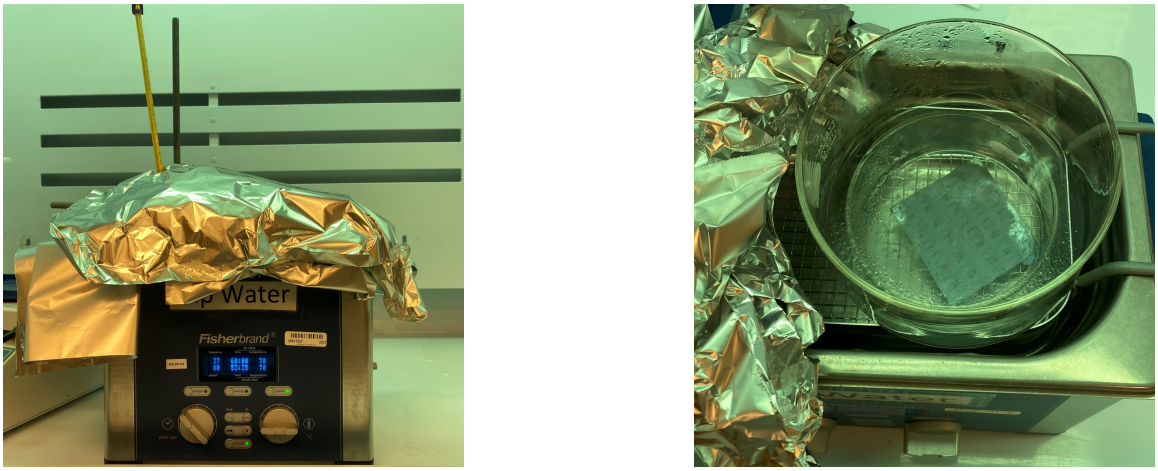


(a) (b)

Figure 3.19: Final KOH etching setup within ultrasonic temperature controlled bath. a) View of system in operation with aluminum foil used to insulate the system and an external thermometer to verify temperature readings from the system. b) View of patterned substrate being etched within KOH solution.

characteristic of 285nm $SiO_2$. A profilometer scan of the pillar feature, shown in Figure 3.22, measures the resulting pillar height to be ≈70um. The profile also reveals the angle between planes from a KOH etch. Sidewall etching is visually evident in Figure 3.20, where a reduction in the area of the alignment marks can be observed by comparing pre and post etch images.

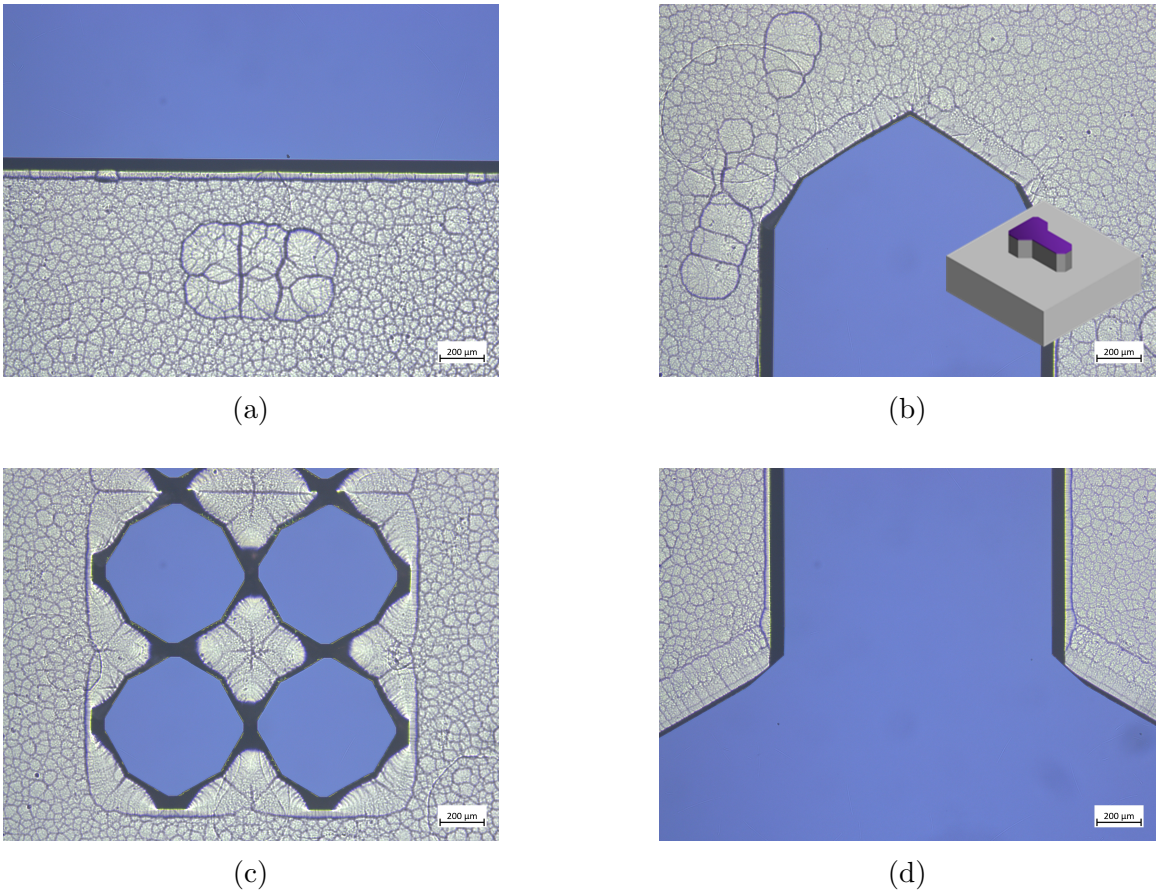

(a) (b)

(c) (d)

Figure 3.20: Etched sample pillar. Silver rough areas are etched exposed Si. Purple features are 70um pillars with 285nm of $SiO_2$ on top. a) Etched "200" label. b) End of pillar feature. Inset: Schematic of etched pillar with 285nm of $SiO_2$ on top. c) Alignment marks. d) Middle of pillar feature.

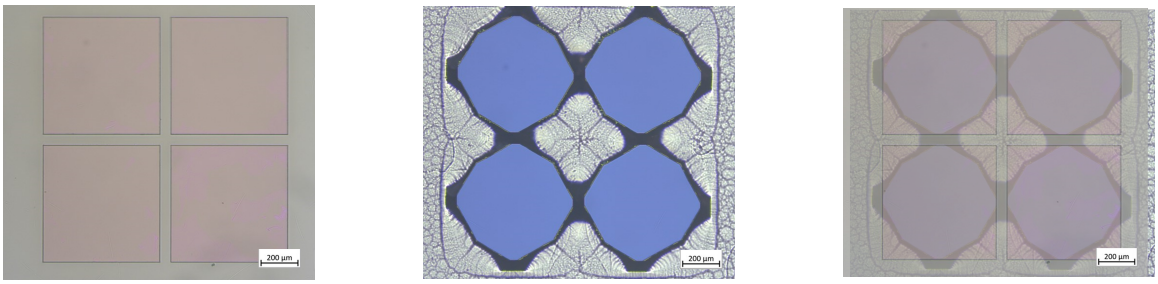

(a) (b) (c)

Figure 3.21: Alignment marks before and after KOH etching displaying sidewall etch. a) Before etch b) After etch c) Before and after overlaid

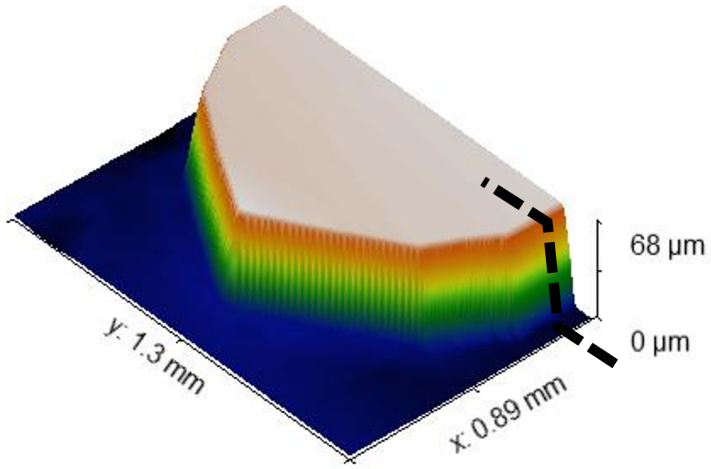


(a)

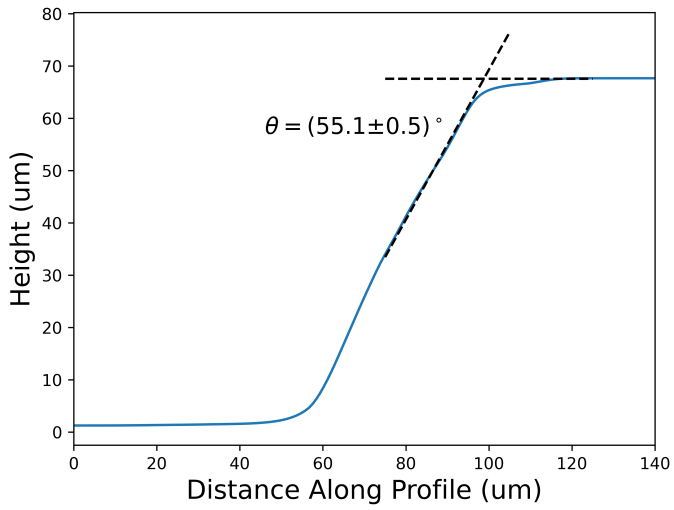


(b)

Figure 3.22: Profilometre scan of etched pillar shown in Figure 3.20. a) 3D scan of pillar edge with line cut path shown by dashed black line. b) Line cut of 3D scan displaying characteristic vertical etching angle.

### 3.4.5 Electrical Contacts

Upon completion of the patterned substrates with tall etched pillars, electrical contacts must be established. For simple samples, only one contact is needed and the entire pillar can be coated with Au at the expense of optical contrast of placed flakes. Samples that require isolated contacts require a patterned deposition. To define the contact shapes before metal deposition, a photolithography step with a lift off resist (LOR) is required. LOR, similar to photoresist, becomes soluble in developer when exposed, but is designed to develop an undercut such that evaporated films do not bridge to the sidewalls. The effect of the undercut achieved through the use of an LOR is demonstrated in Figure 3.23.

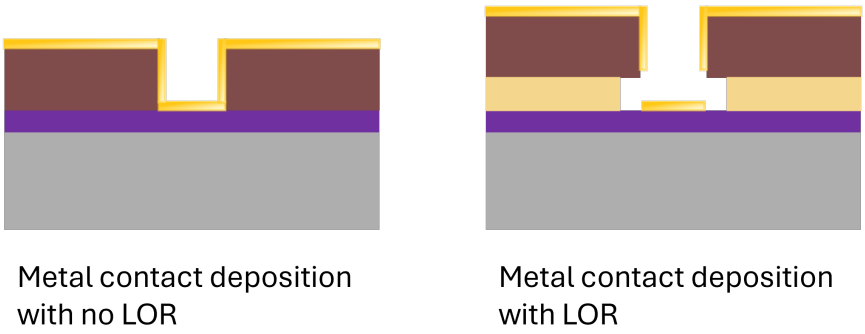


Figure 3.23: Schematic demonstrating the need for a LOR film during a patterned photolithography metal deposition

The smallest dimension on the electrical contact photomask is 15um (Appendix F). This is still quite large with respect to the diffraction limit, but there is significantly less tolerance than in the first photolithography step. Ideally, a thin resist would be used, but there are practical issues with our substrate. Initial trials to spin thinner, more appropriate resists, SPR955 and LOR2B, failed with them not adhering to the

substrate and lacking uniformity. As such, thicker resists with significantly higher viscosity, LOR10B and SPR220 once again, are required. The resulting films adhere to the substrate and are sufficiently uniform for our contact patterns, but would be challenging to use for small features. The procedure for the second photolithography step is:

- On the patterned substrate, spin LOR10B at 3000RPM
- Perform a soft bake on a 180°C hotplate for 5mins
- Spin SPR220 at 6000RPM on the LOR10B fil
- Perform a soft bake on a 115°C hotplate for 90s
- Measure the photolithography lamp irradiance to determine the required time to achieve a dose of 385mJ
- Load the second photolithography mask (Appendix F) and expose the photoresist for the calculated dose time
- Let the substrate sit for at least 1h post exposure
- Perform a post exposure bake on a 115°C hotplate for 90s
- Develop the exposed areas of photoresist by placing the substrate into a beaker filled with M24 developper for 60s. To stop the development submerge the substrate in water.

The developed contact patterns on the raised sample pillars are shown in Figure 3.24. The substrates with or without a patterned resist layer are loaded into an evaporator

chamber to deposit 3nm of Cr and 50nm of Au by e-beam and thermal evaporation respectively. The patterned substrates can then be placed in a photoresist remover or acetone to perform the lift off. The completed conductive raised sample pillars are shown in Figure 3.25.

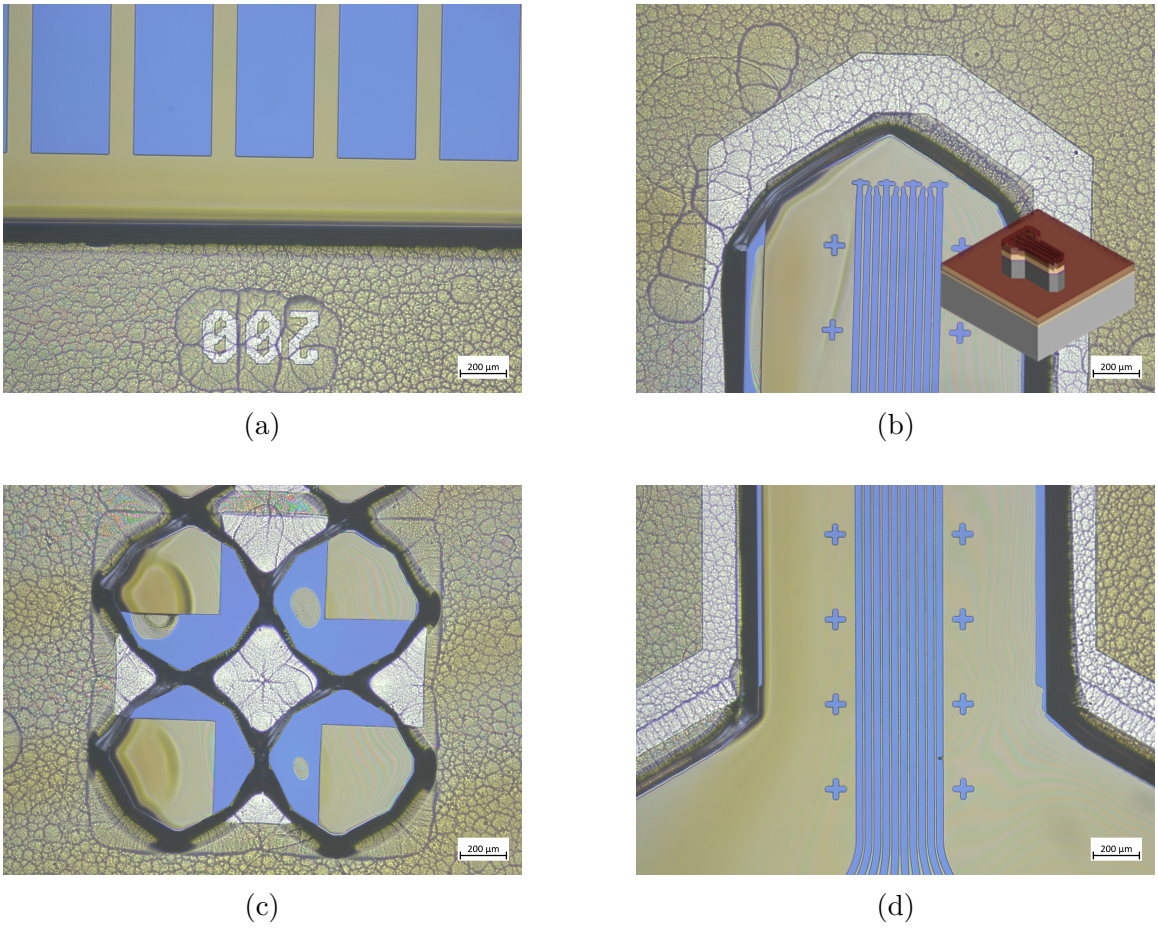


(a) (b)

(c) (d)

Figure 3.24: Etched sample pillar with a developed LOR and photoresist contact pattern. Yellow areas of resist whereas exposed and developped areas show the substrate underneath. a) Label to identify feature. b) End of pillar feature. Inset: Schematic of developed pattern on etched pillar. c) Alignment marks. d) Middle of pillar feature.

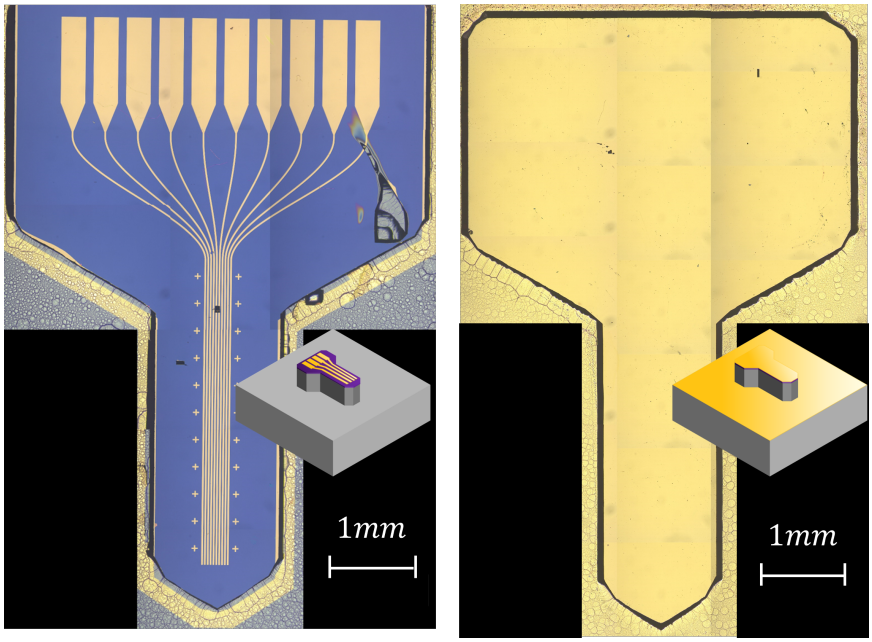


Figure 3.25: Complete raised sample pillars with different metal contact patterns. Left: Pillar with patterned Au contacts with 285nm of $SiO_2$ on top. Inset: Schematic of pillar with patterned contacts. Right: Pillar with Au coating. Inset: Schematic of pillar with Au coating.

## 3.5 Measurement Electronics

To apply a bias across the junction and measure the resulting current, appropriate electrical instrumentation is necessary. DC measurements are sufficient for initial characterization, but certain features of the $I(V_B, \theta)$ plots become more readily visible in the $\frac{dI}{V_B}$ plots which should be taken with a lock-in amplifier.

### 3.5.1 DC Measurements

To perform DC measurements, only a standard source measurement unit (SMU) is required. For this work, I decided to use a 6.5 digit Keithley 2400 SMU which I interface with through GPIB-USB adapter using a standard Python library. The voltage source is swept over a range and the current at each voltage step is recorded.

### 3.5.2 Lock-in Measurements

A numerical derivative of collected DC IV curves can be taken, but present noise will dramatically affect the signal. Therefore, it is customary to take dI/dV measurements by approximating $\frac{dI}{dV} \approx \frac{I_{AC}}{V_{AC}}$ where the AC voltage is kept small.

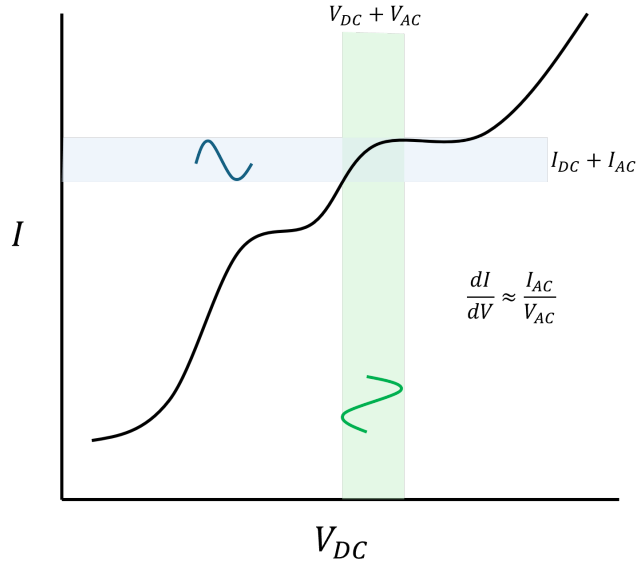


Figure 3.26: Demonstration of the use of an AC bias superimposed on a DC value to estimate $dI/dV$.

In a noisy environment, collecting the AC signal without any filtering will not yield

any improvement over the numerical derivative. Instead, a lock-in amplifier is used to apply the small AC bias at a reference frequency $\omega_r$ and collect the filtered response signal at the same frequency, functionally acting as a very narrow bandpass filter. I implemented a lockin amplifier using a National Instruments (NI) multipurpose board with digital to analog converters (DAC) and analog to digital converters (ADC).

The DAC generates the DC signal, $V_B$, superimposed with the reference AC signal at $\omega_r$ to be applied across device under test (DUT). The ADC then digitizes the response signal of the DUT, now containing noise. The noisy digitized signal is then mixed with the reference signal in Python. The signals are then lowpass filtered to extract the amplitude of the signal at the reference frequency. The two out of phase signals are added in quadrature to extract the relevant signal amplitude. We now have everything we need to get the amplitude and phase of the signal at the reference frequency. Normally, the signal across the DUT can be sampled without issue. However, for this system, connecting the leads across just the junction would be very challenging. Instead, a transimpedance amplifier can be used to measure the current as a voltage signal which can then be read by the ADC. Details on the underlying math behind the filtering and a test of the homemade lockin amplifier system can be found in Appendix G.

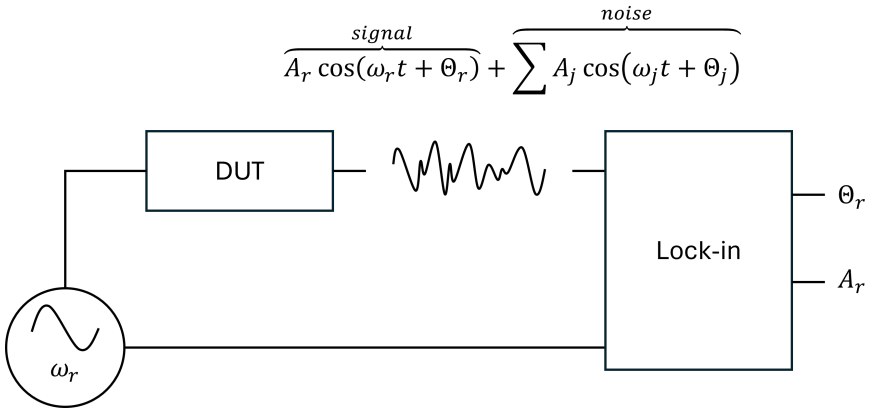


Figure 3.27: Lock-in amplifier functionality. Reference signal generated at $\omega_r$ to the DUT. The signal across the DUT is sampled, now containing the signal of interest at $\omega_r$ and noise at other frequencies. Lockin amplifier extracts the relative phase between the reference and signal of interest as well as the amplitude.

## 3.6 Transfer Techniques

The commonly used methods to transfer flakes and vdW stacks to substrates require modifications to deterministically transfer flakes to our custom pillar and tip structures. Within our group and the field in general, the exfoliation and stacking of individual vdW materials or heterostructures onto a polymer film is routine. Readers unfamiliar with these standard techniques are directed to Appendix A. Briefly, the fabrication process results in a flake or vdW heterostructure on a polymer film, polypropylene carbonate (PPC) is used in our group, that must be transferred to a substrate.

As demonstrated in Appendix A.6, materials transferred to a substrate by the inverted transfer technique can drift from their original location. To create our interfaces, half of the 2D material interface must be placed on the etched sample pillar and the other

half is required to be placed on the custom AFM tips. The portion on the pillar must be near the edge and be aligned with the metal contacts when using the patterned contacts. Similarly, the portion on our custom AFM tips also must be on the tip and can not drift away. Unlike the inverted transfer method, by transferring the vdW structure with the polymer on top, direct contact with the substrate can be made, and the polymer can be removed with solvent without causing the flake to drift. Although not as commonly used today, this approach was used in early vdW heterostructure fabrication [22], and is the method suggested in [7, 15].

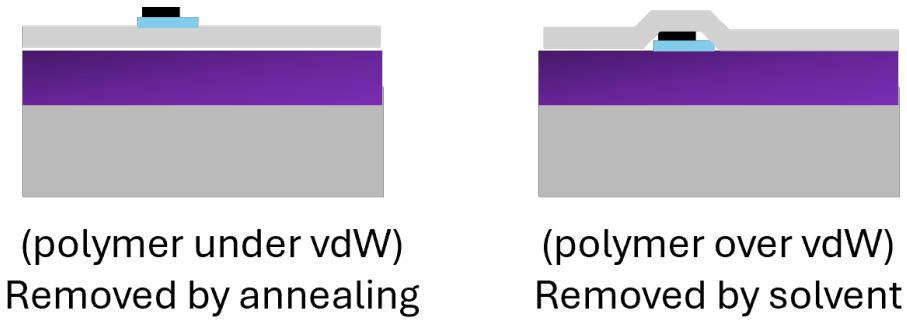


Figure 3.28: vdW transfer to a substrate with the polymer both above and below the vdW structure.

During standard fabrication of vdW heterostructures, layers are sequentially picked up onto a polymer film from bottom to top. To place the vdW heterostructure onto the substrate polymer side up as as shown Figure 3.28, the structure is flipped upsidedown as shown in Figure 3.29. Transferring individual vdW flakes from a PPC film does not have this issue, and individual layers can also be transferred successively to create a vdW heterostructure. However, to transfer a prefabricated vdW heterostructure on a PPC film, an intermediate step described in Section 3.6.1 must first be taken. The method to transfer a vdW flake or heterostructure from a polymer film to a pillar or

AFM tip is then demonstrated in Section 3.6.2.

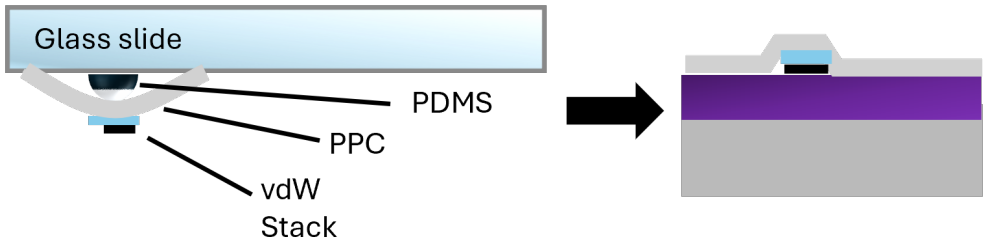


Figure 3.29: Schematic demonstrating the transfer of a pre-stacked vdW structure, that has not been flipped right side up, to a substrate polymer side up. Left: Prepared vdW heterostructure on a polymer film picked up from bottom to top. Right: vdW heterostructure transferred with polymer film above the stack, as described in Section 3.6.2, resulting in the heterostructure being upside down.

### 3.6.1 Intermediate Polymer Transfer

One approach to addressing the issue of prefabricated vdW heterostructures being flipped upside down upon transfer to the substrate is to incorporate an intermediate flipping step using a different polymer. This allows the stack to be right side up when it is ultimately placed on the substrate/structure, as shown in Figure 3.30.

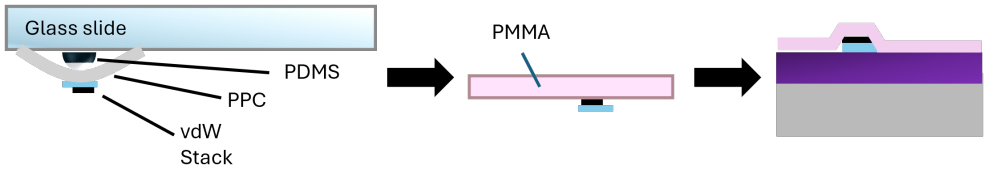


Figure 3.30: Schematic demonstrating the transfer of a pre-stacked vdW structure, that has been flipped, to a substrate polymer side up. Left: Prepared vdW heterostructure on a polymer film picked up from bottom to top. Middle: Intermediate step to flip vdW stack by transferring it to a different polymer. Right: vdW heterostructure transferred with polymer film above the stack, as described in Section 3.6.2, resulting in the heterostructure being upside down.

The conditions on the intermediate polymer are that it must have a different glass transition temperature ($T_g$) than that of the PPC, such that it can become more adhesive than PPC when heated, but its $T_g$ can not be so high that it melts or deforms the PPC layer during transfer. To perform the transfer to the other polymer, the structure on a PPC/PDMS stamp is brought into contact with the intermediate polymer at its $T_g$, where it becomes more adhesive than the PPC, allowing the stack to transfer onto the intermediate polymer.

Polymethyl methacrylate (PMMA) has a $T_g$ around 80°C, well above that of PPC, around 40°C, and below its melting point while also being soluble in acetone. However, PMMA films are significantly more fragile than PPC and are challenging to peel off of a substrate using a tape frame. Various attempts to spin coat PMMA directly on PDMS or drop cast PMMA onto a glass slide did not yield consistently usable films. The PMMA would require a supporting film such as polyvinyl alcohol (PVA) [15, 22, 107]. The PVA has a higher melting point than PMMA and can be separated from the PVA carefully with tweezers or removed in a water bath as it is water soluble. Once the structures have been transferred to the PMMA film right side up, they can be transferred to a substrate, in the same way as a PPC film, as described in Section 3.6.2. The procedure to prepare a PVA/PMMA film and perform the transfer of a vdW heterostructure from PPC is depicted in Figures 3.31 and 3.32 and is described below:

- Prepare a flake or vdW heterostructure on a PPC/PDMS (hemispherical) glass slide. See Appendix B for the justification of a hemispherical PDMS stamp.
- Spin PVA (Partall Film 10) onto a clean substrate at 3000 RPM then place on

a hotplate at 75°C for 5 minutes

- Spin PMMA (950K A6) on the PVA coated substate at 3000 RPM then place on a hotplate at 75°C for 5 minutes
- Place PMMA/PVA substrate onto the bottom set of stages on transfer setup and PPC/PDMS glass slide stamp onto the top set of stages
- Load PPC/PDMS (hemispherical) glass slide with vdW stack onto piezoelectric stage
- Bring the flake on PPC/PDMS into contact with a clean area of PMMA at 80°C until the flake makes contact
- Slowly raise the PPC/PDMS glass slide until no longer in contact. If successful, the stack will have transferred to the PMMA.
- Pickup the PMMA/PVA film with a tape frame
- Place tape frame into a room temperature DI water bath for 10 minutes to dissolve the PVA.
- Place the tape frame onto a holed glass slide flake side down to be transferred. The glass slide should then be placed onto a 120°C hotplate to evaporate any remaining water. Any wrinkles present in the film will also be smoothed out in the process.
- Transfer the vdW heterostructure to the pillar or tip as described in Section 3.6.2.

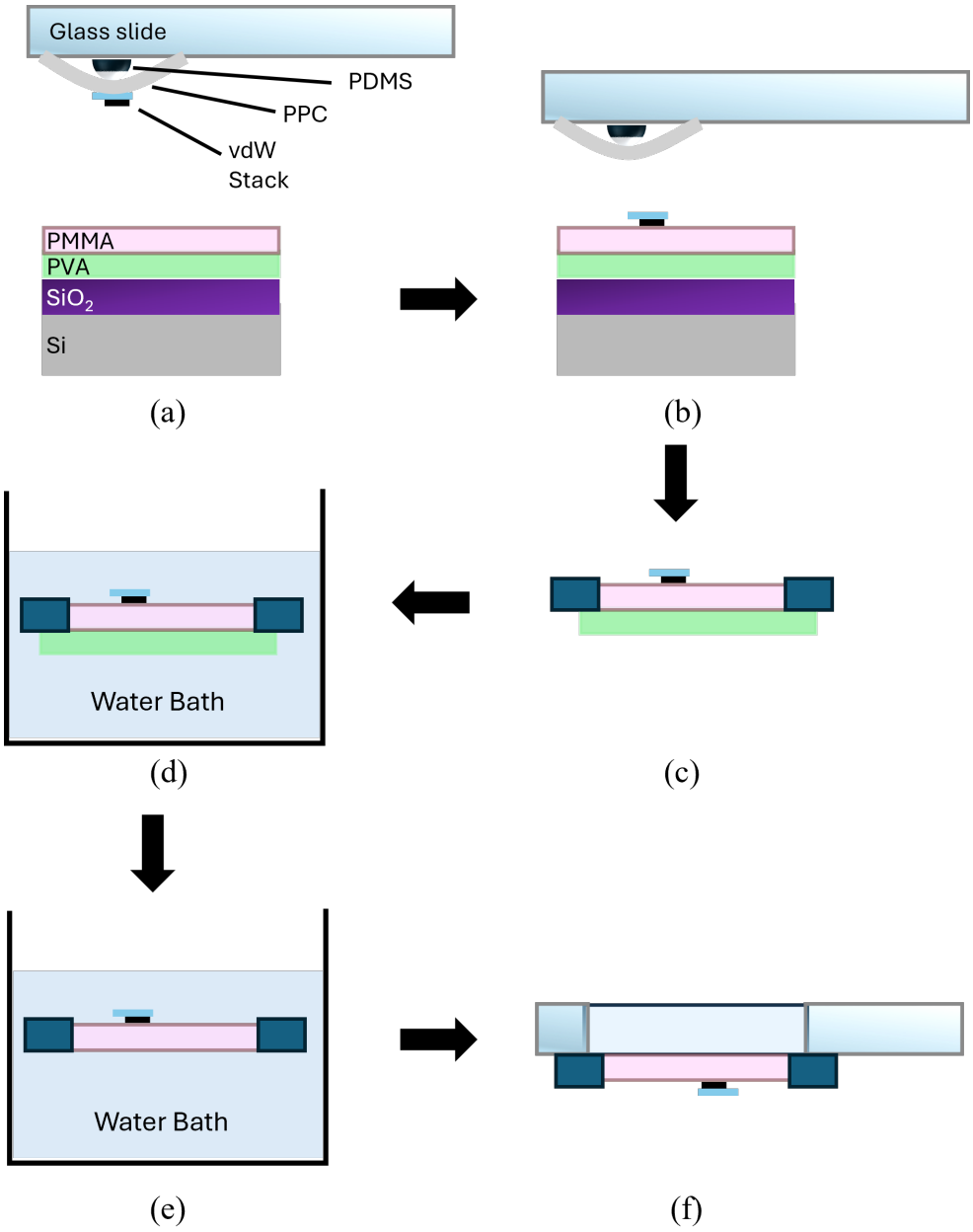


Figure 3.31: Schematic demonstrating the steps to transfer and flip a vdW structure from PPC to a PMMA tape frame. a) Beginning with a prepared vdW heterostructure on a PPC/PDMS stamp and a PMMA/PVA film on a $Si/SiO_2$ substrate. b) The stamp is brought into contact with the substrate at the $T_g$ of PMMA, 80°C, allowing the stack to adhere more strongly to the PMMA and transfer onto it. c) A tape frame is then used to lift the PMMA/PVA film. d) Tape frame is then placed in a water bath. e) The water soluble PVA is dissolved. f) The flipped vdW heterostructure on the PMMA film is mounted onto a holed glass slide, ready for its final transfer to a structure. The process is shown in Figure 3.32.

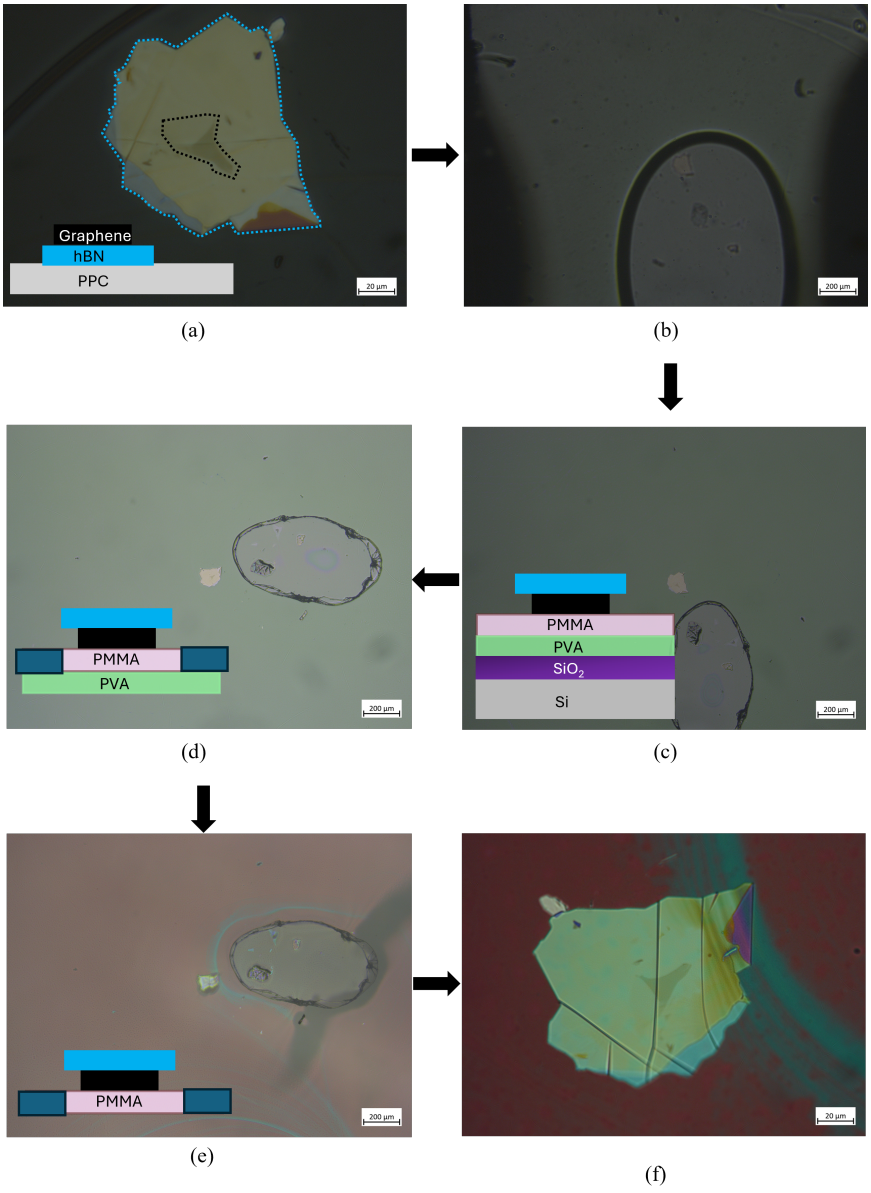


Figure 3.32: Images of the steps to flip a vdW heterostructure from a PPC film to a PMMA/PVA film. a) Starting with an hBN/graphite heterostructure on a PPC film. b) The stamp is brought into contact with a PMMA/PVA film on a $Si/SiO_2$ substrate at 80°C. The contact area of the PPC/PDMS is apparent by the circular fringe. c) When removed, the heterostructure is transferred. Some of the PPC that adhered to the PMMA is seen below the vdW heterostructure. d) The PMMA/PVA tape frame is removed from the substrate. e) A water bath is used to remove the PVA. f) A zoomed in image of the now flipped vdW heterostructure on a PMMA tape frame.

### 3.6.2 Flake Transfer

Once a vdW flake is prepared on PPC or a vdW heterostructure is rightside up on PMMA, it can be transferred to a tip or pillar structure. The target structure will be mounted on a set of positioners, while the polymer film placed on a glass will be mounted on a separate set of positioners, all under an optical microscope. The positioners will be used to align the vdW materials with the target structure and the polymer film will be melted off. To facilitate this process, it is helpful for the film surrounding the flake to be suspended such that the polymer does not adhere to the glass slide. The easiest way to think of doing this was to suspend the polymer over a 1/4″ hole in a glass slide, as shown in Figure 3.33.

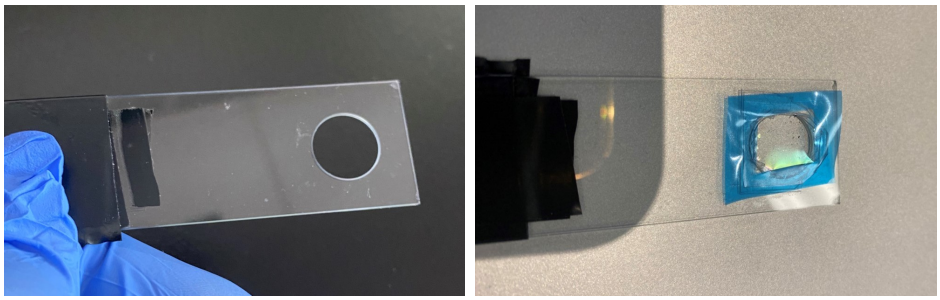

(a) (b)

Figure 3.33: Polymer tape frame suspended over glass slide with a hole. a) Glass slide with hole, b) PPC tape frame suspended over hole.

The transfer procedure is shown in Figures 3.35 and 3.36 with real demonstrations transferring individual flakes from a PPC film provided in Figures 3.37 and 3.38. Demonstrations transferring stacks that have been flipped to PMMA first are shown in Appendix J. While the pillar substrates are somewhat fragile, they can be handled as normal substrates with a bit of care. However, the AFM probes are significantly

more fragile and must be treated uniquely. In addition, since the tips are not flat, the flakes in contact do not naturally conform. Once the flake has made contact with the tip, its sides needs to be pulled down to the cantilever. This can be achieved by propping the AFM probe up, as shown in Figure 3.34. The structure propping the AFM probe up is placed on a glass slide such that when the polymer tape frame is melted off the hole glass slide, it does not stick to the transfer setup.

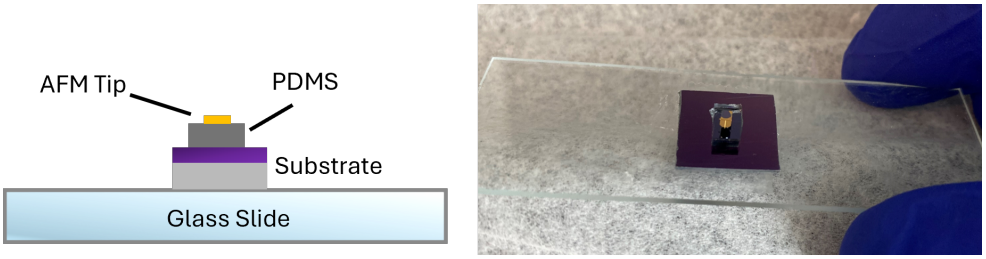


Figure 3.34: Structure used to prop up AFM tips before transfer. The structure is a substrate and a thick PDMS space all placed on a glass slide. Left: Schematic, Right: Image of structure.

The protocol is described in detail below:

- Prepare or identify a flake or vdW stack on a polymer film with a tape frame
  - A flake or stack can be picked up with standard PDMS/PPC stamp from exfoliated flakes
    - If a stack is picked up, it must first be flipped to a PMMA film as described in Section 3.6.1.
  - A flake can be exfoliated directly onto a PPC coated substrate and identified
- Place the tape frame flake side down onto a holed glass slide. If the polymer

is wrinkly, the glass slide can be placed onto a hotplate to smoothen the film. The tape frame is then placed on the piezoelectric manipulators on the transfer stage

- Place the pillar substrate or the AFM probe, propped up as is shown in Figure 3.34, on the stepper motor stage of the transfer setup
- Align the flake to the region of interest
- Lower the polymer film until it makes contact with the substrate or probe
- Raise the temperature of the stage to 140° C to melt the polymer
- Remove excess polymer around the flake by carefully cutting the tape frame away with a sharp needle
- Place the substrate or probe in an acetone bath followed by an isopropyl alcohol bath to dissolve the polymer above the flake. My setup for performing the polymer removal on the AFM probe is described in Appendix H.

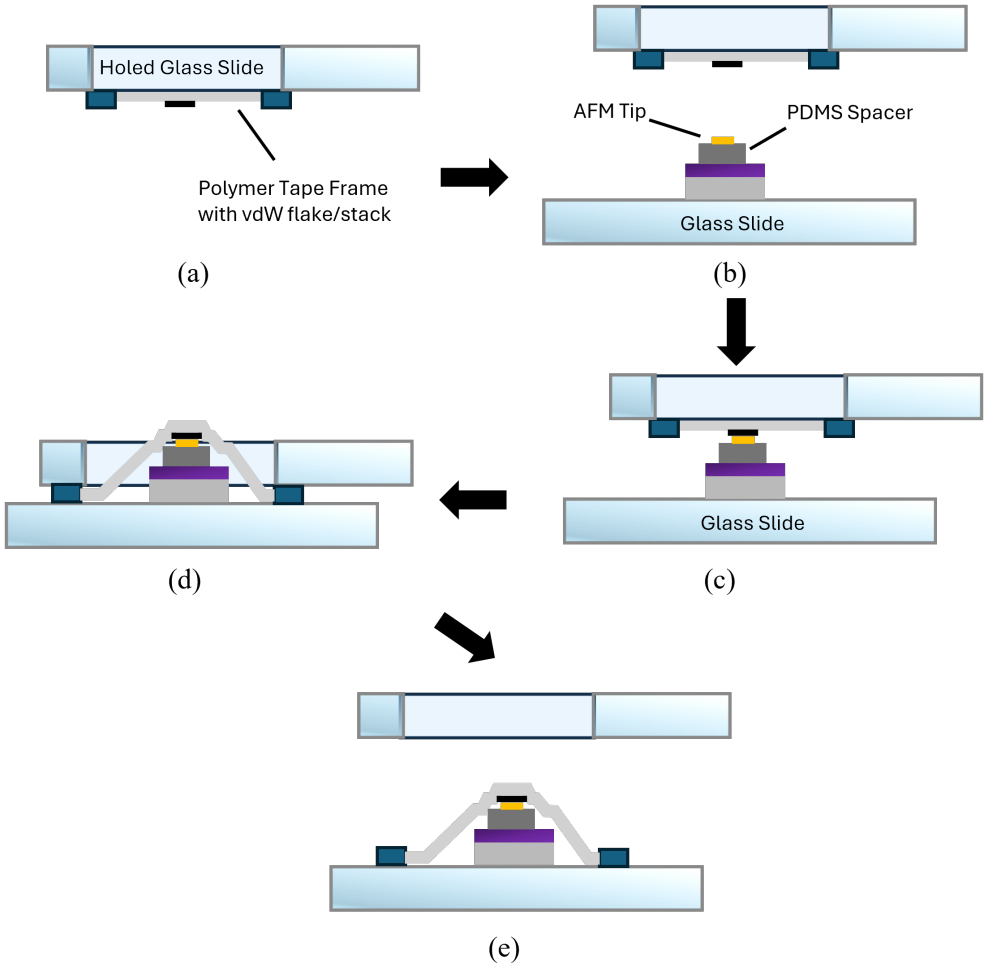


Figure 3.35: Schematic demonstrating the steps to place a vdW structure from a polymer tape frame to an AFM tip. a) Starting with a vdW flake on a polymer tape frame placed on a holed glass slide. b) The flake is aligned to the AFM tip, propped up by a substrate and PDMS spacer as shown in Figure 3.34. c) The polymer and flake are brought into contact with the AFM tip. d) The polymer is then melted off the holed glass slide so that the vdW flake conforms to the tip. e) The holed glass slide is removed such that the AFM tip can be placed into a solvent bath. The process is shown in Figure 3.37.

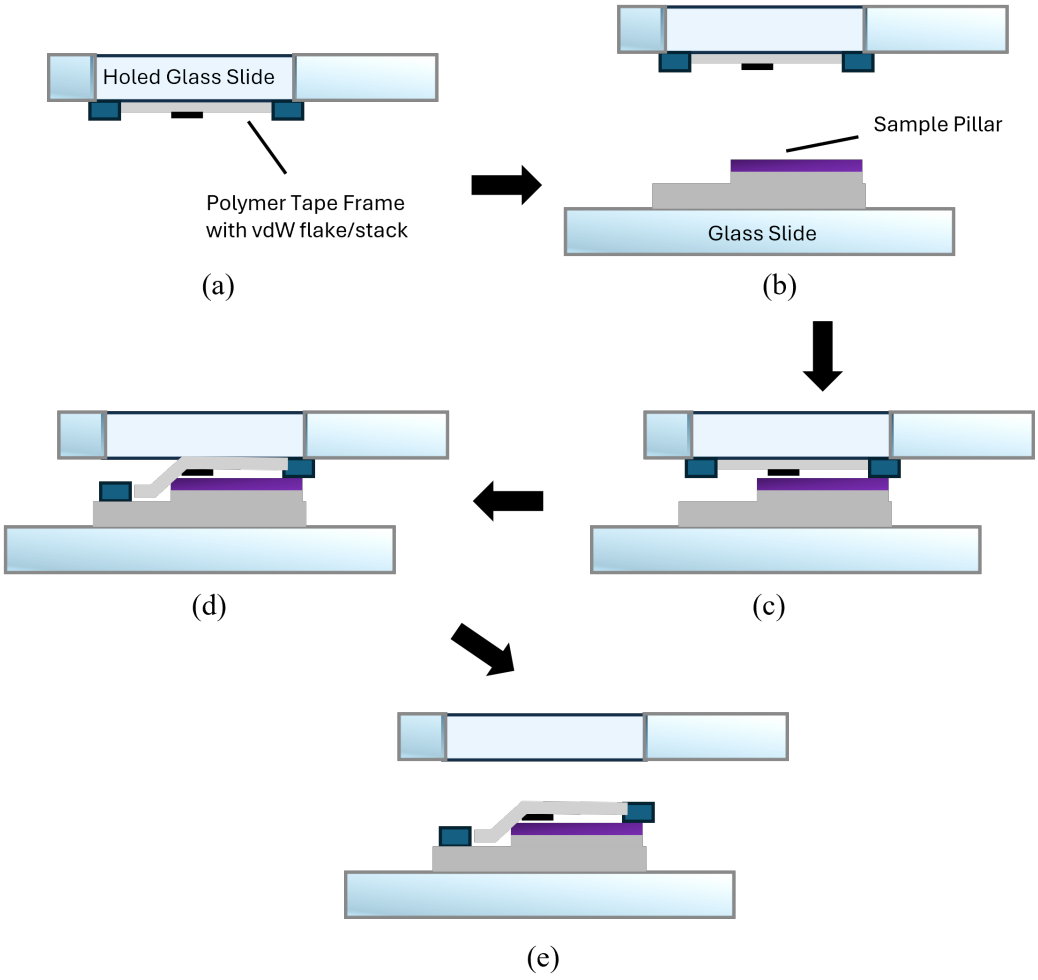


Figure 3.36: Schematic demonstrating the steps to place a vdW structure from a polymer tape frame to a raised sample pillar. a) Starting with a vdw flake on a polymer tape frame placed on a holed glass slide. b) The flake is aligned to the sample pillar substrate. c) The polymer and flake are brought into contact with the pillar. d) The polymer is then melted off the holed glass slide. e) The holed glass slide is removed such that the pillar substrate can be placed into a solvent bath. The process is shown in Figure 3.38.

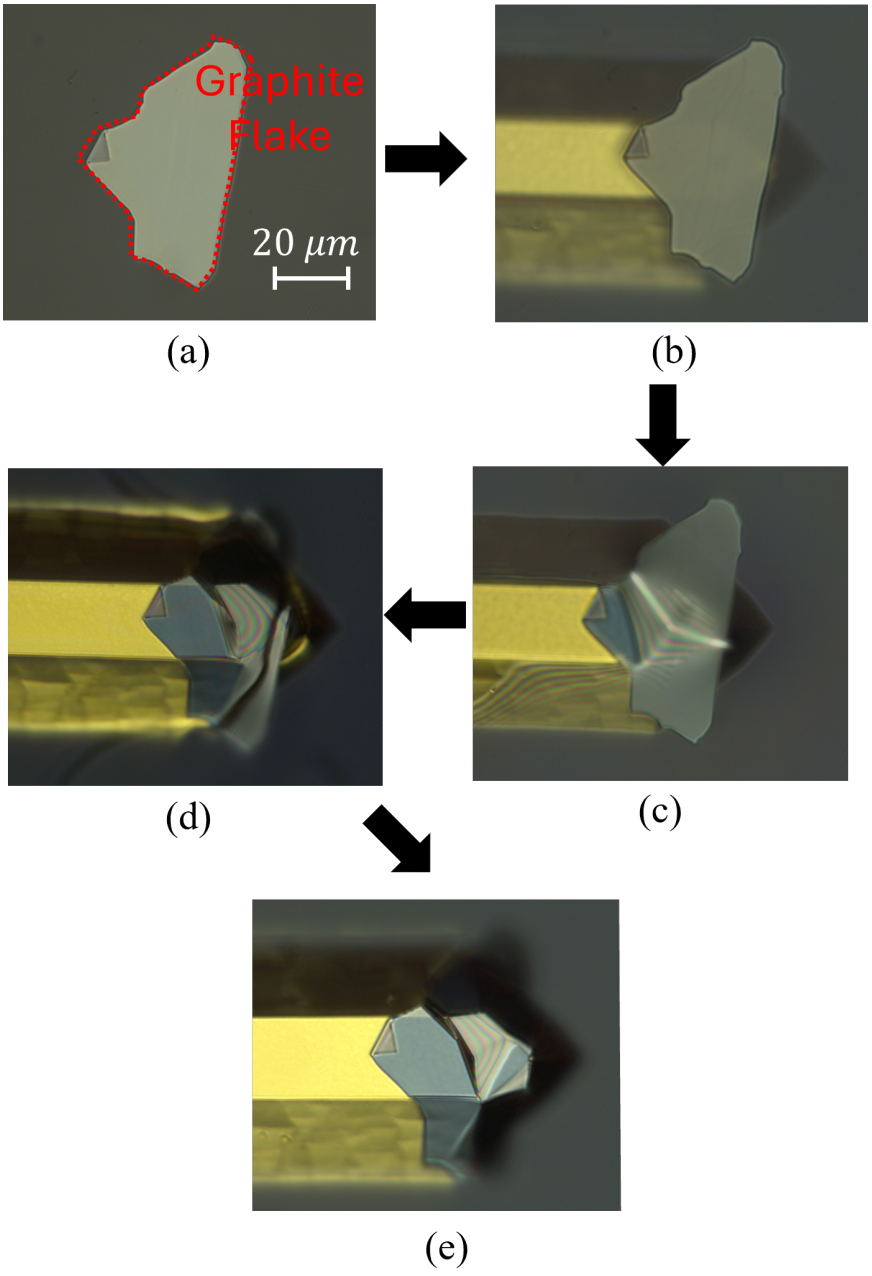


Figure 3.37: Images of the steps to place a graphite flake from a PPC tape frame to a custom AFM tip. a) Starting with a graphite flake on a polymer tape frame placed on a holed glass slide. b) The flake is aligned to the AFM tip. c) The flake is brought into contact with the AFM tip. d) The PPC is melted such the flake and polymer conform to the AFM tip. e) The AFM tip is placed into an acetone solvent bath to remove the PPC. The process is shown in Figure 3.35.

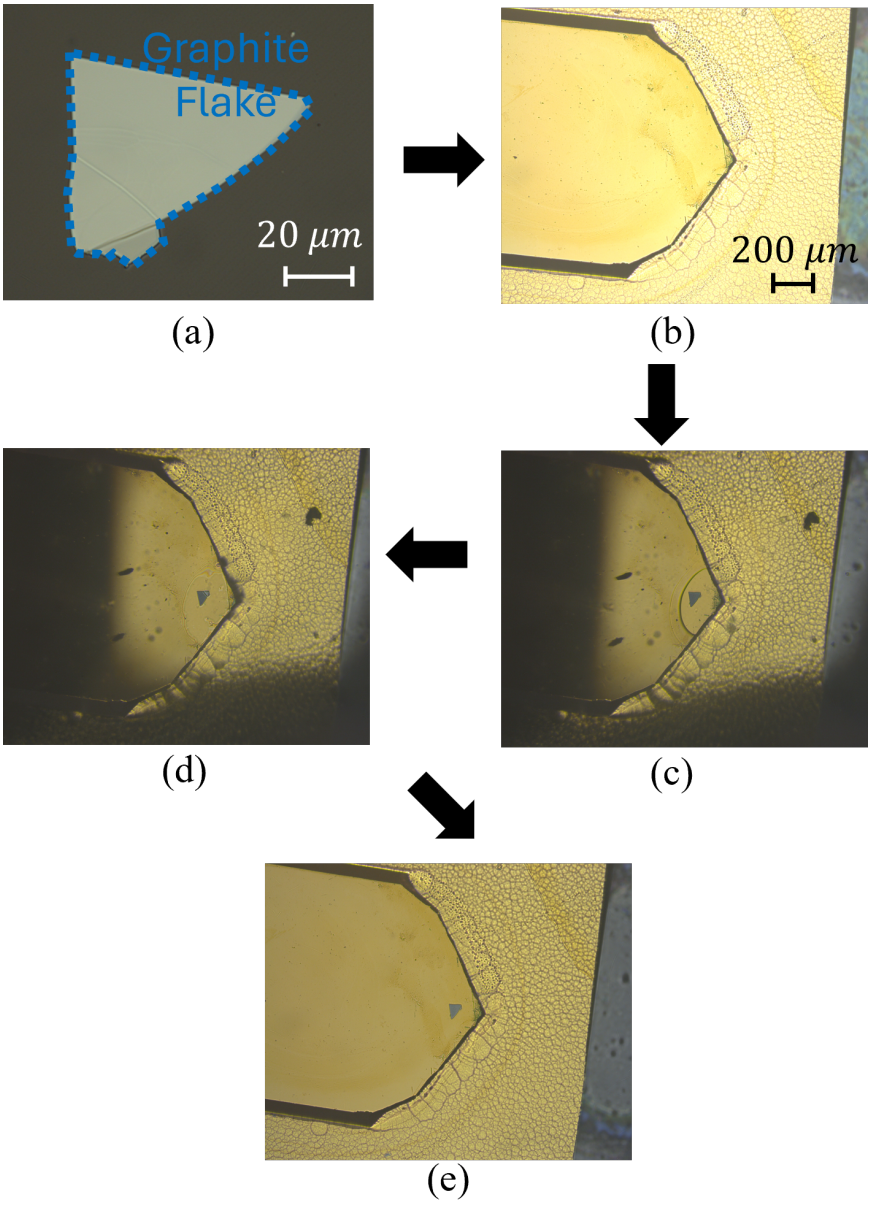


Figure 3.38: Images of the steps to place a graphite flake from a PPC tape frame to raised sample pillar. a) Starting with a graphite flake on a polymer tape frame placed on a holed glass slide. b) The Au coated sample pillar is placed onto the transfer stage. c) The flake is aligned and brought into contact with the pillar. d) The PPC is melted. e) The pillar substrate with the flake is placed into an acetone bath to remove the PPC. The process is shown in Figure 3.36.

# Chapter 4

# Electrical Transport of Vertical Graphite Interfaces

In this section, we present results obtained during prototyping of our adapted AFM system. The primary objective was to demonstrate proof of concept before more comprehensive measurements were taken. The measurements were performed using a graphite flake vdW AFM tip and a gold coated raised sample pillar with another graphite flake. All interfaces were made at fixed angles and no twisting was performed. The vertical deflection setpoint and PID coefficients used to engage the tip to the surface were fixed to low values throughout. In addition, our homemade lockin amplifier was not used as DC conductance measurements offer a simpler starting point. We begin by outlining practical considerations including the electrical connections and the conditions for successful proof of concept. Then a brief description of the procedure is provided, followed by presentation and discussion of the data.

## 4.1 Setup

The measurements are DC conductance measurements between a graphite flake placed on a custom AFM tip and another graphite flake placed on a gold coated sample pillar, both tens of nanometers thick, at a fixed twist angle. The graphite vdW tip is loaded into a standard conductive AFM probe holder which has conductive wire that contacts the surface of the Au cantilever, shown in Figure 4.1.

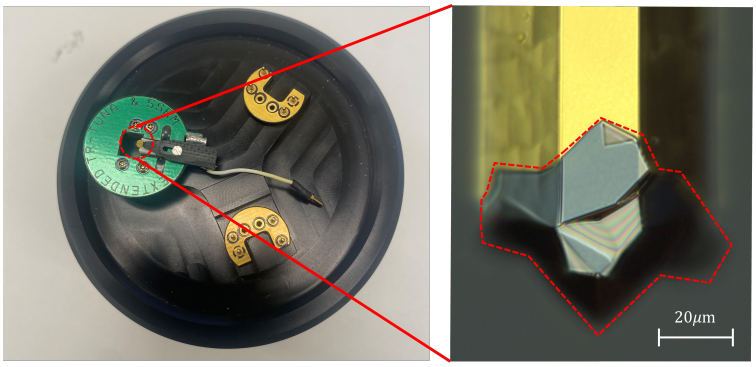


Figure 4.1: Images of the custom graphite vdW AFM tip as well as how it is electrically contacted. Left: The custom AFM tip is shown loaded onto conductive AFM probe holder with a conductive wire with white insulation. Right: Zoomed in image of custom AFM tip loaded into probe holder on left. Graphite flake highlighted by red dashed line.

The graphite flake on the Au coated pillar is shown in Figures 4.2 and 4.3. It is electrically connected by attaching a metal wire to the pillar with conductive H21D Epotek Ag epoxy. The sample substrate is placed on top of the custom stage with the goniometer incline set to approximately 11°. 3D printed spacer plates were used in place of xy positioners. A metal nut was used as a spacer to prop the sample up to limit contact between the edges of the stack and the AFM head.

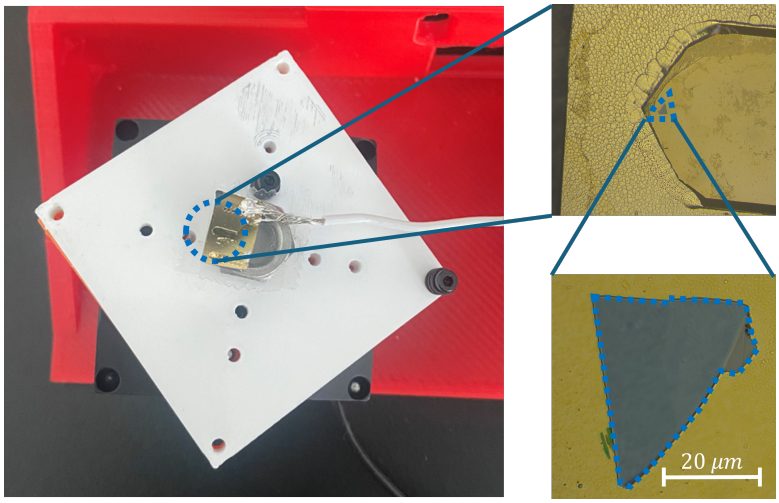


Figure 4.2: Images of the graphite flake sample pillar substrate as well as how it is electrically contacted. Left: Au coated sample pillar substrate shown mounted onto custom stage. A wire with white insulation is bonded to the Au coated substrate with Ag epoxy. Top Right: Image of the Au coated raised sample pillar with the graphite flake at the end. Bottom Right: Zoomed in image of the graphite flake at the edge of the pillar.

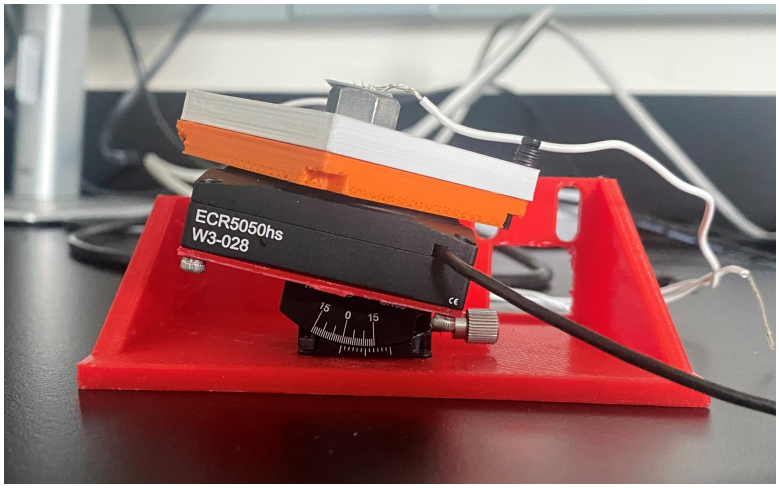


Figure 4.3: Image of custom stage with electrically contacted sample pillar. The components of which are described in Section 3.3. The components from bottom to top are as follows: mount to coarse alignment stage of adapted AFM, goniometer set to approximately 11°, ECR5050hs rotator, two spacer plates used instead of xy positioners, a metal nut, Au coated sample pillar substrate with wire used to electrically contact graphite sample.

The setup of all components is shown in Figure 4.4. A Keithley SMU is connected to the two wires contacting the two separate graphite flakes with generic spring mini-grabber clips, and is used to both source the voltage and sense the drawn current. This type of connector and wire is more prone to external noise through capacitive coupling, but made for quick and easy troubleshooting which was more important during prototyping. In the future, shielded connectors would be preferable and more permanent connections, enabled by a PCB, would make the contacts less prone to any motion. The voltage source was floated to maintain simplicity in connections and as such there is no reference to earth ground. During the measurement setup, the voltage was applied manually, starting with a deliberately low current limit that was expected to be reached. The limit was then gradually increased until the recorded current remained below it. This process ensured that no short circuits were present and helped establish an appropriate current limit that would not clip the signal. The voltage could then be swept over a -15 to 15 mV range. At each voltage step, five current readings are averaged, with the standard deviation being used as the measurement error. The resistance and uncertainty in the resistance are calculated from a linear regression and the resulting standard error in the regression.

The effective circuit we are aiming to prove that we can achieve with our system is drawn in Figure 4.5. The output impedance of the SMU is negligible, and the resistances of the wires to the graphite flakes are on the order of a few ohms. They are added as the series resistor and are not removed from the resistance measurement because they are small and the measurements remain qualitatively the same with or without their inclusion.

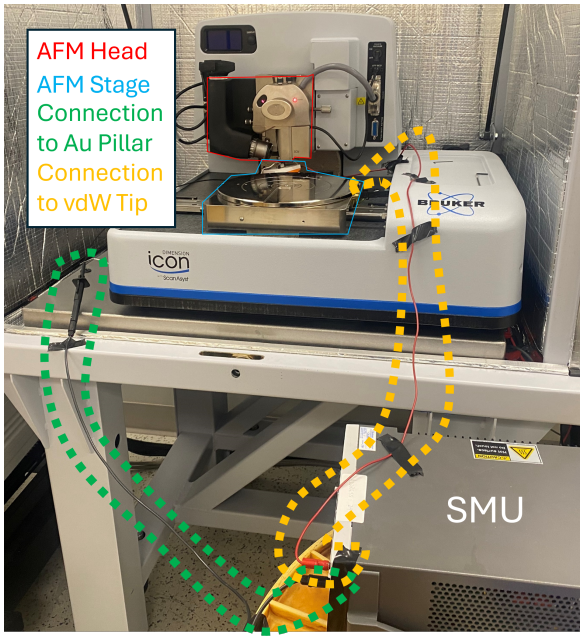


Figure 4.4: Image of the experimental setup and connections to the SMU used to take initial measurements. The green highlighted wire connects the SMU to the pillar wire shown in Figures 4.2 and 4.3. The yellow highlighted wire connects the SMU to the probe holder wire shown in Figure 4.1.

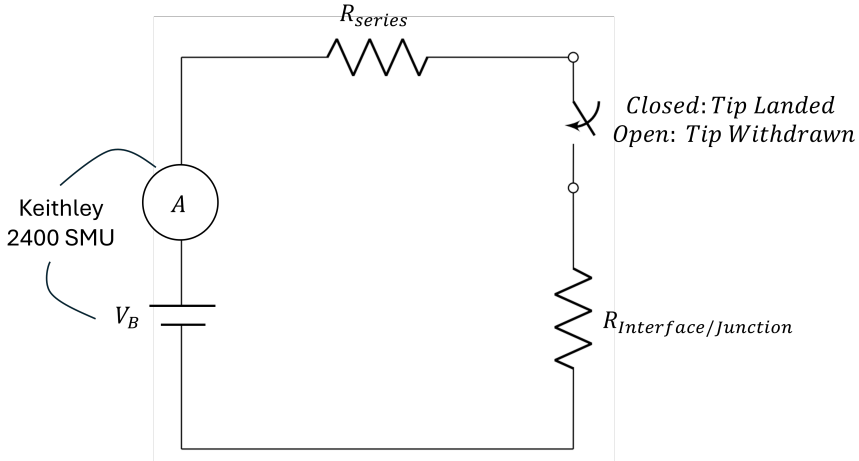


Figure 4.5: Circuit diagram of the system being tested. Voltage and current are sourced and sensed by Keithley SMU. Series resistance represents all resistances in series with the resistance of interface being made by the vdW tip. A closed or open switch represents the state of the AFM tip being engaged or widthdrawn from the surface.

The two interfaces that we expect to form, shown in Figure 4.6, are between the graphite tip and the gold surface of the pillar (G-Au) and between the graphite tip and the graphite on the pillar (G-G). Given the G-G interface inherently has a G-Au interface as well, one could naively assume that the recorded resistance of this junction should be larger than when the tip is landed directly on the gold. Although the resistivity of the two graphite to Au interfaces should be comparable, the contact area of the graphite flake on the Au pillar is orders of magnitude larger than that between the graphite on tip to the Au pillar. As a result, it is reasonable to compare the two configurations, and the total resistance in the G–G configuration may not necessarily exceed that of the G–Au case.

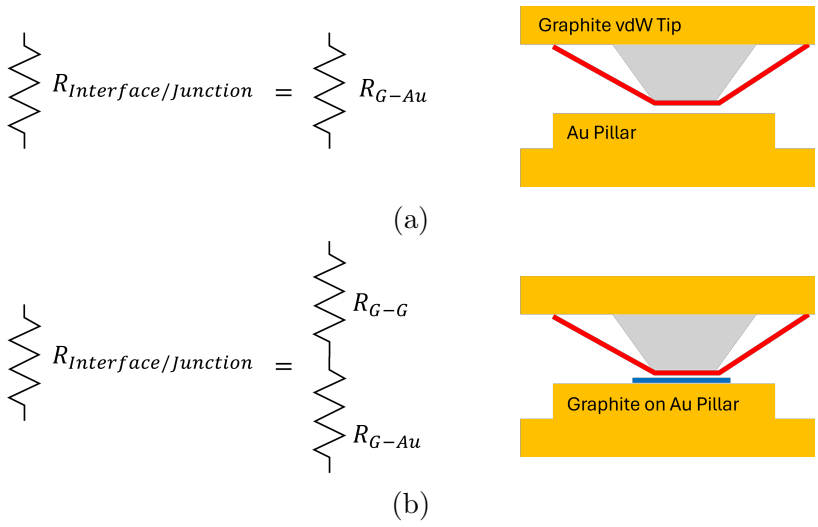


Figure 4.6: Schematic of the expected effective interface resistances for different landing conditions. a) When the tip is landed on Au, only a G-Au resistance makes up the interface. b) When the tip is landed on the graphite flake, the effective resistance should include the resistance between layers, G-G as well as the resistance between the flake on the tip and the pillar, G-Au. However the $R_{G-Au}$ in a) and b) are not comparable given the difference in contact area.

Confirmation of the following characteristics of the circuit drawn in Figure 4.5 should be sufficient to demonstrate that the system behaves as expected, and that 2D material interfaces can be established and characterized using this setup:

1. When the vdW tip is not engaged to the surface, an open circuit should be recorded.
2. Landing the vdW tip on the surface should close the circuit and result in a measurable conductance.
3. Different interfaces should have different measured resistances, allowing characterization of specific interfaces.
4. Conduction takes place through the vdW flake on the tip and not elsewhere on the cantilever.

## 4.2 Procedure

First, the custom AFM tip is loaded into the probe holder which is then mounted onto the AFM head. The laser is then aligned to the tip and the camera focus is fixed, as shown in Figure 4.7. The photodiode vertical deflection signal can then be zeroed. The AFM head is lifted and the coarse stage is repositioned to allow the custom stage to be attached.

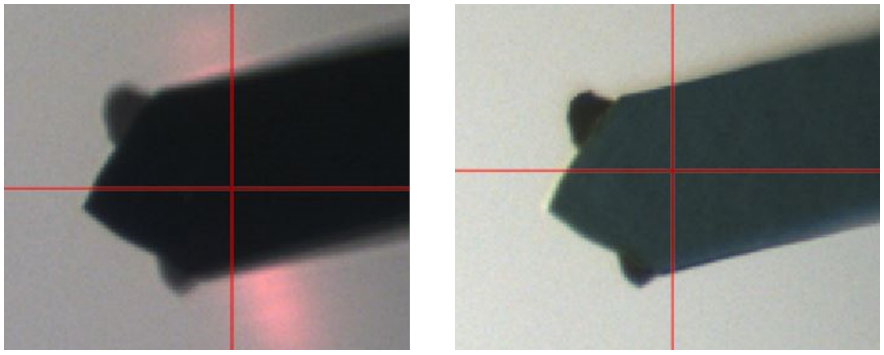

Figure 4.7: View of custom AFM tip/cantilever during the standard alignment process. Left: Laser alignment to the cantilever's shadow Right: Setting focus to the cantilever body.

With the inclined sample connected to the coarse movement of the AFM system, the sample can then be aligned to the laterally stationary head. The head is manually lowered until the outline of pillar is visible. The wires can then be attached to the SMU and the feedback loop is turned on to engage the tip. In Figure 4.8, the pillar can be seen to be in focus, while the AFM tip only comes into focus as it is engaged to the surface. The feedback loop is set with a low vertical deflection setpoint of 0.2V and low proportional and integral coefficients to ensure a slow landing and controlled tip approach. Calibration of the force to deflection setpoint was not performed and the setpoint and coefficients were not changed during the measurements. Once landed, the AFM can be used to scan in contact mode or current voltage (IV) curves can be taken.

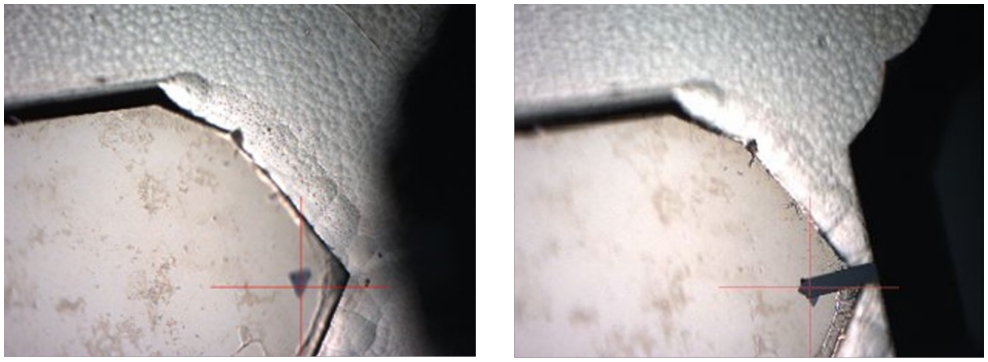


Figure 4.8: View of AFM tip through AFM system's camera both before and after tip landing. The sample pillar is always in focus as it only the cantilever that moves up and down into the focal plane with the head. a) Tip withdrawn, b) Tip engaged.

## 4.3 Results

This subchapter presents the measurements, in the order they were conducted, using the setup described above. To begin, in Figure 4.9, IV curves are taken with the tip withdrawn to confirm the lack of a short circuit. A short would indicate that for current to be drawn it does not have to pass through the conductive probe which would make it impossible to characterize a 2D material interface made with the vdW tip.

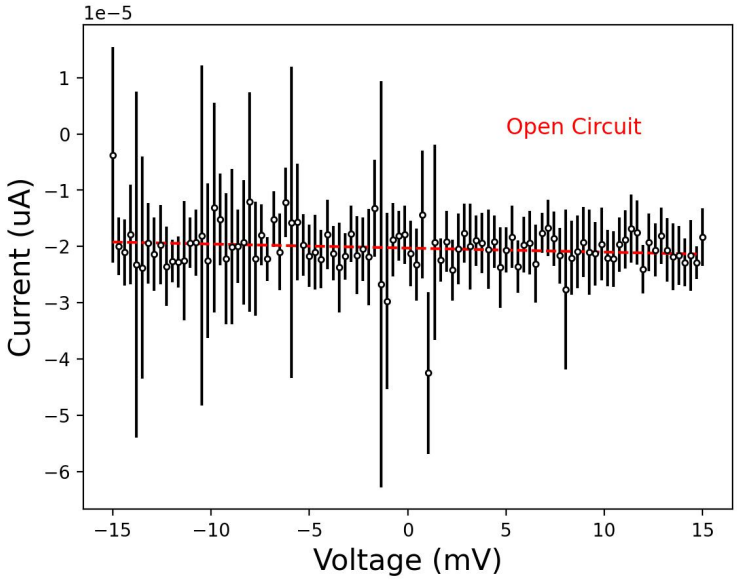


Figure 4.9: IV curve with the vdW tip not engaged to the surface showing an open circuit. Recorded current in black and linear regression in red.

The tip is then engaged on the Au pillar such that G-Au interfaces are formed and characterized. The two formed interfaces, shown in Figure 4.10, correspond to two distinct tip locations on the Au pillar. The first interface demonstrates conductivity with a total circuit resistance of $770 \pm 7\Omega$. While fairly linear, the current exhibits a step at the end of the voltage range. The interface made at the second location measured a lower conduction and non-monotonic behaviour in the current at the start and end of the voltage sweep. These measurements confirm that engaging the tip to the surface does close the circuit. Furthermore, the conductance of the interfaces appears to be sensitive to the details of the contact, which in this case is likely as a result of surface roughness. The observed nonlinear behaviour suggests that good contact is not always consistently achieved and that the contact of the interface may be unstable.

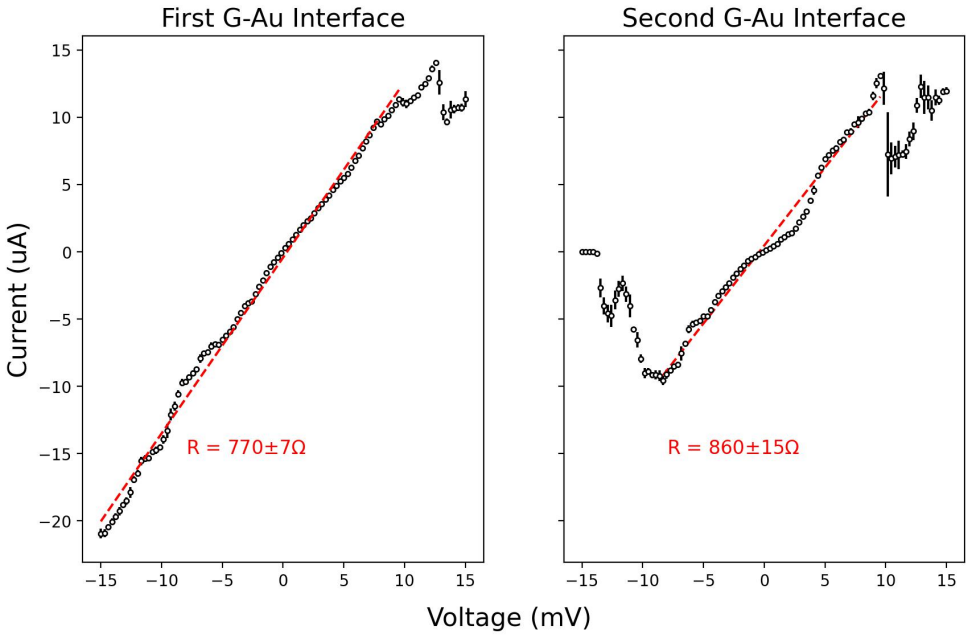


Figure 4.10: IV curves between the graphite vdW tip and two areas of the Au surface showing conduction. Recorded current in black and linear regression in red. First Interface: Linear regression performed on data between -15 to 10 mV. Second Interface: Linear regression performed on data between -8.5 to 10 mV

The tip was then withdrawn and, by visual inspection, landed on the graphite flake. The first G-G interface was measured, then the tip was withdrawn and reengaged in the same location on the graphite flake, such that the second G-G interface should be similar, if not the same. The resulting IV characteristics are shown in Figure 4.11. The voltage of the first G-G interface was restricted to -10 to 10 mV as a precaution for the first measurement through the graphite flake. The first interface has a very linear curve with low noise and resistance lower than that of the G-Au interfaces. In the second measurement, the resulting signal is significantly less linear with three different apparent slopes. The linearity and conductivity observed at the first interface indicate that a good electrical contact was established and suggest that

previous interfaces between the tip and the Au surface were poor. The second G-G interface fails to reestablish the same interface as the first despite being in the same location. In addition, the three different slopes present within the single voltage sweep further indicate instability in the interface.

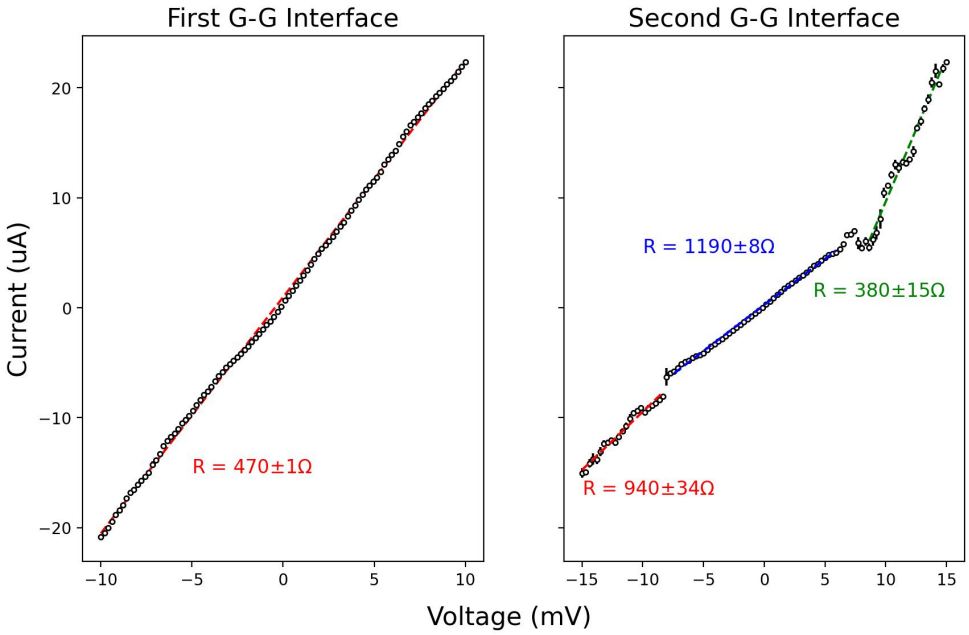


Figure 4.11: IV curves between the graphite vdW tip and graphite flake showing conduction. Recorded current in black and linear regressions coloured. First Interface: Linear regression performed on data between -10 to 10 mV. Second Interface: Linear regressions performed on data within the following ranges: -15 to -8 mV in red, -7.5 to 6mV in blue and 8.5 to 15mV in Green

Given that the alignment of the G-G interfaces was done by eye, it was prudent to ensure the tip was engaged to the graphite flake on the pillar. To ensure a G-G interface is made, a contact mode topographic scan was performed on the flake using the custom tip such that the tip could be deterministically placed onto the flake. A scan was initially completed on Au, then on the graphite flake. Both scans are 40x40

$um^2$, 64x64 pixels at 0.2Hz with unchanged gain settings and are found in Figures 4.12 and 4.13.

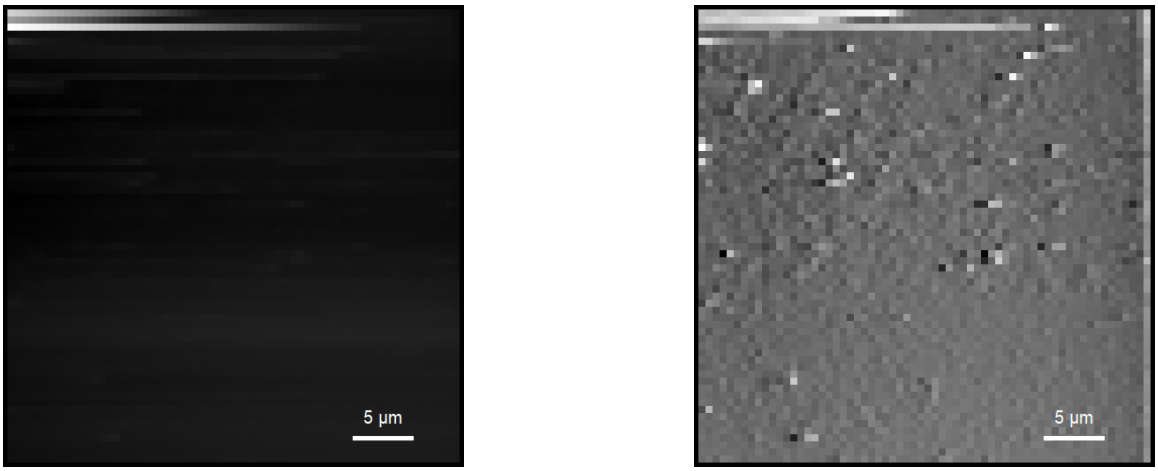


(a) (b)

Figure 4.12: Contact mode AFM scans of Au surface on raised pillar taken using custom vdW tip. 0.2V setpoint, 40x40 $um^2$, 64x64 pixels at 0.2Hz a) Topography, b) Tip deflection error.

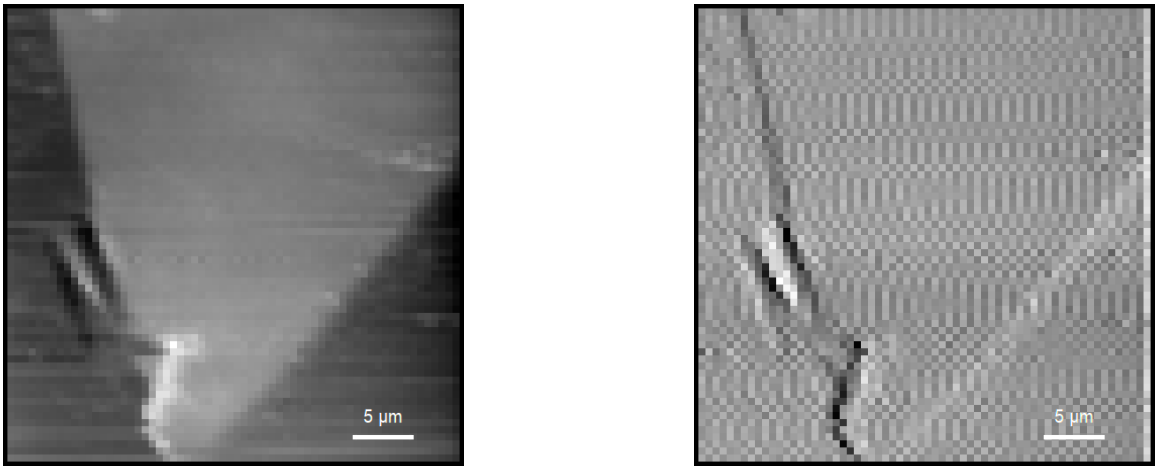


(a) (b)

Figure 4.13: Contact mode AFM scans of grapihite flake on raised pillar taken using custom vdW tip. 0.2V setpoint, 40x40 $um^2$, 64x64 pixels at 0.2Hz a) Topography, b) Tip deflection error.

The tip deflection error of the Au area scan shows the surface's roughness. The graphite flake topography and tip error deflection scans clearly show the outline of the flake. Notably, oscillations in the tip deflection error of the flake scan suggest a potentially poorly tuned, unstable control loop.

With a graphite scan complete, the tip was directed to the centre of the flake such that a G-G interface was guaranteed. Two voltage sweeps were taken and unexpectedly high resistances around 10MΩ were recorded in Figure 4.14.

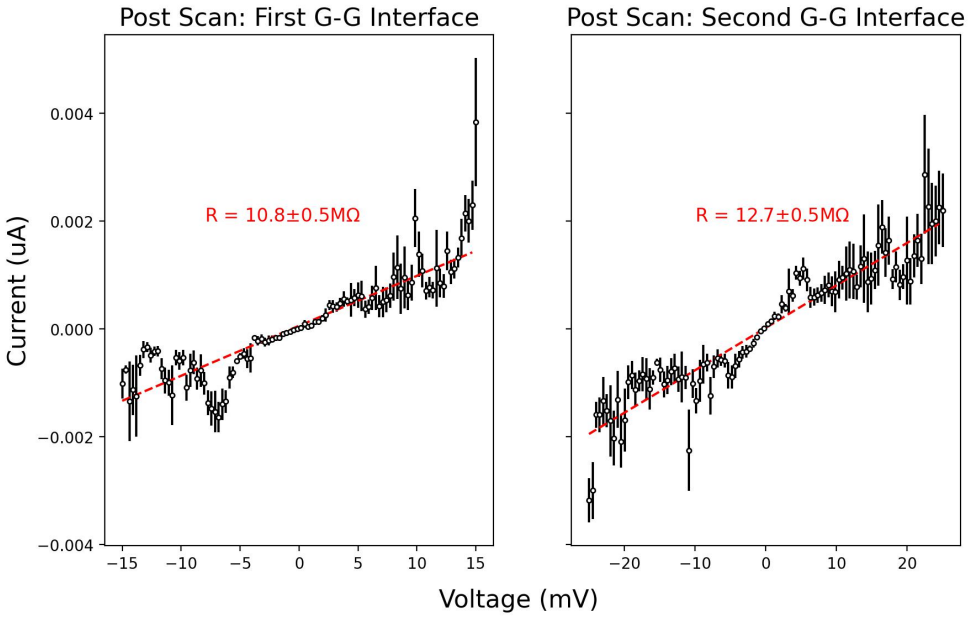


Figure 4.14: IV curves between the graphite vdW tip and graphite flake post topographic scans showing high resistance. Recorded current in black and linear regressions in red. Linear regressions of both the first and second interface were performed over entire voltage range.

To investigate, the tip was withdrawn and placed back onto Au. IV curves on Au, shown in Figure 4.15, indicate an open circuit.

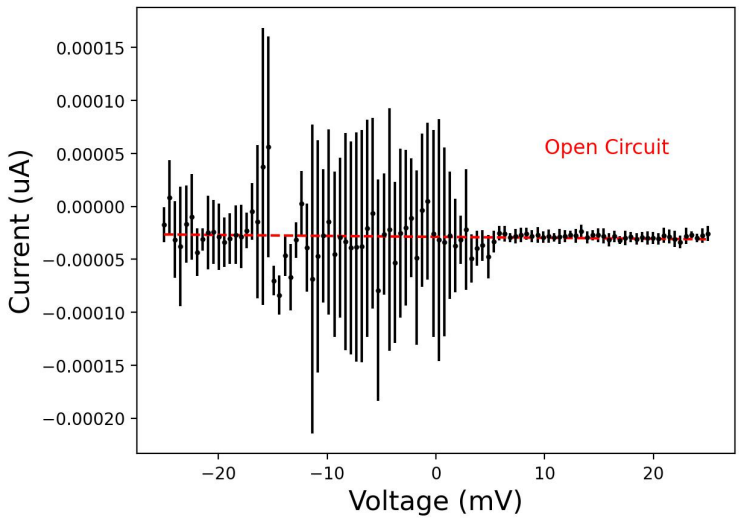


Figure 4.15: IV curves between the graphite vdW tip and gold post topographic scans showing open circuit. Recorded current in black and linear regression in red.

Due to the unexpected results, the tip was withdrawn and removed from the AFM head for further inspection. Figure 4.16 shows a comparison of the graphite tip before and after the measurements, and clearly indicates damage to the flake on the AFM tip. The graphite flake was probably torn during the scan performed on the rough Au surface. No further measurements were performed, as this was the only vdW tip we had remaining from process development.

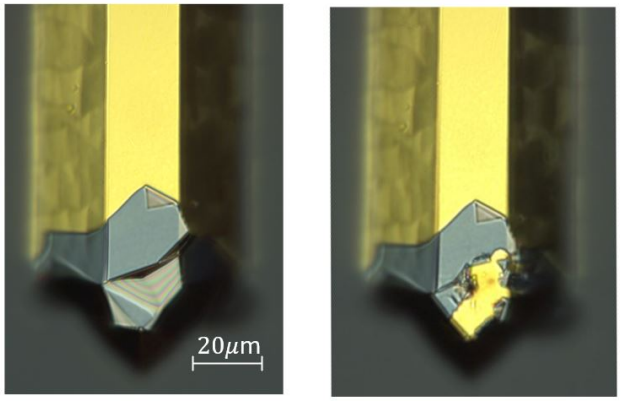


Figure 4.16: Comparison of graphite vdW tip prior to measurements and post topographic scans. a) Prior to the measurements performed in this section, the graphite flake tents over the custom tip forming a flat plateau b) Post topographic scans, the graphite is visibly torn from the custom tip.

## 4.4 Discussion

The measurements generally support the conclusion that the implemented system is capable of forming and characterizing 2D material interfaces. With the tip retracted and far from the surface, an open circuit was recorded, confirming that no short circuits were present in the system. When the graphite tip was engaged to the graphite flake or Au surface, a finite resistance was recorded, indicating that the tip closes the circuit and forms an interface. Furthermore, the variation in recorded resistances across measurements demonstrates the sensitivity of the system to different interfaces. Importantly, the loss of conductivity after the graphite was torn from the tip suggests that the previously recorded resistances were measured through the graphite on the tip. Had the graphite not been required for conduction, its removal would not have led to high resistance values.

However, the measurements revealed that the formed interfaces did not always have good contact and were not consistent. While the first G-G measurement demonstrated that stable and effective contact can be established, all other measurements displayed nonlinear features and increased noise. The inability to reestablish the same G-G interface at the same location on the flake, and the fact that the interface changed within a single voltage sweep, indicates a stability problem likely related to the control loop settings of the system. The oscillations present in the topographic scans on the graphite flake further corroborate the idea that the PID was poorly tuned.

A logical next step would be to address the stability and consistency of the formed interfaces. This would be done through optimization of the PID coefficients to limit oscillations. Furthermore, the effect of the vertical deflection setpoint should be investigated. A relatively low vertical deflection setpoint was appropriately chosen to avoid crashes and was not adjusted, but it is reasonable to believe that applying a greater force could improve the contact quality between the tip and flake. It would also be prudent for a larger area flake to be placed on the pillar or for it to be placed on a $Si/SiO_2$ pillar with patterned contacts to minimize the effect of surface roughness and reduce the risk of damage to the flake placed on the tip.

# Chapter 5

# Conclusions and Next Steps

In this thesis, the Quantum Twisting Microscope is described and the necessary steps/procedures to set one up in a lab are detailed and motivated. While this work presents a replication of that found in the original paper [7], the aim is that with all the required hardware, one could read this thesis as a very comprehensive guide that enables others to build and operate a QTM with minimal additional development.

Preliminary proof of concept measurements demonstrate that the system described in this thesis could be used to implement a fully functional QTM. To move toward a full implementation, some improvements are required. The next steps involve acquiring additional custom tips and preparing more samples to fully validate the functionality of the system. As our measurements indicate that the feedback coefficients and setpoint were suboptimal resulting in instability in the interface contact, this would require investigation. The use of shielded wires, less precarious connections with a PCB, and the use of the lock-in amplifier could be done fairly easily. Furthermore, xy positioners would need to be obtained to enable controlled rotation of the bottom

flake.

One of the limiting factors preventing additional measurements was the cost and time associated with fabricating the custom AFM tips with FIB deposition. During protocol development for transferring vdW materials onto the AFM cantilevers, three of four were broken. Although improvements to the protocol reduced the risk of damaging the cantilevers and allowed the final AFM tip to not be broken, there is still some inherent risk of breakage when handling them. Given the time and financial cost of the FIB deposition process, developing a more scalable method for custom tip production would be worthwhile.

Once the system is fully functional, benchmarking experiments to replicate results would be the next step. Generalizing the system to cryogenic temperatures, as has been done by the original authors, would then be a desirable improvement. However, in terms of novel ideas, I believe it would be fruitful to look at optically pumped QTM systems. Conceivably, one could find a way to measure Floquet states under optical excitation. In addition, while this thesis motivates measurements near the K points of graphene based samples given the excitement of flatbands, many other vdW materials could be looked at. Furthermore, there are proposals to look at flat bands near the M or $\Gamma$ points of other twisted materials [108, 109]. While this system could be used to probe the $\Gamma$ point, it should be able to take measurements near the M point of desirable materials with suitable selection of a probe material.

Altogether, I hope this work may be of some use to those aiming to implement a Quantum Twisting Microscope.

# Bibliography

[1] W. Ren, P. Bøggild, J. Redwing, K. Novoselov, L. Sun, Y. Qi, K. Jia, Z. Liu, O. Burton, J. Alexander-Webber, S. Hofmann, Y. Cao, Y. Long, Q.-H. Yang, D. Li, S. H. Choi, K. K. Kim, Y. H. Lee, M. Li, Q. Huang, Y. Gogotsi, N. Clark, A. Carl, R. Gorbachev, T. Olsen, J. Rosen, K. S. Thygesen, D. K. Efetov, B. S. Jessen, M. Yankowitz, J. Barrier, R. K. Kumar, F. H. L. Koppens, H. Deng, X. Li, S. Dai, D. N. Basov, X. Wang, S. Das, X. Duan, Z. Yu, M. Borsch, A. C. Ferrari, R. Huber, M. Kira, F. Xia, X. Wang, Z.-S. Wu, X. Feng, P. Simon, H.-M. Cheng, B. Liu, Y. Xie, W. Jin, R. R. Nair, Y. Xu, Q. Zhang, A. K. Katiyar, J.-H. Ahn, I. Aharonovich, M. C. Hersam, S. Roche, Q. Hua, G. Shen, T. Ren, H.-B. Zhang, C. M. Koo, N. Koratkar, V. Pellegrini, R. J. Young, B. Qu, M. Lemme, and A. J. Pollard, "The 2D Materials Roadmap," Apr. 2025. arXiv:2503.22476 [cond-mat].

[2] E. Koren, I. Leven, E. Lörtscher, A. Knoll, O. Hod, and U. Duerig, "Coherent commensurate electronic states at the interface between misoriented graphene layers," *Nature Nanotechnology*, vol. 11, pp. 752–757, Sept. 2016. Publisher: Nature Publishing Group.

[3] T. Chari, R. Ribeiro-Palau, C. R. Dean, and K. Shepard, "Resistivity of Rotated Graphite–Graphene Contacts," *Nano Letters*, vol. 16, pp. 4477–4482, July 2016. Publisher: American Chemical Society.

[4] R. Ribeiro-Palau, C. Zhang, K. Watanabe, T. Taniguchi, J. Hone, and C. R. Dean, "Twistable electronics with dynamically rotatable heterostructures," *Science*, vol. 361, pp. 690–693, Aug. 2018. Publisher: American Association for the Advancement of Science.

[5] Y. Yang, J. Li, J. Yin, S. Xu, C. Mullan, T. Taniguchi, K. Watanabe, A. K. Geim, K. S. Novoselov, and A. Mishchenko, "In situ manipulation of van der Waals heterostructures for twistronics," *Science Advances*, vol. 6, p. eabd3655, Dec. 2020. Publisher: American Association for the Advancement of Science.

[6] C. Hu, T. Wu, X. Huang, Y. Dong, J. Chen, Z. Zhang, B. Lyu, S. Ma, K. Watanabe, T. Taniguchi, G. Xie, X. Li, Q. Liang, and Z. Shi, "In-situ twistable bilayer graphene," *Scientific Reports*, vol. 12, p. 204, Jan. 2022. Publisher: Nature Publishing Group.

[7] A. Inbar, J. Birkbeck, J. Xiao, T. Taniguchi, K. Watanabe, B. Yan, Y. Oreg, A. Stern, E. Berg, and S. Ilani, "The quantum twisting microscope," *Nature*, vol. 614, pp. 682–687, Feb. 2023. Publisher: Nature Publishing Group.

[8] H. Tang, Y. Wang, X. Ni, K. Watanabe, T. Taniguchi, P. Jarillo-Herrero, S. Fan, E. Mazur, A. Yacoby, and Y. Cao, "On-chip multi-degree-of-freedom control of two-dimensional materials," *Nature*, vol. 632, pp. 1038–1044, Aug. 2024. Publisher: Nature Publishing Group.

[9] N. Wei, F. Von Oppen, and L. I. Glazman, "Dirac-point spectroscopy of flat-band systems with the quantum twisting microscope," *Physical Review B*, vol. 111, p. 085128, Feb. 2025.

[10] J. Birkbeck, J. Xiao, A. Inbar, T. Taniguchi, K. Watanabe, E. Berg, L. Glazman, F. Guinea, F. von Oppen, and S. Ilani, "Quantum twisting microscopy of phonons in twisted bilayer graphene," *Nature*, vol. 641, pp. 345–351, May 2025. Publisher: Nature Publishing Group.

[11] J. Xiao, E. Berg, L. I. Glazman, F. Guinea, S. Ilani, and F. Von Oppen, "Theory of phonon spectroscopy with the quantum twisting microscope," *Physical Review B*, vol. 110, p. 205407, Nov. 2024.

[12] N. Wei, F. Guinea, F. v. Oppen, and L. I. Glazman, "Theory of plasmon spectroscopy with the quantum twisting microscope," June 2025. arXiv:2506.05485 [cond-mat].

[13] V. Peri, S. Ilani, P. A. Lee, and G. Refael, "Probing quantum spin liquids with a quantum twisting microscope," *Physical Review B*, vol. 109, p. 035127, Jan. 2024. Publisher: American Physical Society.

[14] F. Pichler, W. Kadow, C. Kuhlenkamp, and M. Knap, "Probing magnetism in moir$\'e$ heterostructures with quantum twisting microscopes," *Physical Review B*, vol. 110, p. 045116, July 2024. Publisher: American Physical Society.

[15] D. R. Klein, U. Zondiner, A. Keren, J. Birkbeck, A. Inbar, J. Xiao, M. Sidorova, M. M. A. Ezzi, L. Peng, K. Watanabe, T. Taniguchi, S. Adam, and S. Ilani,

"Imaging the Sub-Moiré Potential Landscape using an Atomic Single Electron Transistor," Oct. 2024. arXiv:2410.22277 [cond-mat].

[16] P. Ajayan, P. Kim, and K. Banerjee, "Two-dimensional van der Waals materials," *Physics Today*, vol. 69, pp. 38–44, Sept. 2016.

[17] A. K. Geim and K. S. Novoselov, "The rise of graphene," *Nature Materials*, vol. 6, pp. 183–191, Mar. 2007. Publisher: Nature Publishing Group.

[18] P. R. Wallace, "The Band Theory of Graphite," *Physical Review*, vol. 71, pp. 622–634, May 1947. Publisher: American Physical Society.

[19] A. H. Castro Neto, F. Guinea, N. M. R. Peres, K. S. Novoselov, and A. K. Geim, "The electronic properties of graphene," *Reviews of Modern Physics*, vol. 81, pp. 109–162, Jan. 2009. Publisher: American Physical Society.

[20] K. S. Novoselov, A. K. Geim, S. V. Morozov, D. Jiang, Y. Zhang, S. V. Dubonos, I. V. Grigorieva, and A. A. Firsov, "Electric Field Effect in Atomically Thin Carbon Films," *Science*, vol. 306, pp. 666–669, Oct. 2004. Publisher: American Association for the Advancement of Science.

[21] K. S. Novoselov, D. Jiang, F. Schedin, T. J. Booth, V. V. Khotkevich, S. V. Morozov, and A. K. Geim, "Two-dimensional atomic crystals," *Proceedings of the National Academy of Sciences*, vol. 102, pp. 10451–10453, July 2005. Publisher: Proceedings of the National Academy of Sciences.

[22] C. R. Dean, A. F. Young, I. Meric, C. Lee, L. Wang, S. Sorgenfrei, K. Watanabe, T. Taniguchi, P. Kim, K. L. Shepard, and J. Hone, "Boron nitride substrates for

high-quality graphene electronics," *Nature Nanotechnology*, vol. 5, pp. 722–726, Oct. 2010. Publisher: Nature Publishing Group.

[23] A. K. Geim and I. V. Grigorieva, "Van der Waals heterostructures," *Nature*, vol. 499, pp. 419–425, July 2013. Publisher: Nature Publishing Group.

[24] Q. H. Wang, K. Kalantar-Zadeh, A. Kis, J. N. Coleman, and M. S. Strano, "Electronics and optoelectronics of two-dimensional transition metal dichalcogenides," *Nature Nanotechnology*, vol. 7, pp. 699–712, Nov. 2012. Publisher: Nature Publishing Group.

[25] B. Huang, G. Clark, E. Navarro-Moratalla, D. R. Klein, R. Cheng, K. L. Seyler, D. Zhong, E. Schmidgall, M. A. McGuire, D. H. Cobden, W. Yao, D. Xiao, P. Jarillo-Herrero, and X. Xu, "Layer-dependent ferromagnetism in a van der Waals crystal down to the monolayer limit," *Nature*, vol. 546, pp. 270–273, June 2017. Publisher: Nature Publishing Group.

[26] C. Gong, L. Li, Z. Li, H. Ji, A. Stern, Y. Xia, T. Cao, W. Bao, C. Wang, Y. Wang, Z. Q. Qiu, R. J. Cava, S. G. Louie, J. Xia, and X. Zhang, "Discovery of intrinsic ferromagnetism in two-dimensional van der Waals crystals," *Nature*, vol. 546, pp. 265–269, June 2017. Publisher: Nature Publishing Group.

[27] X. Xi, Z. Wang, W. Zhao, J.-H. Park, K. T. Law, H. Berger, L. Forró, J. Shan, and K. F. Mak, "Ising pairing in superconducting NbSe2 atomic layers," *Nature Physics*, vol. 12, pp. 139–143, Feb. 2016. Publisher: Nature Publishing Group.

[28] S. C. de la Barrera, M. R. Sinko, D. P. Gopalan, N. Sivadas, K. L. Seyler, K. Watanabe, T. Taniguchi, A. W. Tsen, X. Xu, D. Xiao, and B. M. Hunt,

"Tuning Ising superconductivity with layer and spin–orbit coupling in two-dimensional transition-metal dichalcogenides," *Nature Communications*, vol. 9, p. 1427, Apr. 2018. Publisher: Nature Publishing Group.

[29] Z. Fei, T. Palomaki, S. Wu, W. Zhao, X. Cai, B. Sun, P. Nguyen, J. Finney, X. Xu, and D. H. Cobden, "Edge conduction in monolayer WTe2," *Nature Physics*, vol. 13, pp. 677–682, July 2017. Publisher: Nature Publishing Group.

[30] X. Li, W. Cai, J. An, S. Kim, J. Nah, D. Yang, R. Piner, A. Velamakanni, I. Jung, E. Tutuc, S. K. Banerjee, L. Colombo, and R. S. Ruoff, "Large-Area Synthesis of High-Quality and Uniform Graphene Films on Copper Foils," *Science*, vol. 324, pp. 1312–1314, June 2009. Publisher: American Association for the Advancement of Science.

[31] S. M. Eichfeld, L. Hossain, Y.-C. Lin, A. F. Piasecki, B. Kupp, A. G. Birdwell, R. A. Burke, N. Lu, X. Peng, J. Li, A. Azcatl, S. McDonnell, R. M. Wallace, M. J. Kim, T. S. Mayer, J. M. Redwing, and J. A. Robinson, "Highly Scalable, Atomically Thin WSe2 Grown via Metal–Organic Chemical Vapor Deposition," *ACS Nano*, vol. 9, pp. 2080–2087, Feb. 2015. Publisher: American Chemical Society.

[32] K. Kang, S. Xie, L. Huang, Y. Han, P. Y. Huang, K. F. Mak, C.-J. Kim, D. Muller, and J. Park, "High-mobility three-atom-thick semiconducting films with wafer-scale homogeneity," *Nature*, vol. 520, pp. 656–660, Apr. 2015. Publisher: Nature Publishing Group.

[33] S. Thomas, "Paragraf: Leveraging the full potential of graphene from a microelectronics standpoint," Dec. 2021.

[34] K. S. Novoselov, A. K. Geim, S. V. Morozov, D. Jiang, M. I. Katsnelson, I. V. Grigorieva, S. V. Dubonos, and A. A. Firsov, "Two-dimensional gas of massless Dirac fermions in graphene," *Nature*, vol. 438, pp. 197–200, Nov. 2005. Number: 7065 Publisher: Nature Publishing Group.

[35] A. Splendiani, L. Sun, Y. Zhang, T. Li, J. Kim, C.-Y. Chim, G. Galli, and F. Wang, "Emerging Photoluminescence in Monolayer MoS2," *Nano Letters*, vol. 10, pp. 1271–1275, Apr. 2010. Publisher: American Chemical Society.

[36] K. S. Novoselov, A. Mishchenko, A. Carvalho, and A. H. Castro Neto, "2D materials and van der Waals heterostructures," *Science*, vol. 353, p. aac9439, July 2016. Publisher: American Association for the Advancement of Science.

[37] M. Kuwabara, D. R. Clarke, and D. A. Smith, "Anomalous superperiodicity in scanning tunneling microscope images of graphite," *Applied Physics Letters*, vol. 56, pp. 2396–2398, June 1990.

[38] J. E. Buckley, J. L. Wragg, H. W. White, A. Bruckdorfer, and D. L. Worcester, "Large-scale periodic features associated with surface boundaries in scanning tunneling microscope images of graphite," *Journal of Vacuum Science & Technology B: Microelectronics and Nanometer Structures Processing, Measurement, and Phenomena*, vol. 9, pp. 1079–1082, Mar. 1991.

[39] P. I. Oden, T. Thundat, L. A. Nagahara, S. M. Lindsay, G. B. Adams, and O. F. Sankey, "Superperiodic features observed on graphite under solution with scanning tunneling microscopy," *Surface Science*, vol. 254, pp. L454–L459, Aug. 1991.

[40] K. Kim, M. Yankowitz, B. Fallahazad, S. Kang, H. C. P. Movva, S. Huang, S. Larentis, C. M. Corbet, T. Taniguchi, K. Watanabe, S. K. Banerjee, B. J. LeRoy, and E. Tutuc, "van der Waals Heterostructures with High Accuracy Rotational Alignment," *Nano Letters*, vol. 16, pp. 1989–1995, Mar. 2016. Publisher: American Chemical Society.

[41] R. Bistritzer and A. H. MacDonald, "Moiré bands in twisted double-layer graphene," *Proceedings of the National Academy of Sciences*, vol. 108, pp. 12233–12237, July 2011.

[42] E. Y. Andrei and A. H. MacDonald, "Graphene bilayers with a twist," *Nature Materials*, vol. 19, pp. 1265–1275, Dec. 2020. Publisher: Nature Publishing Group.

[43] L. Balents, C. R. Dean, D. K. Efetov, and A. F. Young, "Superconductivity and strong correlations in moiré flat bands," *Nature Physics*, vol. 16, pp. 725–733, July 2020. Publisher: Nature Publishing Group.

[44] G. Li, A. Luican, J. M. B. Lopes dos Santos, A. H. Castro Neto, A. Reina, J. Kong, and E. Y. Andrei, "Observation of Van Hove singularities in twisted graphene layers," *Nature Physics*, vol. 6, pp. 109–113, Feb. 2010. Number: 2 Publisher: Nature Publishing Group.

[45] A. Luican, G. Li, A. Reina, J. Kong, R. R. Nair, K. S. Novoselov, A. K. Geim, and E. Y. Andrei, "Single-Layer Behavior and Its Breakdown in Twisted Graphene Layers," *Physical Review Letters*, vol. 106, p. 126802, Mar. 2011. Publisher: American Physical Society.

[46] Y. Cao, V. Fatemi, A. Demir, S. Fang, S. L. Tomarken, J. Y. Luo, J. D. Sanchez-Yamagishi, K. Watanabe, T. Taniguchi, E. Kaxiras, R. C. Ashoori, and P. Jarillo-Herrero, "Correlated insulator behaviour at half-filling in magic-angle graphene superlattices," *Nature*, vol. 556, pp. 80–84, Apr. 2018. Number: 7699 Publisher: Nature Publishing Group.

[47] Y. Cao, V. Fatemi, S. Fang, K. Watanabe, T. Taniguchi, E. Kaxiras, and P. Jarillo-Herrero, "Unconventional superconductivity in magic-angle graphene superlattices," *Nature*, vol. 556, pp. 43–50, Apr. 2018. Number: 7699 Publisher: Nature Publishing Group.

[48] P. J. Ledwith, A. Vishwanath, and E. Khalaf, "Exotic Carriers from Concentrated Topology: Dirac Trions as the Origin of the Missing Spectral Weight in Twisted Bilayer Graphene," May 2025. arXiv:2505.08779 [cond-mat].

[49] Z. Hao, A. M. Zimmerman, P. Ledwith, E. Khalaf, D. H. Najafabadi, K. Watanabe, T. Taniguchi, A. Vishwanath, and P. Kim, "Electric field–tunable superconductivity in alternating-twist magic-angle trilayer graphene," *Science*, vol. 371, pp. 1133–1138, Mar. 2021. Publisher: American Association for the Advancement of Science.

[50] T. Devakul, P. J. Ledwith, L.-Q. Xia, A. Uri, S. C. de la Barrera, P. Jarillo-Herrero, and L. Fu, "Magic-angle helical trilayer graphene," *Science Advances*, vol. 9, p. eadi6063, Sept. 2023. Publisher: American Association for the Advancement of Science.

[51] S. Chen, M. He, Y.-H. Zhang, V. Hsieh, Z. Fei, K. Watanabe, T. Taniguchi, D. H. Cobden, X. Xu, C. R. Dean, and M. Yankowitz, "Electrically tunable

correlated and topological states in twisted monolayer–bilayer graphene," *Nature Physics*, vol. 17, pp. 374–380, Mar. 2021. Publisher: Nature Publishing Group.

[52] C. Shen, Y. Chu, Q. Wu, N. Li, S. Wang, Y. Zhao, J. Tang, J. Liu, J. Tian, K. Watanabe, T. Taniguchi, R. Yang, Z. Y. Meng, D. Shi, O. V. Yazyev, and G. Zhang, "Correlated states in twisted double bilayer graphene," *Nature Physics*, vol. 16, pp. 520–525, May 2020. Publisher: Nature Publishing Group.

[53] T. Han, Z. Lu, G. Scuri, J. Sung, J. Wang, T. Han, K. Watanabe, T. Taniguchi, H. Park, and L. Ju, "Correlated insulator and Chern insulators in pentalayer rhombohedral-stacked graphene," *Nature Nanotechnology*, vol. 19, pp. 181–187, Feb. 2024. Publisher: Nature Publishing Group.

[54] M. I. Katsnelson, K. S. Novoselov, and A. K. Geim, "Chiral tunnelling and the Klein paradox in graphene," *Nature Physics*, vol. 2, pp. 620–625, Sept. 2006. Publisher: Nature Publishing Group.

[55] N. Stander, B. Huard, and D. Goldhaber-Gordon, "Evidence for Klein Tunneling in Graphene $p\mathrm{\text{\ensuremath{-}}}n$ Junctions," *Physical Review Letters*, vol. 102, p. 026807, Jan. 2009. Publisher: American Physical Society.

[56] A. F. Young and P. Kim, "Quantum interference and Klein tunnelling in graphene heterojunctions," *Nature Physics*, vol. 5, pp. 222–226, Mar. 2009. Publisher: Nature Publishing Group.

[57] T. Ando, T. Nakanishi, and R. Saito, "Berry's Phase and Absence of Back Scattering in Carbon Nanotubes," *Journal of the Physical Society of Japan*, vol. 67, pp. 2857–2862, Aug. 1998. Publisher: The Physical Society of Japan.

[58] J.-H. Chen, C. Jang, S. Xiao, M. Ishigami, and M. S. Fuhrer, "Intrinsic and extrinsic performance limits of graphene devices on SiO2," *Nature Nanotechnology*, vol. 3, pp. 206–209, Apr. 2008. Publisher: Nature Publishing Group.

[59] J. L. Mañes, F. Guinea, and M. A. H. Vozmediano, "Existence and topological stability of Fermi points in multilayered graphene," *Physical Review B*, vol. 75, p. 155424, Apr. 2007.

[60] J.-M. Hou and W. Chen, "Hidden symmetry and protection of Dirac points on the honeycomb lattice," *Scientific Reports*, vol. 5, p. 17571, Dec. 2015. Publisher: Nature Publishing Group.

[61] Y. Zhang, Y.-W. Tan, H. L. Stormer, and P. Kim, "Experimental observation of the quantum Hall effect and Berry's phase in graphene," *Nature*, vol. 438, pp. 201–204, Nov. 2005. Publisher: Nature Publishing Group.

[62] D. Xiao, M.-C. Chang, and Q. Niu, "Berry phase effects on electronic properties," *Reviews of Modern Physics*, vol. 82, pp. 1959–2007, July 2010. Publisher: American Physical Society.

[63] F. D. M. Haldane, "Model for a Quantum Hall Effect without Landau Levels: Condensed-Matter Realization of the "Parity Anomaly"," *Physical Review Letters*, vol. 61, pp. 2015–2018, Oct. 1988. Publisher: American Physical Society.

[64] M. Serlin, C. L. Tschirhart, H. Polshyn, Y. Zhang, J. Zhu, K. Watanabe, T. Taniguchi, L. Balents, and A. F. Young, "Intrinsic quantized anomalous Hall effect in a moiré heterostructure," *Science*, vol. 367, pp. 900–903, Feb. 2020. Publisher: American Association for the Advancement of Science.

[65] S. Y. Zhou, G.-H. Gweon, A. V. Fedorov, P. N. First, W. A. de Heer, D.-H. Lee, F. Guinea, A. H. Castro Neto, and A. Lanzara, "Substrate-induced bandgap opening in epitaxial graphene," *Nature Materials*, vol. 6, pp. 770–775, Oct. 2007. Publisher: Nature Publishing Group.

[66] G. Giovannetti, P. A. Khomyakov, G. Brocks, P. J. Kelly, and J. van den Brink, "Substrate-induced band gap in graphene on hexagonal boron nitride: Ab initio density functional calculations," *Physical Review B*, vol. 76, p. 073103, Aug. 2007. Publisher: American Physical Society.

[67] K. Watanabe, T. Taniguchi, and H. Kanda, "Direct-bandgap properties and evidence for ultraviolet lasing of hexagonal boron nitride single crystal," *Nature Materials*, vol. 3, pp. 404–409, June 2004. Publisher: Nature Publishing Group.

[68] S. Mitra, Jiménez-Galán, M. Aulich, M. Neuhaus, R. E. F. Silva, V. Pervak, M. F. Kling, and S. Biswas, "Light-wave-controlled Haldane model in monolayer hexagonal boron nitride," *Nature*, vol. 628, pp. 752–757, Apr. 2024. Publisher: Nature Publishing Group.

[69] N. W. Ashcroft and N. D. Mermin, *Solid State Physics*. Fort Worth: Saunders College Publishing, 1976.

[70] S. Carr, S. Fang, and E. Kaxiras, "Electronic-structure methods for twisted moiré layers," *Nature Reviews Materials*, vol. 5, pp. 748–763, Oct. 2020. Publisher: Nature Publishing Group.

[71] D. M. Kennes, M. Claassen, L. Xian, A. Georges, A. J. Millis, J. Hone, C. R. Dean, D. N. Basov, A. N. Pasupathy, and A. Rubio, "Moiré heterostructures as a condensed-matter quantum simulator," *Nature Physics*, vol. 17, pp. 155–163, Feb. 2021. Publisher: Nature Publishing Group.

[72] J. M. B. Lopes dos Santos, N. M. R. Peres, and A. H. Castro Neto, "Graphene Bilayer with a Twist: Electronic Structure," *Physical Review Letters*, vol. 99, p. 256802, Dec. 2007.

[73] K. Bian, C. Gerber, A. J. Heinrich, D. J. Müller, S. Scheuring, and Y. Jiang, "Scanning probe microscopy," *Nature Reviews Methods Primers*, vol. 1, pp. 1–29, May 2021. Publisher: Nature Publishing Group.

[74] E. J. Mele, "Commensuration and interlayer coherence in twisted bilayer graphene," *Physical Review B*, vol. 81, p. 161405, Apr. 2010. Publisher: American Physical Society.

[75] Y. Kim, H. Yun, S.-G. Nam, M. Son, D. S. Lee, D. C. Kim, S. Seo, H. C. Choi, H.-J. Lee, S. W. Lee, and J. S. Kim, "Breakdown of the Interlayer Coherence in Twisted Bilayer Graphene," *Physical Review Letters*, vol. 110, p. 096602, Feb. 2013.

[76] R. Bistritzer and A. H. MacDonald, "Transport between twisted graphene layers," *Physical Review B*, vol. 81, p. 245412, June 2010. Publisher: American Physical Society.

[77] L. Simon, C. Bena, F. Vonau, M. Cranney, and D. Aubel, "Fourier-transform scanning tunnelling spectroscopy: the possibility to obtain constant-energy maps and band dispersion using a local measurement," *Journal of Physics D: Applied Physics*, vol. 44, p. 464010, Nov. 2011.

[78] N. Avraham, J. Reiner, A. Kumar-Nayak, N. Morali, R. Batabyal, B. Yan, and H. Beidenkopf, "Quasiparticle Interference Studies of Quantum Materials," *Advanced Materials*, vol. 30, no. 41, p. 1707628, 2018. _eprint: https://advanced.onlinelibrary.wiley.com/doi/pdf/10.1002/adma.201707628.

[79] A. Damascelli, Z. Hussain, and Z.-X. Shen, "Angle-resolved photoemission studies of the cuprate superconductors," *Reviews of Modern Physics*, vol. 75, pp. 473–541, Apr. 2003.

[80] S. Lisi, X. Lu, T. Benschop, T. A. de Jong, P. Stepanov, J. R. Duran, F. Margot, I. Cucchi, E. Cappelli, A. Hunter, A. Tamai, V. Kandyba, A. Giampietri, A. Barinov, J. Jobst, V. Stalman, M. Leeuwenhoek, K. Watanabe, T. Taniguchi, L. Rademaker, S. J. van der Molen, M. P. Allan, D. K. Efetov, and F. Baumberger, "Observation of flat bands in twisted bilayer graphene," *Nature Physics*, vol. 17, pp. 189–193, Feb. 2021. Publisher: Nature Publishing Group.

[81] R. Wiesendanger, *Scanning Probe Microscopy and Spectroscopy: Methods and Applications*. Cambridge University Press, 1994.

[82] I. Giaever, "Energy Gap in Superconductors Measured by Electron Tunneling," *Physical Review Letters*, vol. 5, pp. 147–148, Aug. 1960. Publisher: American Physical Society.

[83] P. K. Hansma, "Inelastic electron tunneling," *Physics Reports*, vol. 30, pp. 145–206, Apr. 1977.

[84] J. Smoliner, W. Demmerle, G. Berthold, E. Gornik, G. Weimann, and W. Schlapp, "Momentum conservation in tunneling processes between barrier-separated 2D-electron-gas systems," *Physical Review Letters*, vol. 63, pp. 2116–2119, Nov. 1989.

[85] J. P. Eisenstein, T. J. Gramila, L. N. Pfeiffer, and K. W. West, "Probing a two-dimensional Fermi surface by tunneling," *Physical Review B*, vol. 44, pp. 6511–6514, Sept. 1991. Publisher: American Physical Society.

[86] H. M. Yoo, M. Korkusinski, D. Miravet, K. W. Baldwin, K. West, L. Pfeiffer, P. Hawrylak, and R. C. Ashoori, "Time, momentum, and energy resolved pump-probe tunneling spectroscopy of two-dimensional electron systems," *Nature Communications*, vol. 14, p. 7440, Nov. 2023. Publisher: Nature Publishing Group.

[87] J. Jang, H. M. Yoo, L. N. Pfeiffer, K. W. West, K. W. Baldwin, and R. C. Ashoori, "Full momentum- and energy-resolved spectral function of a 2D electronic system," *Science*, vol. 358, pp. 901–906, Nov. 2017. Publisher: American Association for the Advancement of Science.

[88] Z. Zhang, S. Wu, D. Călugăru, H. Hu, T. Taniguchi, K. Wanatabe, A. B. Bernevig, and E. Y. Andrei, "Heavy fermions, mass renormalization and local moments in magic-angle twisted bilayer graphene via planar tunneling spectroscopy," Mar. 2025. arXiv:2503.17875 [cond-mat].

[89] K. Takeyama, R. Moriya, S. Okazaki, Y. Zhang, S. Masubuchi, K. Watanabe, T. Taniguchi, T. Sasagawa, and T. Machida, "Resonant Tunneling Due to van der Waals Quantum-Well States of Few-Layer WSe2 in WSe2/h-BN/p+-MoS2 Junction," *Nano Letters*, vol. 21, pp. 3929–3934, May 2021. Publisher: American Chemical Society.

[90] K. Kinoshita, R. Moriya, S. Okazaki, Y. Zhang, S. Masubuchi, K. Watanabe, T. Taniguchi, T. Sasagawa, and T. Machida, "Polarity-dependent twist-controlled resonant tunneling device based on few-layer W Se 2," *Physical Review Research*, vol. 5, p. 043292, Dec. 2023.

[91] C. Zhou, H. Li, Z. Huang, C. Y. Wan, Z. Jin, J. Liu, and J. Wang, "Probing Electronic Band Structure of Monolayer MoS2 in Gate-Controlled Resonant Tunneling Diodes," *ACS Applied Materials & Interfaces*, vol. 17, pp. 25915–25921, Apr. 2025. Publisher: American Chemical Society.

[92] G. W. Burg, N. Prasad, B. Fallahazad, A. Valsaraj, K. Kim, T. Taniguchi, K. Watanabe, Q. Wang, M. J. Kim, L. F. Register, and E. Tutuc, "Coherent Interlayer Tunneling and Negative Differential Resistance with High Current Density in Double Bilayer Graphene–WSe2 Heterostructures," *Nano Letters*, vol. 17, pp. 3919–3925, June 2017. Publisher: American Chemical Society.

[93] L. Britnell, R. V. Gorbachev, R. Jalil, B. D. Belle, F. Schedin, A. Mishchenko, T. Georgiou, M. I. Katsnelson, L. Eaves, S. V. Morozov, N. M. R. Peres, J. Leist, A. K. Geim, K. S. Novoselov, and L. A. Ponomarenko, "Field-Effect Tunneling Transistor Based on Vertical Graphene Heterostructures," *Science*, vol. 335, pp. 947–950, Feb. 2012. Publisher: American Association for the Advancement of Science.

[94] A. Mishchenko, J. S. Tu, Y. Cao, R. V. Gorbachev, J. R. Wallbank, M. T. Greenaway, V. E. Morozov, S. V. Morozov, M. J. Zhu, S. L. Wong, F. Withers, C. R. Woods, Y.-J. Kim, K. Watanabe, T. Taniguchi, E. E. Vdovin, O. Makarovsky, T. M. Fromhold, V. I. Fal'ko, A. K. Geim, L. Eaves, and K. S. Novoselov, "Twist-controlled resonant tunnelling in graphene/boron nitride/graphene heterostructures," *Nature Nanotechnology*, vol. 9, pp. 808–813, Oct. 2014. Publisher: Nature Publishing Group.

[95] J. R. Wallbank, D. Ghazaryan, A. Misra, Y. Cao, J. S. Tu, B. A. Piot, M. Potemski, S. Pezzini, S. Wiedmann, U. Zeitler, T. L. M. Lane, S. V. Morozov, M. T. Greenaway, L. Eaves, A. K. Geim, V. I. Fal'ko, K. S. Novoselov, and A. Mishchenko, "Tuning the valley and chiral quantum state of Dirac electrons in van der Waals heterostructures," *Science*, vol. 353, pp. 575–579, Aug. 2016. Publisher: American Association for the Advancement of Science.

[96] S. Luryi, "Quantum capacitance devices," *Applied Physics Letters*, vol. 52, pp. 501–503, Feb. 1988.

[97] R. C. Ashoori, H. L. Stormer, J. S. Weiner, L. N. Pfeiffer, S. J. Pearton, K. W. Baldwin, and K. W. West, "Single-electron capacitance spectroscopy of discrete

quantum levels," *Physical Review Letters*, vol. 68, pp. 3088–3091, May 1992.

[98] G. D. Mahan, *Many-Particle Physics*. Boston, MA: Springer US, 2000.

[99] E. H. Hwang and S. Das Sarma, "Quasiparticle spectral function in doped graphene: Electron-electron interaction effects in ARPES," *Physical Review B*, vol. 77, p. 081412, Feb. 2008.

[100] S. Ulstrup, R. J. Koch, S. Singh, K. M. McCreary, B. T. Jonker, J. T. Robinson, C. Jozwiak, E. Rotenberg, A. Bostwick, J. Katoch, and J. A. Miwa, "Direct observation of minibands in a twisted graphene/WS2 bilayer," *Science Advances*, vol. 6, p. eaay6104, Apr. 2020. Publisher: American Association for the Advancement of Science.

[101] W. Jin, P.-C. Yeh, N. Zaki, D. Chenet, G. Arefe, Y. Hao, A. Sala, T. O. Mentes, J. I. Dadap, A. Locatelli, J. Hone, and R. M. Osgood, "Tuning the electronic structure of monolayer graphene/ Mo S 2 van der Waals heterostructures via interlayer twist," *Physical Review B*, vol. 92, p. 201409, Nov. 2015.

[102] S. Reyntjens and R. Puers, "A review of focused ion beam applications in microsystem technology," *Journal of Micromechanics and Microengineering*, vol. 11, p. 287, July 2001.

[103] H. Seidel, L. Csepregi, A. Heuberger, and H. Baumgartel, "Anisotropic etching of crystalline silicon in alkaline solutions. II. Influence of dopants," *Journal of The Electrochemical Society*, vol. 137, no. 1t, 1990.

[104] N. Lim, Y. S. Choi, A. Efremov, and K.-H. Kwon, "Dry Etching Performance and Gas-Phase Parameters of C6F12O + Ar Plasma in Comparison with CF4

+ Ar," *Materials*, vol. 14, p. 1595, Jan. 2021. Number: 7 Publisher: Multidisciplinary Digital Publishing Institute.

[105] K. Williams, K. Gupta, and M. Wasilik, "Etch rates for micromachining processing-Part II," *Journal of Microelectromechanical Systems*, vol. 12, pp. 761–778, Dec. 2003.

[106] P. Blake, E. W. Hill, A. H. Castro Neto, K. S. Novoselov, D. Jiang, R. Yang, T. J. Booth, and A. K. Geim, "Making graphene visible," *Applied Physics Letters*, vol. 91, p. 063124, Aug. 2007.

[107] J. Boddison-Chouinard, R. Plumadore, and A. Luican-Mayer, "Fabricating van der Waals Heterostructures with Precise Rotational Alignment," *Journal of Visualized Experiments (JoVE)*, p. e59727, July 2019.

[108] M. Angeli and A. H. MacDonald, " valley transition metal dichalcogenide moiré bands," *Proceedings of the National Academy of Sciences*, vol. 118, p. e2021826118, Mar. 2021. Publisher: Proceedings of the National Academy of Sciences.

[109] D. Călugăru, Y. Jiang, H. Hu, H. Pi, J. Yu, M. G. Vergniory, J. Shan, C. Felser, L. M. Schoop, D. K. Efetov, K. F. Mak, and B. A. Bernevig, "Moiré materials based on M-point twisting," *Nature*, vol. 643, pp. 376–381, July 2025. Publisher: Nature Publishing Group.

[110] L. Wang, I. Meric, P. Y. Huang, Q. Gao, Y. Gao, H. Tran, T. Taniguchi, K. Watanabe, L. M. Campos, D. A. Muller, J. Guo, P. Kim, J. Hone, K. L.

Shepard, and C. R. Dean, "One-Dimensional Electrical Contact to a Two-Dimensional Material," *Science*, vol. 342, pp. 614–617, Nov. 2013. Publisher: American Association for the Advancement of Science.

[111] V. Patil, S. Ghosh, A. Basu, Kuldeep, A. Dutta, K. Agrawal, N. Bhatia, A. Shah, D. A. Jangade, R. Kulkarni, A. Thamizhavel, and M. M. Deshmukh, "Pick-up and assembling of chemically sensitive van der Waals heterostructures using dry cryogenic exfoliation," *Scientific Reports*, vol. 14, p. 11097, May 2024. Publisher: Nature Publishing Group.

[112] J. Diez-Merida, I. Das, G. D. Battista, A. Diez-Carlon, M. Lee, L. Zeng, K. Watanabe, T. Taniguchi, E. Olsson, and D. K. Efetov, "High-yield fabrication of bubble-free magic-angle twisted bilayer graphene devices with high twist-angle homogeneity," May 2024. arXiv:2405.11323 [cond-mat].

# Appendices

# A Methods

Here, I discuss standard 2D material device fabrication techniques commonly used in our lab.

## A.1 Mechanical Exfoliation

As mentioned in the main body, 2D materials in their bulk are stacks of individual layers only loosely bound to each other by vdW forces. Monolayers or few layers of material can be isolated by overcoming the vdW forces to adjacent layers, often done with mechanical exfoliation [20, 21]. The process involves the preparation of a Si substrate with 285nm $SiO_2$, required to achieve optimal optical contrast of the exfoliated flakes [106]. Next, a bulk crystal is thinned out on a piece of tape and the prepared substrate is pressed onto the tape. In detail:

- Use a diamond scribe to cleave a Si wafer with 285nm of oxide into smaller substrates.
- Clean the substrates by sequentially placing them for approximately 5 minutes each in an acetone bath, followed by an isopropyl alcohol (IPA) bath, and finally in a distilled water (DI). After rinsing, blow off excess water using nitrogen. Then place the substrate on a hotplate at a temperature above 100°C to evaporate any remaining moisture. The DI bath followed by the hotplate are optional.
- Place a small piece of your layered material onto a piece of adhesive tape.

- Thin the crystal by repeatedly folding clean sections of tape onto the flake until a large area of the tape is covered with thin flakes.
- It is simplest to now press the cleaned substrate onto the thinned out flakes on the tape.

For hBN and TMDs, prior to placing the substrate onto the flakes an intermediate step is used to improve the yield.

- Cut a square of polydimethylsiloxane (PDMS) roughly into the shape and size of the substrate.
- Press the PDMS onto the thinned out flakes on the tape
- Remove the PDMS from the tape and place it flake side down onto the cleaned substrate.
- Place the substrate and PDMS onto a hotplate between 80-100°C for 5 minutes then peel the PDMS from the substrate.

Once the flakes have been placed on a prepared substrate, their thicknesses can be identified under an optical microscope by their contrast. For more confirmation of the layer count, AFM or Raman spectroscopy can be used.

## A.2 Polymer Stamp Preparation

Once crystals have been exfoliated onto substrates and desirable flakes have been identified, the dry transfer technique can be used to fabricate heterostructures [110].

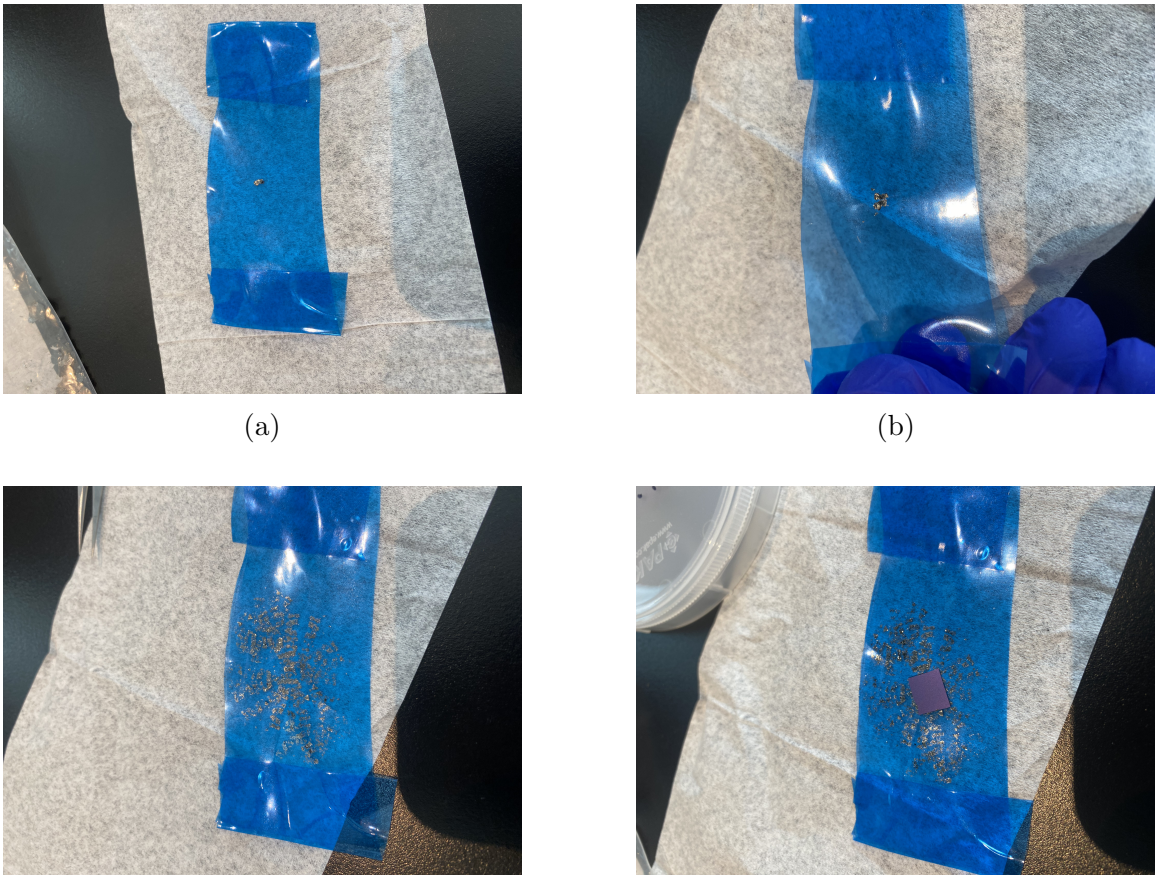

(a) (b)

(c) (d)

Figure A.1: Mechanical exfoliation process. a) Small flake of graphite placed on tape. b) After the small flake was folded once showing a mirrored copy. c) After the tape has been folded on itself many times. d)A 285nm $SiO_2$/Si wafer placed on the thinned crystal.

This technique uses the temperature dependent adhesion of a polymer stamp to overcome the vdW forces between a flakes and substrate. A variety of polymers are used by different labs, but we use a thin polypropylene carbonate (PPC) film supported by a protruding soft polydimethylsiloxane (PDMS) stamp on a glass slide, shown in Figure A.2, to make contact with the flake.

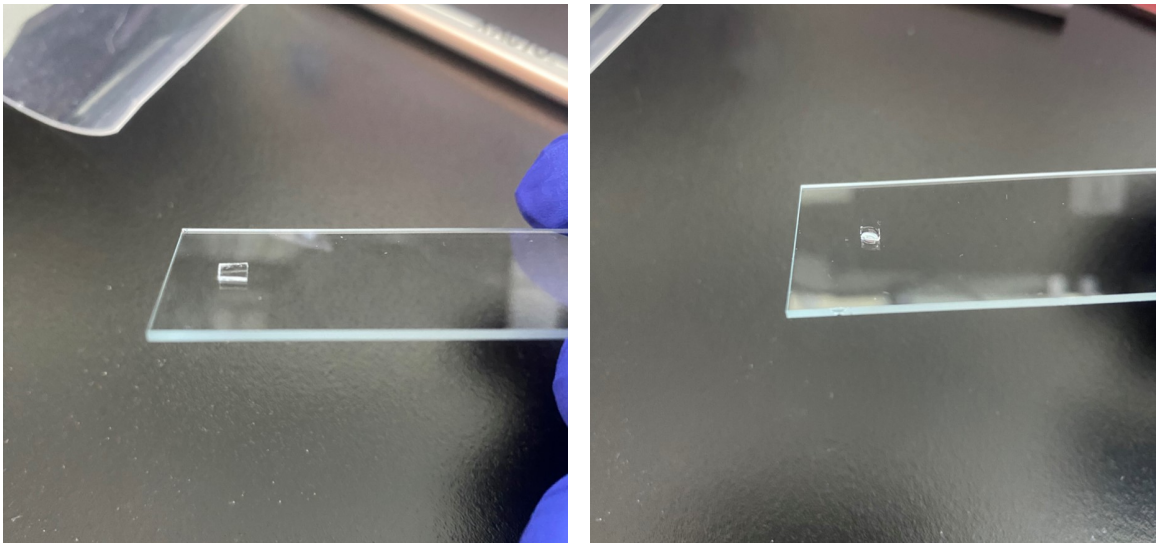

(a) (b)

Figure A.2: PDMS on glass slides. a) Square of precured Gel Pak PDMS placed on a glass slide. b) Hemisphere of PDMS cured in lab placed on a glass slide.

PPC has a glass transition temperature ($T_g$) near 40°C at which it its adhesion to 2D materials becomes higher than that of the substrate. PPC is soluble in acetone and requires a relatively low operating temperature range. The PDMS is relatively soft and does not come in contact with the flakes, but allows for controlled contact between the PPC film and the substrate/flake. The adhesion of PDMS can be used and has recently been demonstrated [111]; however its $T_g$ requires a liquid nitrogen setup to reach. The polymer stamps are made in the following way:

- PPC in solid form is mixed with anisole in a 17:3 ratio by mass
- PPC solution is spun on a clean Si substrate at 1500 RPM and placed on a 75°C hotplate for 5 minutes
- The PPC films are carefully removed from the substrates with a tape window.

- PDMS is placed on a glass slide
- Optionally, the PDMS can undergo an oxygen plasma etching cycle at 50W for 2 minutes to promote adhesion between the PPC and PDMS
  - Planar PDMS squares can be cut from purchased precured PDMS sheets
  - Hemispherical PDMS squares can be made from uncured PDMS kits. Briefly, the kits come with the correct ratio of polymer to curing agent and are mixed together. A small drop is dispensed on a glass slide and is cured on a hotplate at 100°C for 10-15 minutes [111].
- The PPC supported by the tape window is placed overtop of the PDMS protrusion.

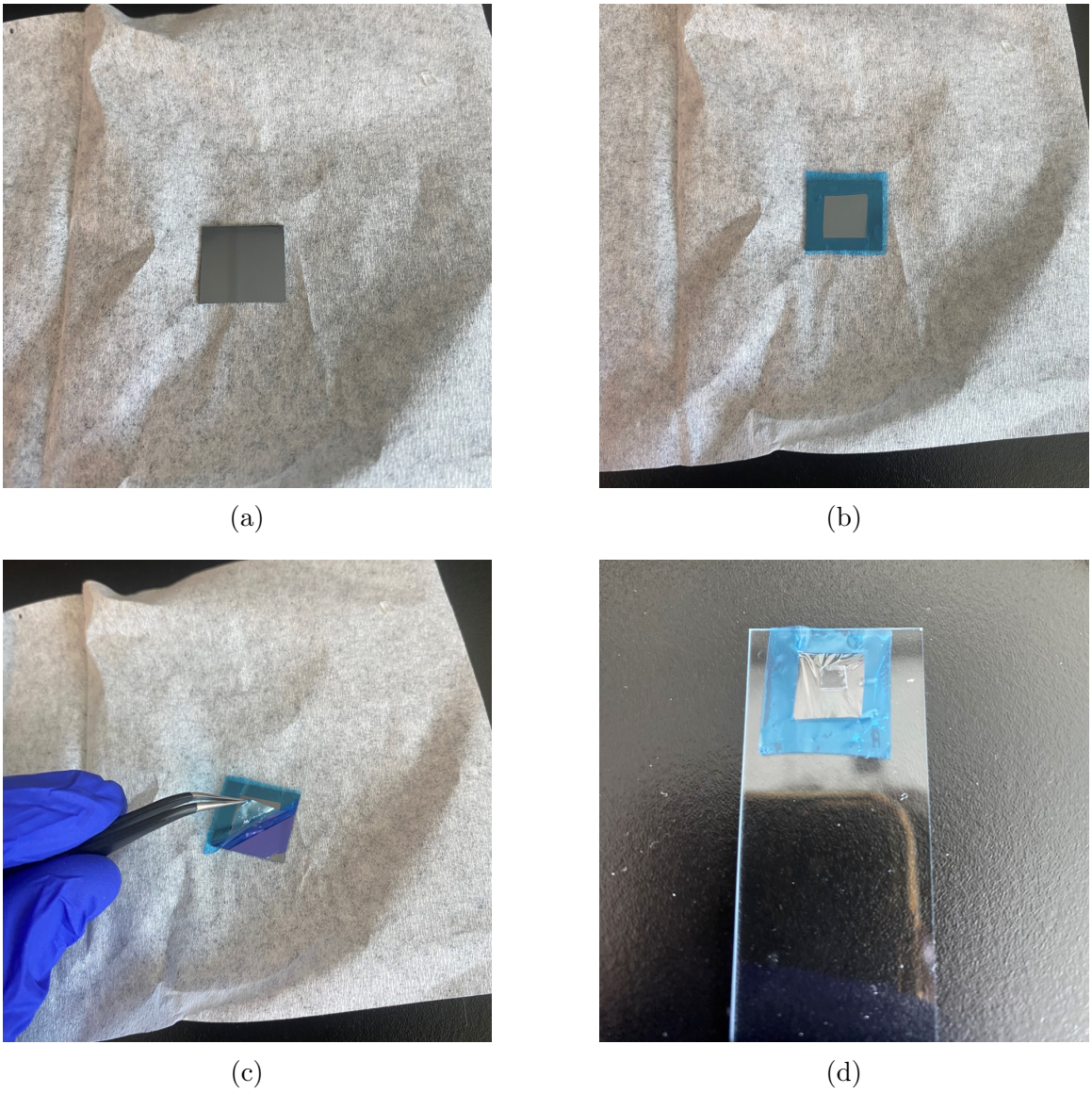

(a) (b)

(c) (d)

Figure A.3: Polymer stamp making process. a) PPC film on $SiO_2$/Si substrate. b) Tape frame placed on PPC film. c) Removal of the PPC film with the tape frame. d) PPC film placed on PDMS square on a glass slide.

Planar pre-cured PDMS squares are generally sufficient, however I have personally found hemispherical PDMS transfers to be more controlled and can minimize the contact area that the film makes with the substrate. The ability to control the size

of the contact area can play an important role in certain scenarios (Appendix B).

### A.3 Heterostructure Preparation

Once flakes have been identified and PPC/PDMS stamps have been prepared, flakes can be picked up and stacked to create vdW heterostructures. A substrate with an identified vdW flake is placed on a set of stepper motors with x,y,z and rotation degrees of freedom underneath an optical microscope. The polymer stamp glass slide is held overtop the substrate with a set of piezoelectric motors with x,y and z degrees of freedom. Briefly, the flake of interest is raised to the focal plane and is centred to the field of view of the optical microscope. The PDMS/PPC film is slowly brought into contact with the substrate between 40-45°C, ideally not initially directly on the flake of interest. The point of contact between the film and the substrate is easily identified by the characteristic Newton's rings. The point of contact is slowly brought across the flake by continuously lowering the glass slide. After the flake is completely covered, it should adhere more strongly to the PPC than to the substrate. The substrate stage is then lowered, allowing the flake to transfer onto the stamp. To pick up subsequent layers, the same procedure is followed except already picked up flakes must be aligned laterally with the flakes to be picked up. To introduce twist between layers, the same flake is only partially picked up then rotated before the rest is picked up.

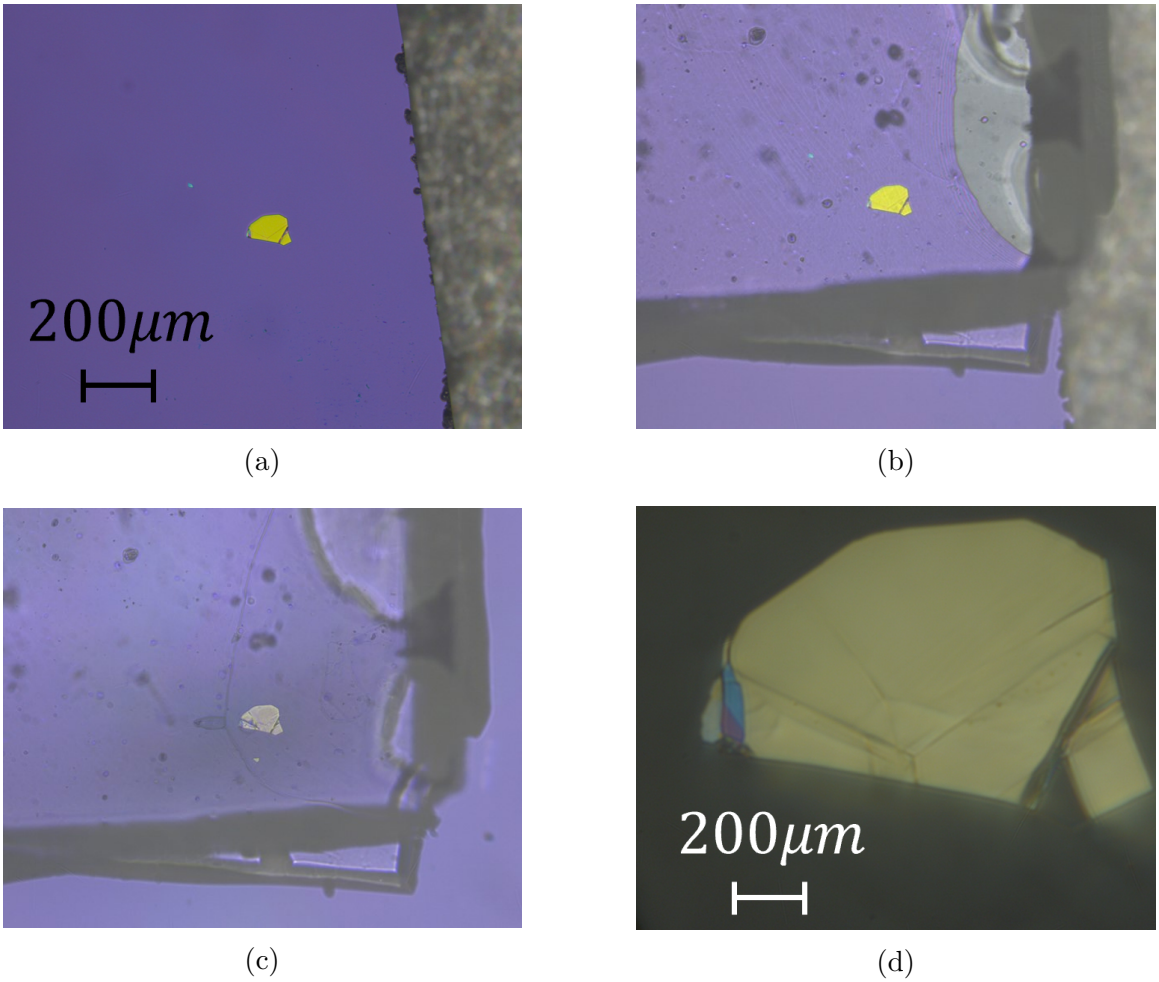


(a) (b)

(c) (d)

Figure A.4: Dry transfer technique used to pickup an hBN flake. a) hBN flake exfoliated onto $Si/SiO_2$ substrate b) PPC/PDMS stamp making contact with the substrate with contact area visible from interference fringes. c)d) hBN stuck to PPC and removed from substrate

## A.4 Specific Stamp Preparation for Graphite

Anecdotally, picking up graphite as the first material in a heterostructure can be quite an arduous task with PPC but once the graphite is on the PPC, subsequent flakes are relatively easy to pickup. Some labs use polycarbonate (PC), which is more effective

at picking up graphite, but it is not soluble in acetone and its $T_g$ is too high for our setup (180°C). One solution is to exfoliate graphite directly on PPC which has high yield. In this method, a graphite flake is thinned on tape normally and pressed onto a PDMS square before pressing the PDMS onto a PPC covered substrate. Flakes can then be identified on the PPC coated substrate with greatly reduced contrast. Identifying very thin flakes may be challenging, but thicker flakes do not pose an issue. Once a desirable flake is identified, a standard tape window can be used to lift the PPC off the substrate and onto a PDMS square or hemisphere on a glass slide. By hand it may be difficult to place the PPC film on the PDMS such that the identified flake lies above the PDMS. Instead, the film can be placed onto a glass slide with a hole drilled in it. The flake can then be lined up to the PDMS under the microscope with the previously described transfer stage. Once aligned, the PPC film can be lowered to the PDMS and the tape frame will release itself from the holed slide with a bit of heating. This graphite flake can then be dropped off onto a substrate or can be used to pick up other materials.

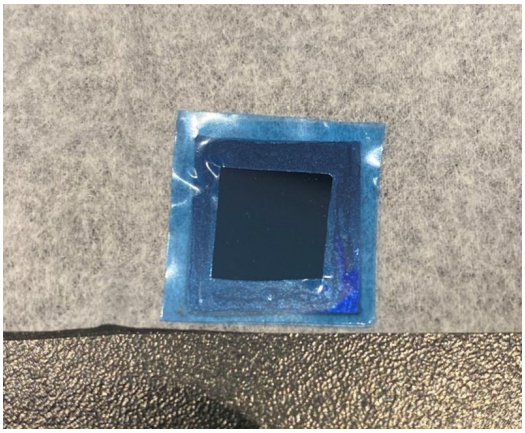

(a)



(b)

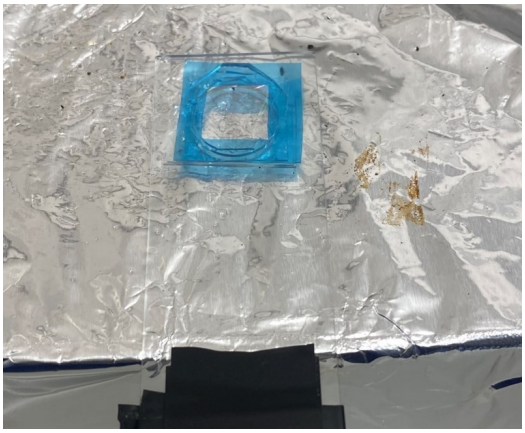

(c)

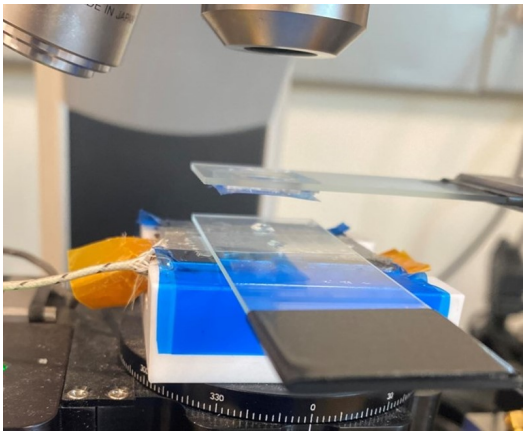

(d)

Figure A.5: Graphite stamp preparation. a) PPC film covered 285nm $SiO_2$/Si wafer with tape frame. b) After placing flakes onto the PPC film, the tape frame and PPC are removed from the substrate and placed onto a glass slide with a hole. Graphite side into the hole. c) The suspended PPC film on the holed glass slide is heated on a hotplate to remove ripples. d) Once a flake is identified it is aligned to a standard PDMS glass slide and the film is transferred.

## A.5 Flake Preparation on Substrate

Often, desirable flakes are surrounded by large flakes that might interfere with a transfer. In addition, the standard twisted sample fabrication method requires tearing a flake which can also introduce strain and angle inhomogeneity. It is possible to carefully remove adjacent flakes with a set tweezers by hand, but this is not a controlled method and has a high chance of damaging the flake of interest. Instead, one can use their transfer stages to carefully bring an AFM tip down to the surface of their substrate. Carefully dragging the tip across an area can remove debris and or make cuts in flakes [112].

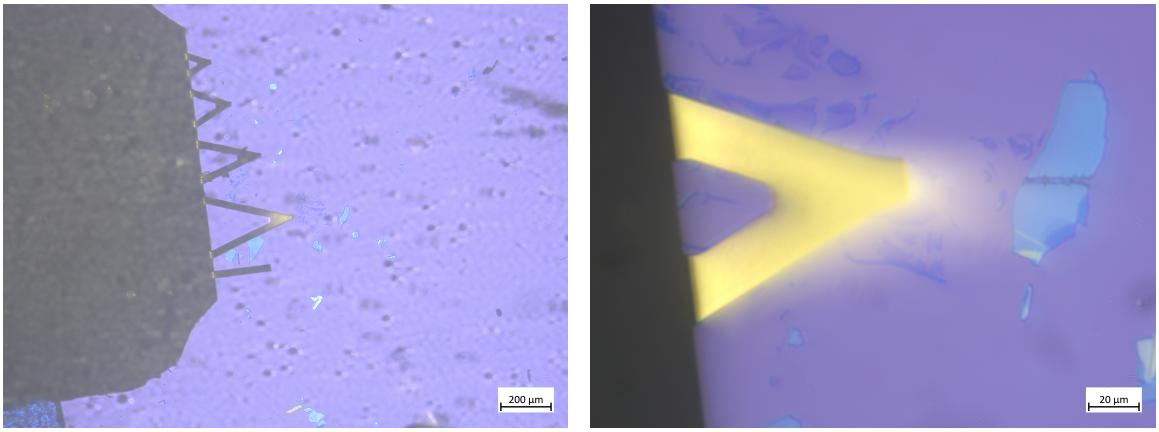


(a) (b)

Figure A.6: Optical images of AFM tip used to cut flake on substrate a) x5 magnification image of AFM tip in contact with substrate. b) x50 magnification image of AFM tip in contact with substrate after cutting through flake.

### A.6 Inverted Transfer

Once a stack of vdW materials has been constructed on a PPC stamp, the sample is transferred to a prepared substrate for further analysis. The inverted transfer method is commonly used because it ensures the top surface maintains limited contact with polymer contaminants, critical for STM samples. During this technique, the PPC tape window is removed from the glass slide and is placed on the substrate flake side up. The PPC film is then removed through tube and vacuum furnace annealing. As the PPC evaporates from underneath the flakes, the flakes have a tendency to drift away from their original location (Figure A.8). When the heterostructure needs to be placed near certain features, this technique can not be used reliably. An intermediate polymer can be used to remedy this problem and is described in Section 3.6.1.

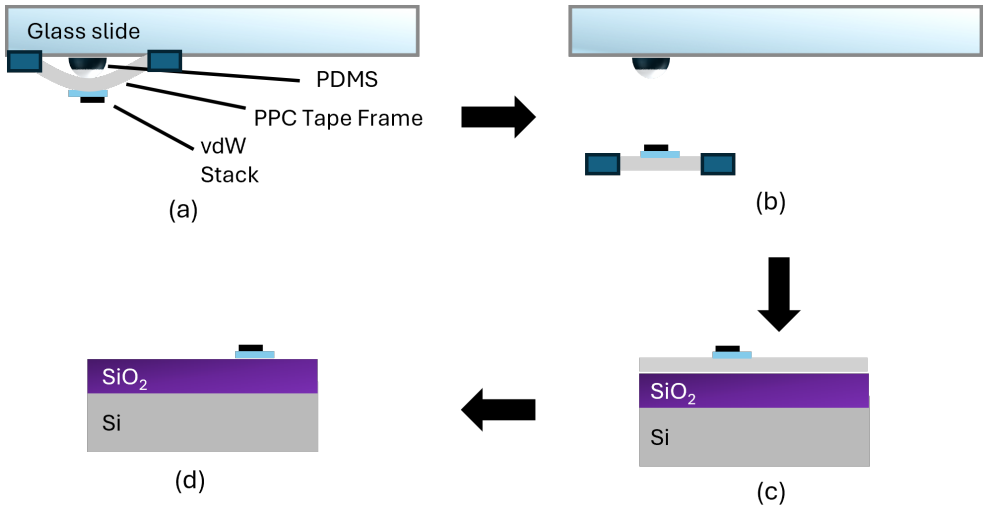


Figure A.7: Inverted transfer steps a) vdW stack on PPC film. b) PPC film removed and flipped flake side up. c) PPC placed on substrate. d) Substrate undergoes annealing to remove PPC. While the PPC is removed, the vdW stack has the potential to drift from its original location as is shown with the transparent copy to its left.

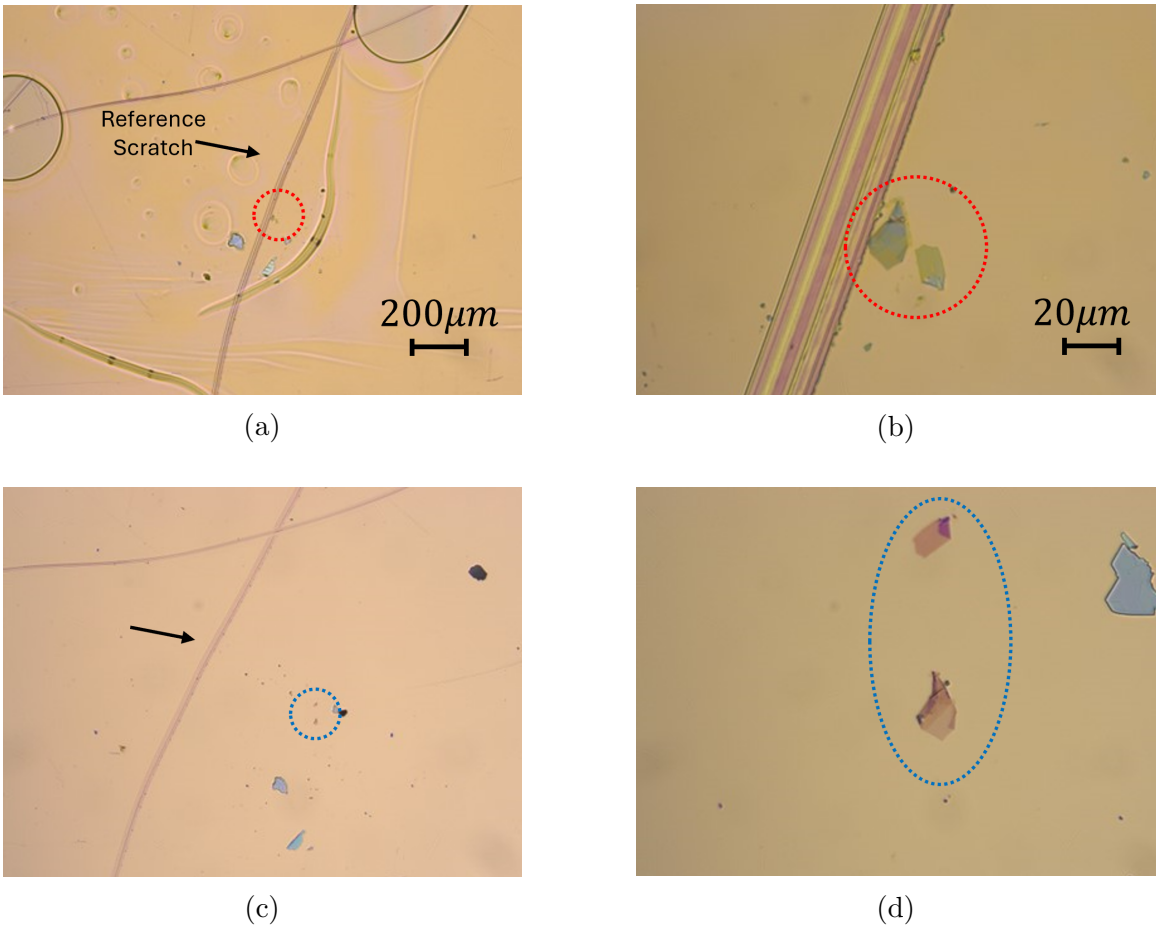


(a) (b)

(c) (d)

Figure A.8: Inverted transfer before and after PPC removal. a),b) vdW stack placed on substrate by inverted transfer viewed at x5 and x50 magnification respectively. c), d) vdW stack after tube furnace and vacuum annealing to remove PPC underneath viewed at x5 and x50 magnetification respectively. Comparing their location relative to the reference scratch it is clear they have drifted hundreds of microns.

## B Polymer Stamp PDMS Shape Motivation

When the contact area made between a PPC/PDMS stamp and a substrate is too large, the PPC can sometimes stick to the substrate making the transfer significantly more difficult.The hemispherical PDMS makes it easier to minimize the contact area.

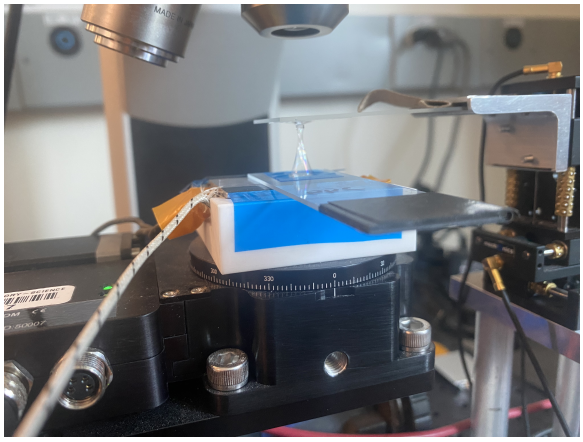

Figure A.9: Transferring a vdW structure from a PPC/PDMS stamp when the contact area is too large resulting in the PPC film being stretched and not detaching.

## C Graphene Band Structure

The following derivation is reproduced from my homework submission for PHY5110, Winter 2024. To calculate the electronic structure of graphene, I use a common approach of a nearest neighbour (NN) tight binding model. Graphene sublattices are identical and as such the onsite energy of each is identical. I am therefore free to set the energy of occupying a carbon atom to 0. The Hamiltonian is then only the kinetic energy from hopping between nearest neighbours which are on different sublattices. Hopping is captured through the creation of an electron on sublattice A (B) at site $R_A$ ($R_B$) and the annihilation of an electron on sublattice B (A) at site $R_B + \delta$ ($R_A + \delta$). The annihilation/creation operators are distinct between sublattices, $a^\dagger/a$ and $b^\dagger/b$. NN atoms are always on the other sublattice such that we can write the Hamiltonian

as,

$$H = -t_{NN} \sum_{R_B,\delta} b^\dagger_{R_B} a_{R_B+\delta} + c.c. \tag{1}$$

where there are three $\delta$ connecting NN from the other sublattice. I now rewrite the creation/annihilation operators in momentum space.

$$H = -\frac{t_{NN}}{N} \sum_{R_B,\delta} \sum_{k,k'} b^\dagger_k a_{k'} e^{-ikR_B} e^{ik'(R_B+\delta)} + c.c. \tag{2}$$

$$H = -\frac{t_{NN}}{N} \sum_{R_B,\delta} \sum_{k,k'} b^\dagger_k a_{k'} e^{iR_B(k'-k)} e^{ik'\delta} + c.c. \tag{3}$$

We use the definition of the Kronecker delta in terms of Fourier components,

$$H = -t_{NN} \sum_{\delta} \sum_{k,k'} b^\dagger_k a_{k'} e^{ik'\delta} \frac{1}{N} \sum_{R_B} e^{iR_A(k'-k)} + c.c. \tag{4}$$

$$H = -t_{NN} \sum_{\delta} \sum_{k,k'} b^\dagger_k a_{k'} e^{ik'\delta} \delta_{k,k'} + c.c. \tag{5}$$

$$H = -t_{NN} \sum_{k,\delta} b^\dagger_k a_{k'} e^{ik'\delta} + c.c. \tag{6}$$

The three NN vectors are: $\delta_1 = a(0,1)$, $\delta_2 = a(-\frac{\sqrt{3}}{2}, -\frac{1}{2})$, $\delta_2 = a(\frac{\sqrt{3}}{2}, -\frac{1}{2})$ where $a$ is

the carbon carbon separation length.

$$H = -t_{NN} \sum_k b_k^\dagger a_k (e^{-ik_y a} + e^{ik_x a \frac{\sqrt{3}}{2} + ik_y a \frac{1}{2}} + e^{-ik_x a \frac{\sqrt{3}}{2} + ik_y a \frac{1}{2}}) + c.c. \tag{7}$$

$$H = \sum_k b_k^\dagger a_k f(k) + c.c. \tag{8}$$

$$H = \sum_k b_k^\dagger a_k f(k) + \sum_k b_k a_k^\dagger f^*(k) \tag{9}$$

$$H = \sum_k b_k^\dagger a_k f(k) + b_k a_k^\dagger f^*(k) \tag{10}$$

$$H = \sum_k \psi^\dagger(k) h(k) \psi(k) \tag{11}$$

where $\psi(k) = (b_k, a_k)^T$ is a field operator for momenta k on both sublattices and

$$h(k) = \begin{bmatrix} 0 & f(k) \\ f^*(k) & 0 \end{bmatrix}. \tag{12}$$

This is a good form and all we need to do is solve for the eigenvalues of $h(k)$.The eigenvalues are $\pm|f(k)|$, where $f(k)$ can be simplified to

$$f(k) = -t(e^{-ik_y a} + e^{ik_x a \frac{\sqrt{3}}{2} + ik_y a \frac{1}{2}} + e^{-ik_x a \frac{\sqrt{3}}{2} + ik_y a \frac{1}{2}}) \tag{13}$$

$$f(k) = -t(e^{-ik_y a} + e^{ik_y a \frac{1}{2}}(e^{ik_x a \frac{\sqrt{3}}{2}} + e^{-ik_x a \frac{\sqrt{3}}{2}})) \tag{14}$$

$$f(k) = -t(e^{-ik_y a} + 2e^{ik_y a \frac{1}{2}} \cos(\frac{\sqrt{3}a}{2} kx)) \tag{15}$$

therefore

$$|f(k)|^2 = (-t(e^{-ik_y a} + 2e^{ik_y a\frac{1}{2}}\cos(\frac{\sqrt{3}a}{2}kx)))(-t(e^{ik_y a} + 2e^{-ik_y a\frac{1}{2}}\cos(\frac{\sqrt{3}a}{2}kx))) \tag{16}$$

$$|f(k)|^2 = t^2(1 + 2\cos(\frac{\sqrt{3}a}{2}k_x)(e^{i\frac{3a}{2}k_y} + e^{-i\frac{3a}{2}k_y}) + 4\cos^2(\frac{\sqrt{3}a}{2}kx)) \tag{17}$$

$$|f(k)|^2 = t^2(1 + 4\cos(\frac{\sqrt{3}a}{2}k_x)\cos(\frac{3a}{2}k_y) + 4\cos^2(\frac{\sqrt{3}a}{2}kx)) \tag{18}$$

$$E(k) = \pm|t|\sqrt{1 + 4\cos(\frac{\sqrt{3}a}{2}k_x)\cos(\frac{3a}{2}k_y) + 4\cos^2(\frac{\sqrt{3}a}{2}k_x)} \tag{19}$$

There are six points in the first BZ in which the energy goes to zero ,however only two of them are unique as the others are connected by reciprocal lattice vectors. The points are known as the $K$ and $K'$ points and are $K = \frac{2\pi}{3a}(\frac{2}{\sqrt{3}}, 0)$ and $K' = \frac{2\pi}{3a}(-\frac{2}{\sqrt{3}}, 0)$. Now, let's expand $f(k)$ around our K points and plug into our diagonalized Hamiltonian again!

$$f(K + \delta k) \approx f(K) + \nabla f(K) \cdot (K + \delta k) \tag{20}$$

$$\partial_{k_y} f = -t(-iae^{-ik_y a} + iae^{i\frac{a}{2}k_y}cos(\frac{\sqrt{3}a}{2}k_x) \tag{21}$$

$$\partial_{k_y} f(K) = -t(-ia + ia\cos(\frac{\sqrt{3}a}{2}\frac{4\pi}{3a\sqrt{3}})) = it\frac{3a}{2} \tag{22}$$

$$\partial_{k_x} f = t\sqrt{3}ae^{i\frac{1}{2}k_y a}\sin(\frac{\sqrt{3}a}{2}k_x) \tag{23}$$

$$\partial_{k_x} f(K) = t\sqrt{3}a\sin(\frac{\sqrt{3}a}{2}\frac{4\pi}{3a\sqrt{3}}) = t\frac{3a}{2} \tag{24}$$

$$f(K+\delta k) \approx t\frac{3a}{2}(\delta k_x + i\delta k_y) \tag{25}$$

$$f^*(K+\delta k) \approx t\frac{3a}{2}(\delta k_x - i\delta k_y) \tag{26}$$

$$|f(K+\delta k)|^2 = f(K+\delta k)f^*(K+\delta k) \tag{27}$$

$$E(K+\delta k) = \pm t\frac{3a}{2}|\delta k| \tag{28}$$

$$E(K+\delta k) = \pm v_f|\delta k| \tag{29}$$

We see that the dispersion relation of graphene near its K points is analogous to light where it is only linearly dependent on momenta.

Now, we want to calculate the density of states for graphene. I follow the standard counting procedure, where the total number of states with momenta equal to or less than $k$ are the volume in k-space over the spacing between states.

$$n_s = \frac{V_k}{\Delta k} = \frac{2\pi k^2}{(2\pi/L)^2} = \frac{k^2L^2}{2\pi} \tag{30}$$

$$n_s/A = \frac{k^2}{2\pi} \tag{31}$$

The number of states between $k$ and $k+\delta k$ is

$$dn_s = \frac{dn_s}{dk}dk \tag{32}$$

$$g(E)dE = \frac{dn_s}{dk}dk \tag{33}$$

$$g(E) = \frac{k}{\pi}(\frac{dE}{dk})^{-1}. \tag{34}$$

We now how the density of states in number of states per unit energy per unit area. For most systems there is a spin degeneracy between energies, so a factor of 2 is added, but here we also have a K valley degeneracy.

$$g(E) = 2(2)\frac{k}{\pi}(\frac{dE}{dk})^{-1} \tag{35}$$

$$g(E) = 2(2)\frac{k}{\pi}(v_f)^{-1} \tag{36}$$

$$g(E) = 2\frac{E}{\pi v_f^2}, \tag{37}$$

The DOS of a material can only be positive,

$$g(E) = 2\frac{|E|}{\pi v_f^2}. \tag{38}$$

## D Scanning Tunneling Microscope

The scanning tunneling microscope (STM) is an SPM technique which relies on a tunneling current between an atomically sharp tip, ideally one atom, and metallic sample which goes as $I_T \propto e^{-\kappa d}$. In constant current mode (i.e. constant interaction), xy piezoelectric actuators scan the tip across the surface while the PID controls a z piezoelectric actuator in the tip to change the height to maintain the current at some setpoint. This gives the user a topographic map of the surface of the material under investigation. The tunneling current is also dependent on the local density of states (LDOS, DOS) of the sample. If there are no available states at the correct energy to tunnel into, then no tunneling current will be recorded. By measuring the dI/dV one can measure the DOS as a function of energy where the DC voltage corresponds to

the energy of the electrons. This is fantastic as it begins to highlight the electronic bands of a material.

## E QTM: Momentum Resolved Twisted Bilayer Graphene Examples

I use the model described in Chapter 2 to simulate the tunneling current between graphene probe through a $WSe_2$ tunnel barrier into two different samples with band structures that approximate twisted bilayer graphene (TBLG). The TBLG band structures are modeled as two Dirac cones separated in k-space by the rotation of the sample with some coupling between them, as is done in [7]. I change the flatness of the bands to demonstrate that the resulting current plots are representative of the sample's bands. The input TBLG bands are shown in Figure A.10 and the calculated tunneling currents are shown in Figure A.11.

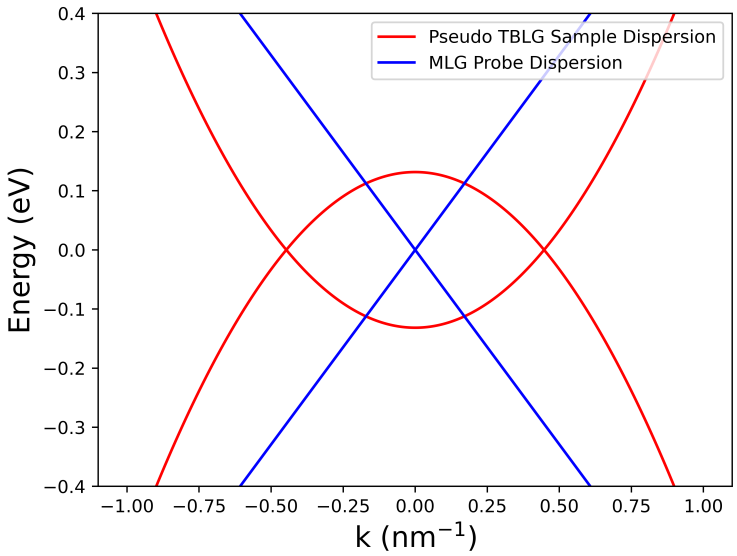


(a)

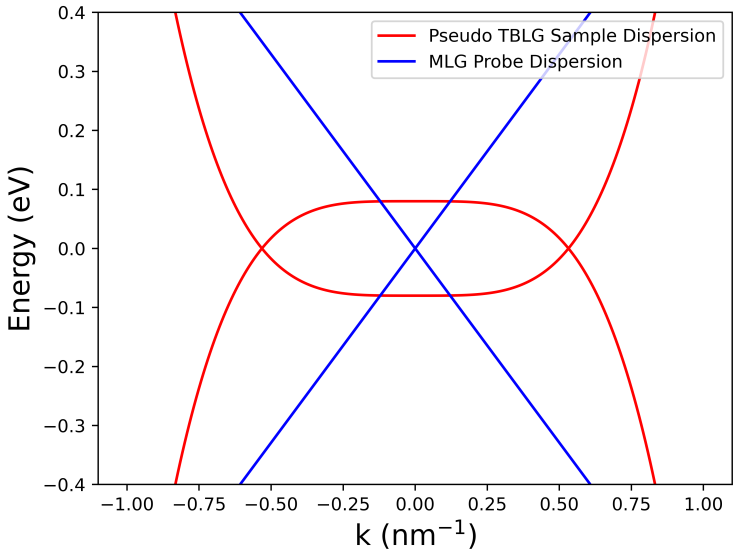


(b)

Figure A.10: Graphene probe and TBLG sample bands used in the calculation of tunneling current, shown in Figure A.11. The monolayer graphene band is shown in blue, and the TBLG bands are shown in red. The TBLG is approximated by two parabolic or quartic bands. The intersections of these bands near $\pm 0.5$ nm$^{-1}$ represent the two Dirac cones, separated by the twist angle between the individual graphene layers that make up the TBLG sample. The region in between approximates the hybridization of the bands. a) Parabolic approximation b) Quartic approximation

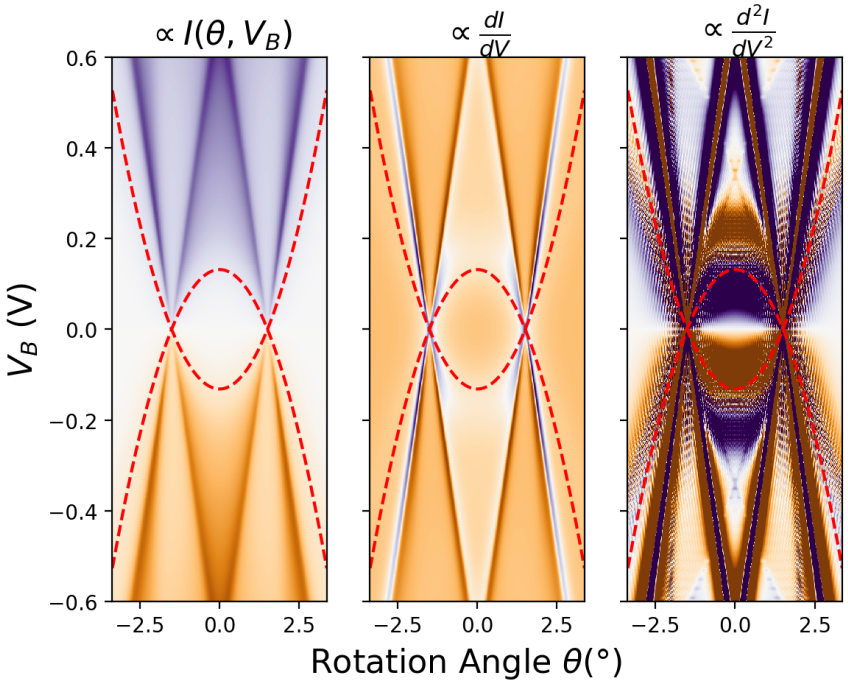


(a) a)

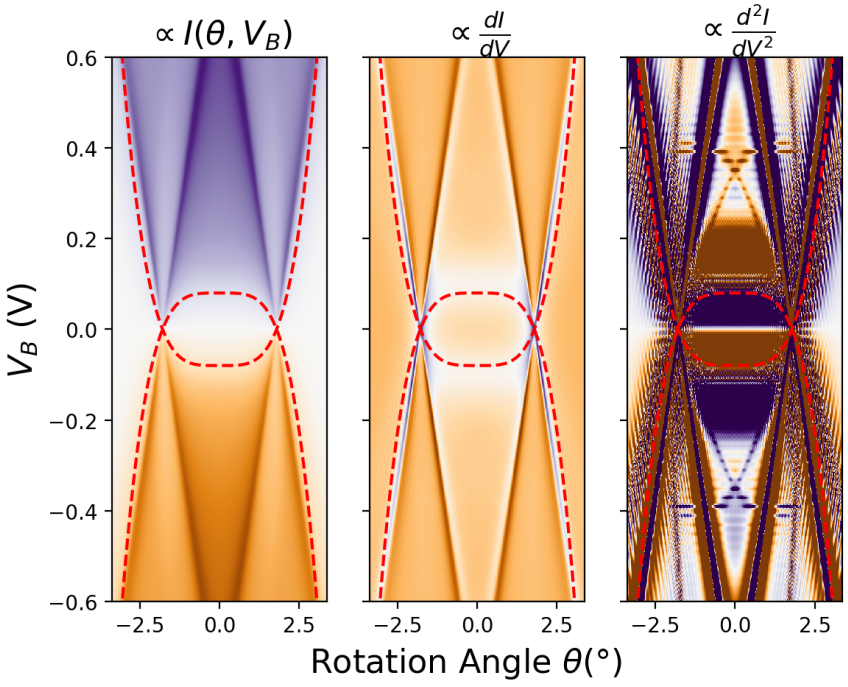


(b) b)

Figure A.11: Calculated tunneling current between graphene probe and TBLG samples with bands shown in Figure A.10. a) Parabolic approximation for TBLG bands b) Quartic approximation for TBLG bands

## F Photolithography Mask Design

Two photolithography masks were required for the pillar fabrication process. Both masks are made of sodalime glass and have patterned Cr to dictate which areas of resist get exposed. The first mask was designed to define the large pillar shapes in the photoresist. The Cr pattern on this mask is such that light exposes everywhere but the pillar shapes. The second mask is required to pattern electrical contacts on the pillars once they have been etched. The Cr pattern on this mask allows for light to only expose the contact patterns.

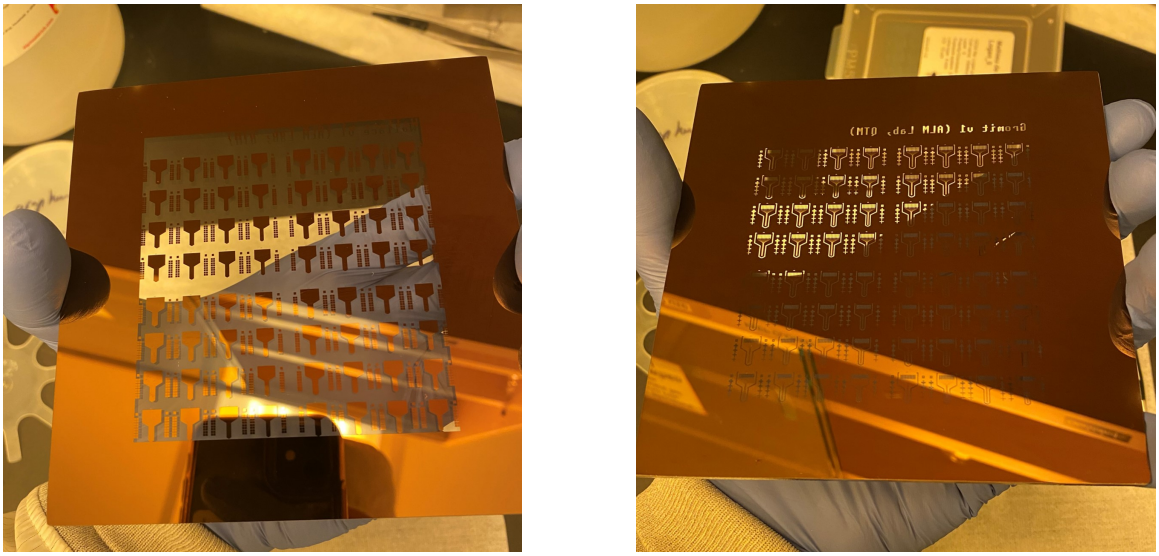

(a) (b)

Figure A.12: Photolithography masks a) First mask with Cr covering pillar shapes b) Second mask with Cr covering everywhere except for contact shapes

The masks were designed and ordered prior to the initial characterization of the required etching steps. They were designed in Python to automate the creation of features with varying shapes and sizes to accommodate a range of different process results. Primarily, 16 different pillar dimensions were included to allow for variations

in sidewall etching produced during the KOH etch. The variations were created by adding padding ranging from 200-450um to an unpadded "master" feature as shown in Figure A.13. The set of 16 is repeated four times on the mask as shown in Figure A.14.

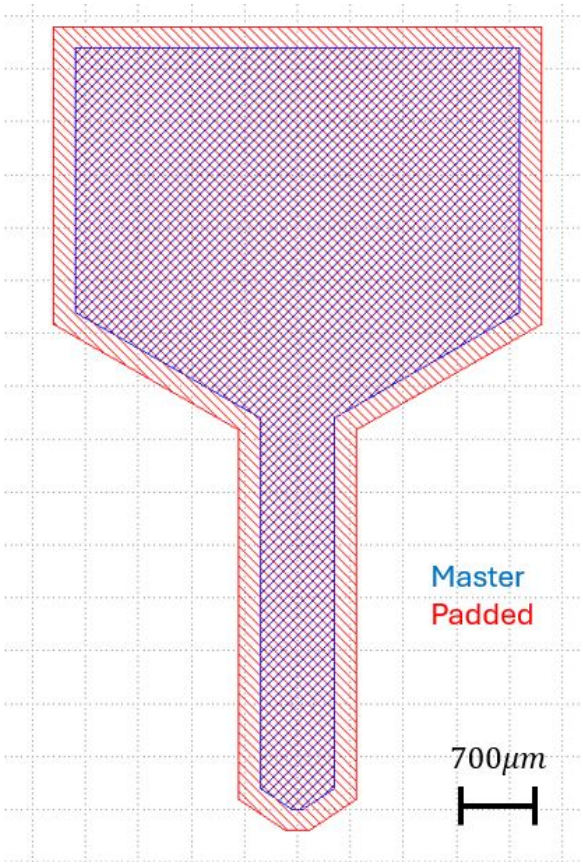


Figure A.13: Padding was added to pillar shapes. On the mask, only the padded features are found with padding ranging from 200 to 450 um.

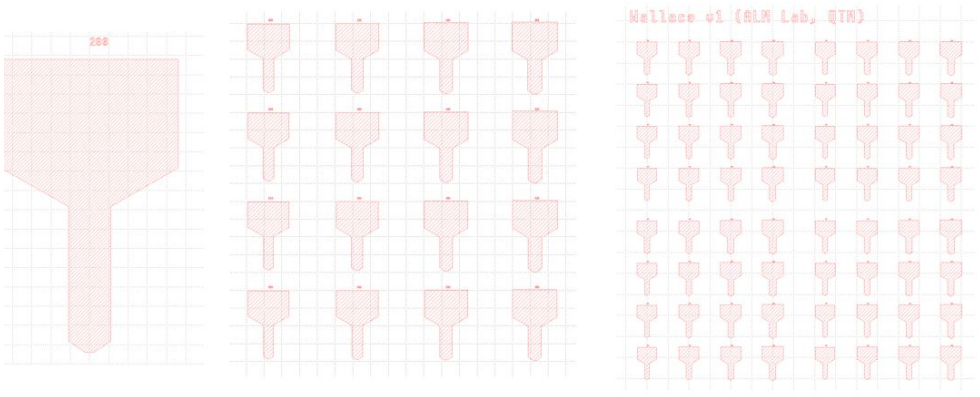


Figure A.14: Pillar shapes on the first photomask. Left: Smallest pillar feature with 200um of padding added to unpadded "master". Middle: 16 pillar features with padding ranging from 200-450um of padding. Right: All of the pillar features found in the first mask. 2x2 grid of the 16 pillar features shown in the Middle figure.

The second photolithography mask was then designed for the electrical contacts. The contacts are required to terminate near the edge of the pillar and must have large pads at the other end to wire bond to. Two different contact terminations were designed to allow for sample versatility as shown in the original paper and in Figure A.15. One termination is repeated in the top left and bottom right quadrants, and the other is repeated in the top right and bottom left quadrants.

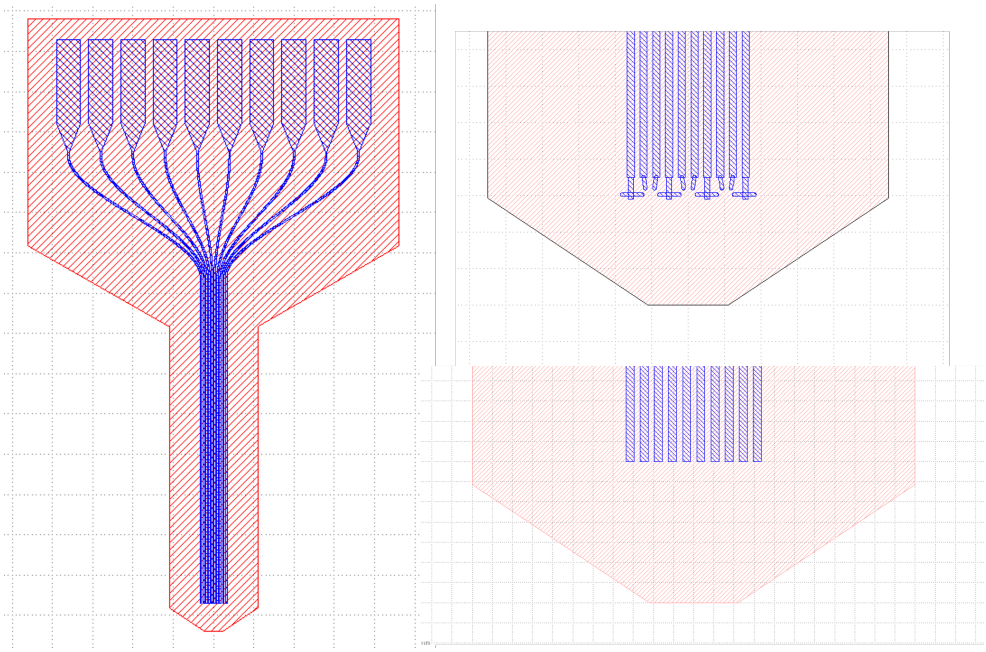

Figure A.15: Contact shapes overlaid onto a pillar shape. Left: Pillar shape shown in red. Contact pattern shown in blue. Top Right: Contact termination pattern variation. Bottom Right: Contact termination pattern variation.

While the first photolithography step does not require any alignment, the contacts need to be aligned to the pillars. Since the contacts are small, and only the contacts are exposed, there is limited visibility of the sample during alignment. Viewing windows and alignment marks are added to make aligning of the contacts to the pillars easier. The alignment marks are shown in Figure A.16 with their use demonstrated in Figure A.17. The viewing window added to the second mask that allows for alignment to the edge of the pillar features is shown in Figure A.18 with their use demonstrated in Figure A.19. A view of the two masks overlaid on each other, with all features, is shown in Figure A.20.

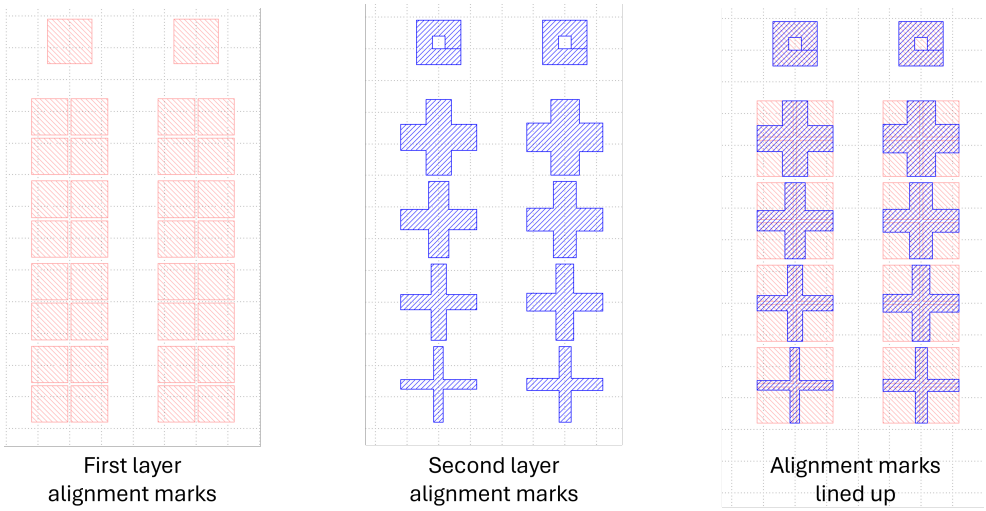


Figure A.16: Alignment marks in the first and second mask.

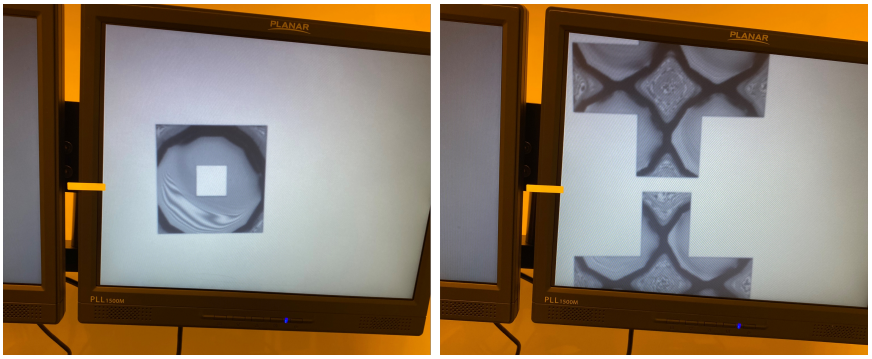

Figure A.17: Use of alignment marks when aligning second mask to etched pillar substrate.

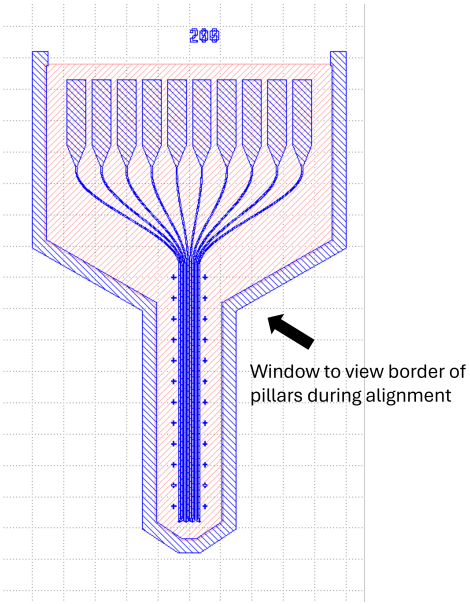


Figure A.18: Window in the second mask around the pillars to enable easy viewing.

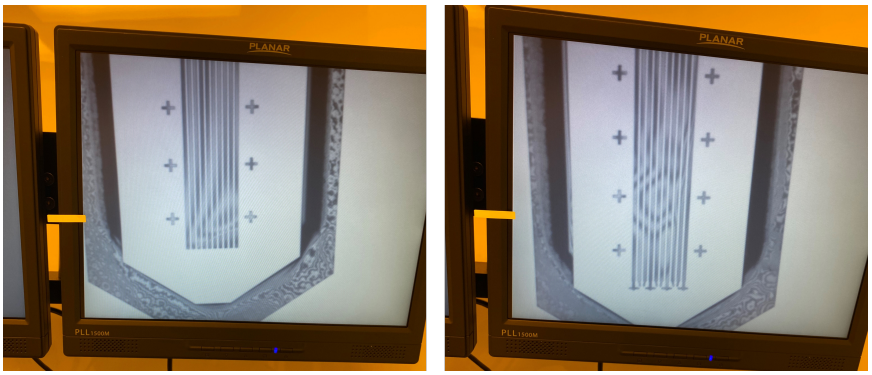


Figure A.19: Use of window demonstrated when aligning second mask to etched pillar substrate.

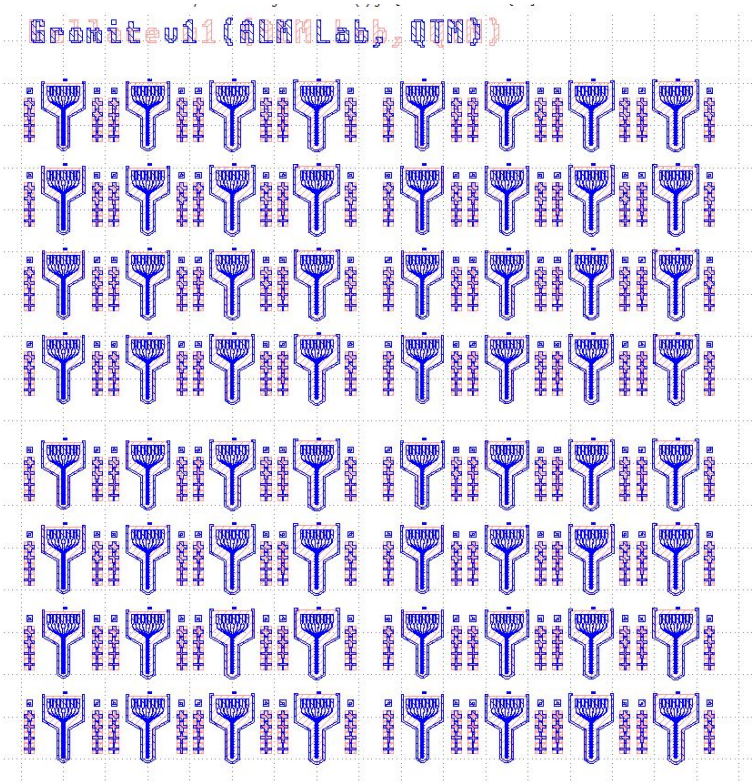

Figure A.20: First and second masks aligned.

# G Lockin Amplifier

## G.1 Filtering

Our device under test (DUT), the interface resistance, is linear, so we can treat each frequency component of the collected signal separately. To illustrate the filtering, we look at a signal at an arbitrary frequency, $\omega$

$$V = A\cos(\omega t + \vartheta) \tag{39}$$

If we mix it with two 90° out of phase signals at the reference frequency

$$A\cos(\omega t+\vartheta)\cos(\omega_r t)=\frac{A}{2}\{\cos((\omega+\omega_r)t+\vartheta)+\cos((\omega-\omega_r)t+\vartheta)\} \tag{40}$$

$$A\cos(\omega t+\vartheta)\sin(\omega_r t)=\frac{A}{2}\{\sin((\omega+\omega_r)t+\vartheta)+\sin((\omega-\omega_r)t+\vartheta)\} \tag{41}$$

it becomes clear that the average/DC value of either of these mixed signals is 0 unless $\omega=\omega_r$.

$$A\cos(\omega_r t+\vartheta)\cos(\omega_r t)=\frac{A}{2}\{\cos((2\omega_r)t+\vartheta)+\cos(\vartheta)\} \tag{42}$$

$$A\cos(\omega_r t+\vartheta)\sin(\omega_r t)=\frac{A}{2}\{\sin((2\omega_r)t+\vartheta)+\sin(\vartheta)\} \tag{43}$$

We can filter out the second harmonic by lowpass filtering the mixed signals such that only the reference frequency remains

$$\overline{A\cos(\omega_r t+\vartheta)\cos(\omega_r t)}=\frac{A}{2}\cos(\vartheta) \tag{44}$$

$$\overline{A\cos(\omega_r t+\vartheta)\sin(\omega_r t)}=\frac{A}{2}\sin(\vartheta) \tag{45}$$

## G.2 Testing

To test my lock-in amplifier before having a QTM to test on, I had to come up with a way to generate a signal with lots of noise. A simple and obvious way to do that is to take the voltage across a very small resistor in series with a large resistor forming a resistor divider, depicted in Figure A.21. The source amplitude was swept from 0.02

to 0.2V$_{pk-pk}$ at 10kHz With $R_{signal} = 100\Omega$ and $R_{series} = 1\text{M}\Omega$,

$$V_{signal} = V_{reference}\frac{100}{100 + 10^6} \tag{46}$$

$$V_{signal} \approx V_{reference}10^{-4} \tag{47}$$

The recorded IV curve and signal to source voltage ratio shown in Figure A.22 mostly match what was expected for source voltages when above 50mV. While not exact, the small signal amplitude certainly affects the ability of the lockin, but during proper measurements a transimpedence amplifier would amplify the signal into a higher voltage range. The collected signal shown in the bottom row of Figure A.23 clearly has noise present which has been successfully filtered out.

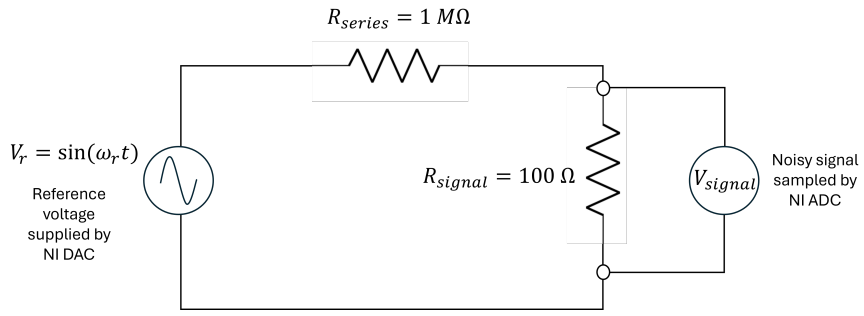


Figure A.21: Circuit used to test homemade lock-in amplifier

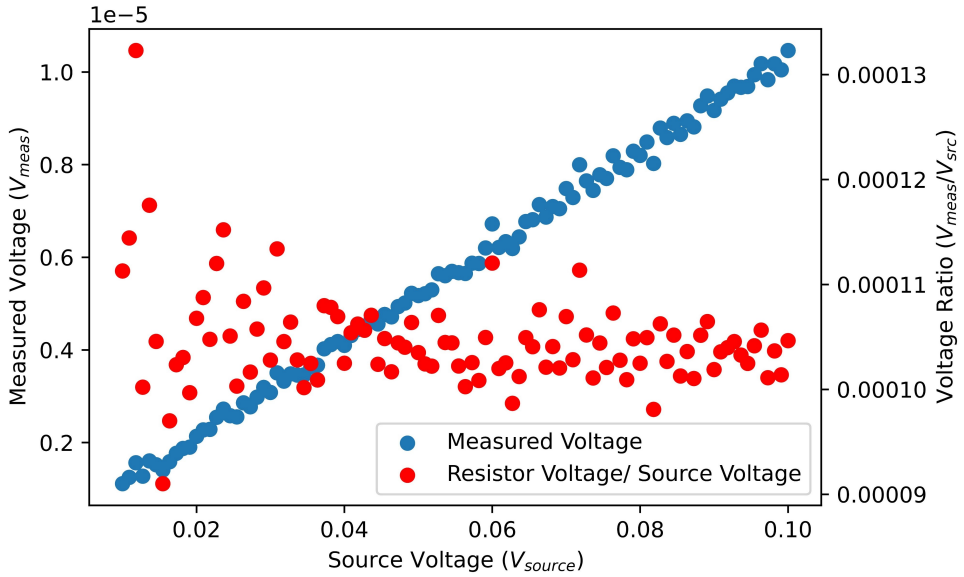


Figure A.22: Demonstration of lockin amplifier used on test circuit achieving desired ratio set by the resistor divider.

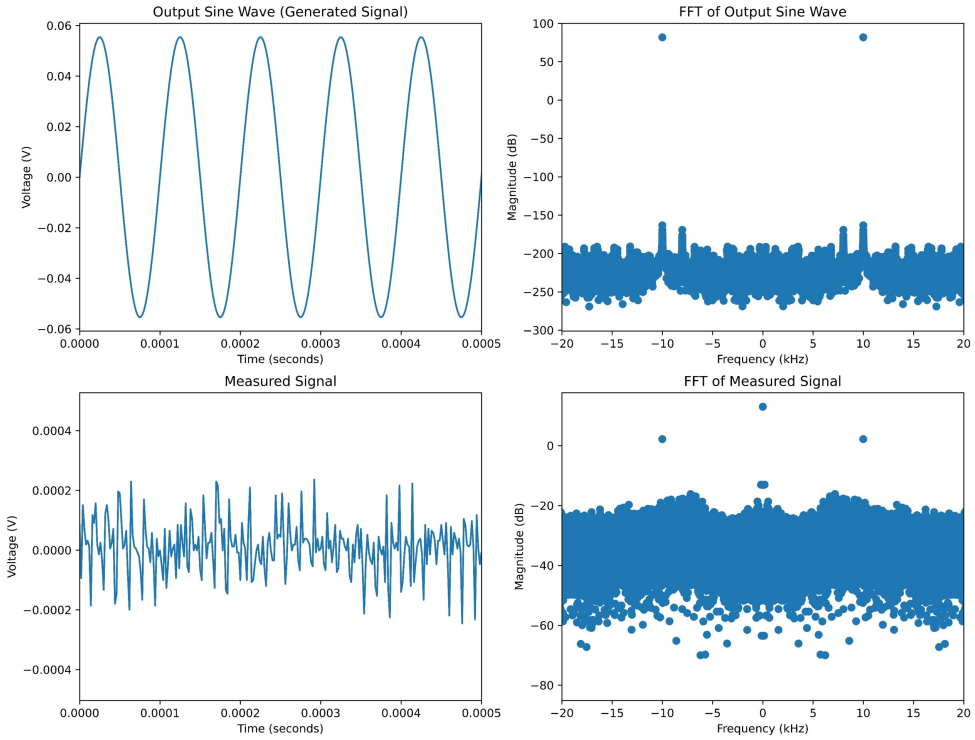


Figure A.23: Source and measured signal during lockin amplification test. Left: In time, Right: In frequency. Top: Source signal, Bottom: Measured signal.

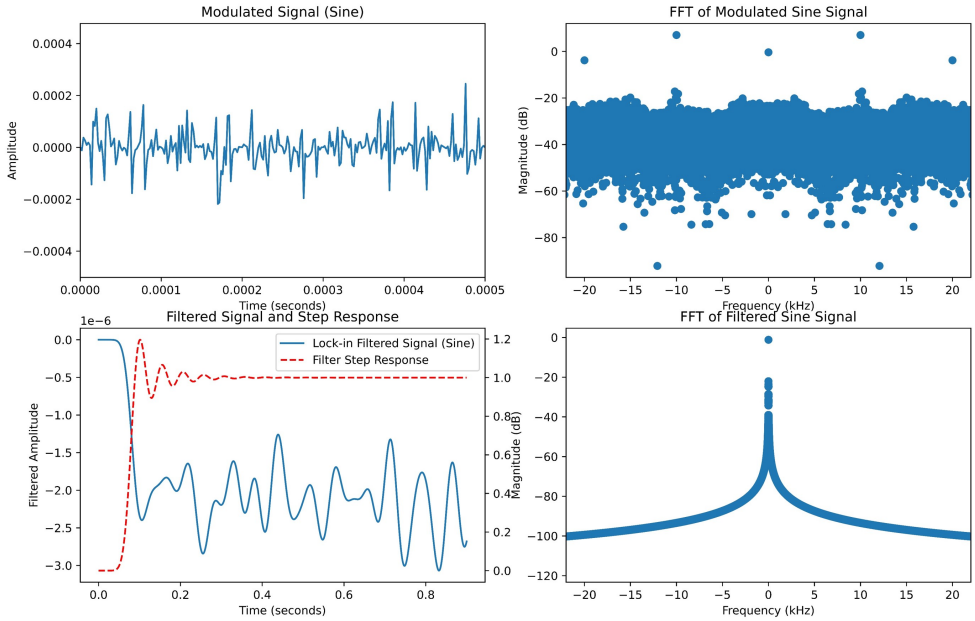


Figure A.24: Processing performed on measured signal during lockin amplification. Left: In time, Right: In frequency. Top: Modulated signal achieved by mixing the measured signal from Figure A.23 with the reference signal, Bottom: Low pass filter of the mixed signal extracting only the DC value when averaged, corresponding to the signal amplitude at the reference frequency. Step response of the used lowpass filter shown in red.

## H AFM Tip Solvent Bath

Once a flake or vdW heterostructure with its carrying polymer has been aligned and melted onto the cantilever the polymer must be washed away. Ideally, the tip would be loaded into the probe holders and placed into an acetone bath. In our case, all the AFM tools are from a shared facility and this was not possible. Instead, I opted to manually hold the cantilever body with tweezers during the acetone bath. This approach, while functional, was impractical for extended durations and resulted in accidental cantilever breakage. If these problems are relevant, I would recommend

this as a potential solution, albeit not very sophisticated.

The solution I opted for was to load the AFM cantilever into a set of reverse action tweezers. With a 3D printed collar, sized to fit around a standard beaker, and an angled slot for the tweezers the AFM tip can comfortably sit in an acetone bath. The tweezers are easily loaded and removed dramatically reducing the chance of knocking the tip into the sides of the beaker.

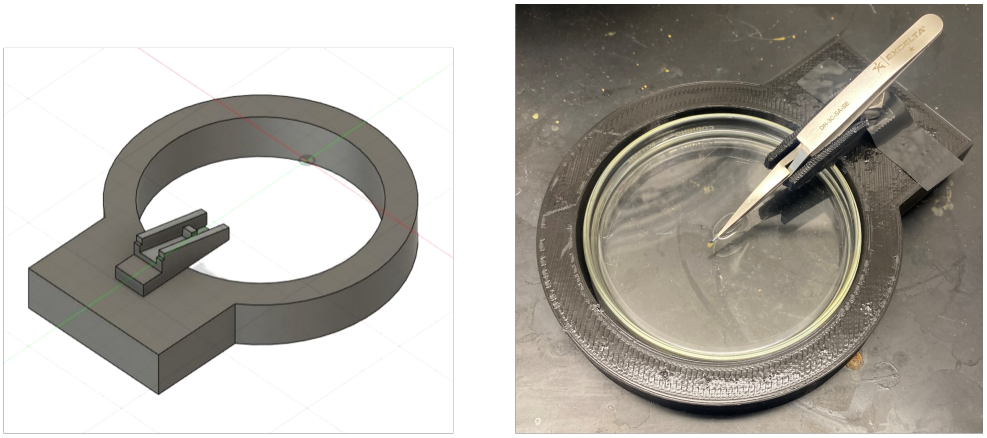

Figure A.25: Tweezer holder to facilitate AFM tip solvent baths. Left: Schematic of design to holder tweezers. Right: 3D printed tweezer holder.

# I Ellispometry

Ellipsometry was used to monitor thin film thicknesses where step edges were not available. The method relies on the difference in Fresnel reflectance coefficients between s ($\perp$ to the plane of incidence) and p ($\parallel$ to the plane of incidence) polarizations,

$$R_s = |\frac{n_1 \cos\theta_i - n_2 \cos\theta_t}{n_1 \cos\theta_i + n_2 \cos\theta_t}|^2 \tag{48}$$

$$R_p = |\frac{n_1 \cos\theta_t - n_2 \cos\theta_i}{n_1 \cos\theta_t + n_2 \cos\theta_i}|^2 \tag{49}$$

where $n_i$ are the indices of refraction and $\theta_{i,t}$ are the incident and transmitted angles which can be related by Snell's law. Ellipsometry measures the change in the polarization state of light reflected from a a thin film sample. Incident light, often linearly polarized, with a known polarization undergoes a phase shift and change in amplitude upon reflection, depending on the index and thickness of the film. The reflected light is generally elliptically polarized and this is recorded by the ellipsometer. If the thickness of the film is known, the index can be extracted, or as was done here, the index can be input and the thickness can be measured. The ellipsometer I used has Xe lamp with a motorized monochrometer to sweep the input wavelength. My recipe swept from 400-700nm in increments of 10nm with 100ms integration times. The index of $SiO_2$ is readily found online and the indices for photoresists are usually provided in their datasheets. Although some ellipsometers have built in spatial resolution, ours does not which motivates the use of witness samples with no patterning.

## J PMMA Transfer Examples

Here, I present examples of transferring a flipped vdW stack from a PMMA film, as described in Section 3.6.2, to a raised sample pillar, in Figure A.26, and tipless cantilever, in Figure A.27. Given the limited number of custom AFM tips available, a test was performed only on a tipless cantilever.

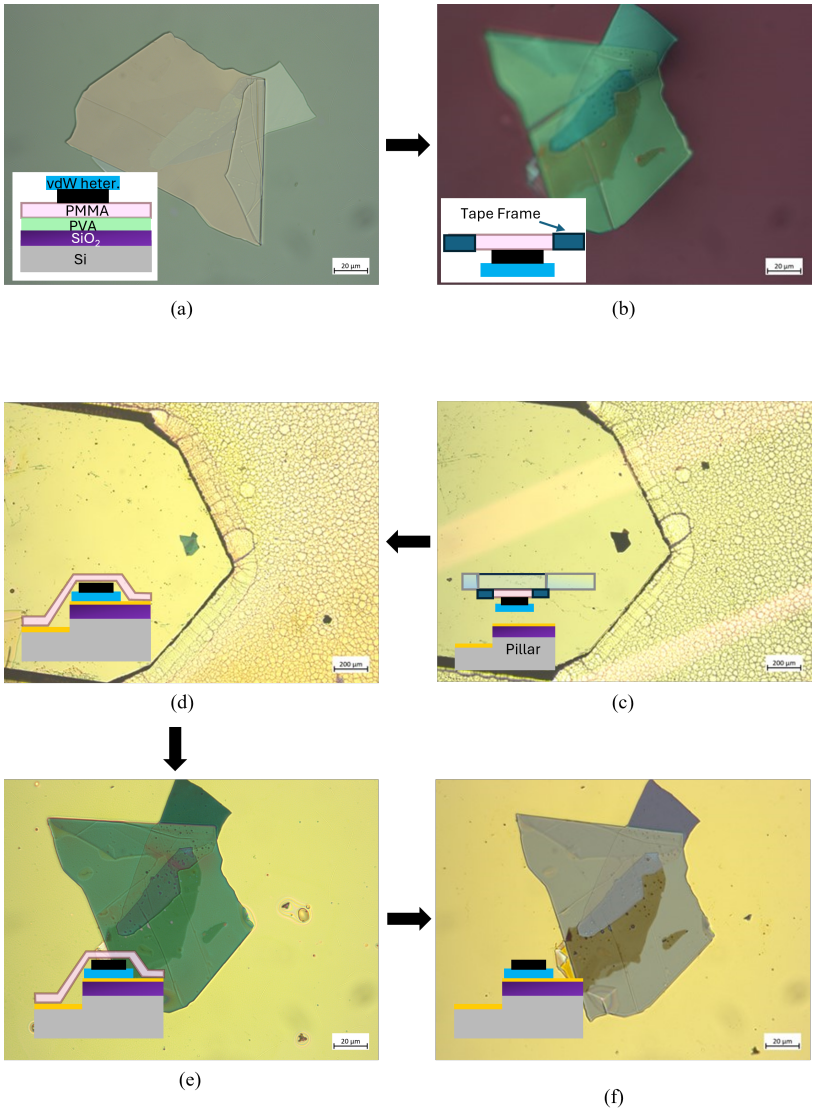


Figure A.26: Flipped vdW heterostructure transfer from PMMA film. a) Starting with a flipped vdW heterostructure on a PMMA/PVA film. The PMMA film is prepared using the technique described in Section 3.6.1. b) The PMMA film is lifted off the substrate and placed onto a holed glass slide. c) The flake is aligned to the pillar substrate. d) The PMMA film is melted onto the pillar. e) Zoomed in image of the vdW heterostructure on the pillar with the PMMA film overtop. f) The PMMA is removed with acetone such that ultimately the heterostructure is transferred right side up without drifting, as described in Section 3.6.2.

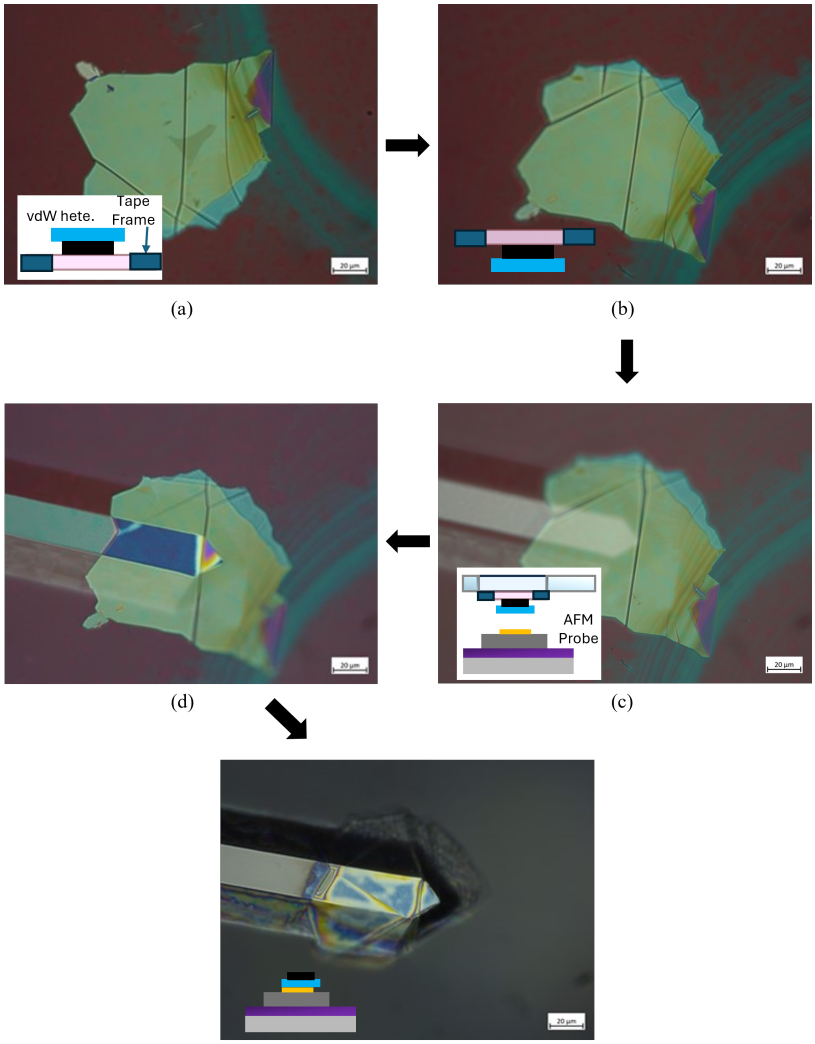


Figure A.27: Flipped vdW heterostructure transfer from PMMA film. a) Starting with a flipped vdW heterostructure on a PMMA film as prepared in Figure 3.32. b) PMMA film flipped rightside up as it will be placed onto the cantilever. Note the graphite is no longer visible. c) The vdW heterostructure film is then loaded onto a holed glass slide and aligned to the cantilever. d) The flake makes contact to the cantilever and the PMMA is melted off of the glass sldie. e) The PMMA is removed with acetone such that ultimately the heterostructure is transferred right side up without drifting, as described in Section 3.6.2.